Rostam Golesorkhtabar

Ab initio Calculation of Elastic Properties

General Implementation and Specific Application to the Shape-Memory Material NiTi

Dissertation

written at the Montanuniversität Leoben,
Chair of Atomistic Modelling and Design of Materials

under supervision of
Univ. Prof. Dr. Dr. h.c. C. Ambrosch–Draxl

Leoben, April 2013

Affidavit

I declare in lieu of oath, that I wrote this thesis and performed the associated research myself, using only literature cited in this volume.

April, 2013 Rostam Golesorkhtabar

To Nakisa

Zusammenfassung

Die elastischen Eigenschaften eines Materials spielen eine Schlüsselrolle in Forschung und Technologie, da sind grundlegend für das mechanische und thermodynamische Verhalten sind. Obwohl die mechanischen Eigenschaften stark von der Mikrostruktur abhängen, werden sie von Wechselwirkungen auf atomarer Ebene bestimmt. Aus diesem Grund bietet die computerunterstützte Festkörpertheorie auf Basis der Quantenmechanik einen Einblick, der wesentlich für das Verständnis des makroskopischen Materialverhaltens ist. Das Hauptziel dieser Arbeit ist die Entwicklung und Implementierung eines Schemas für die zuverlässige Ab-initio-Berechnung der elastischen Eigenschaften kristalliner Materialien.

Elastische Eigenschaften werden entweder durch die elastischen Konstanten, das heißt, durch die Komponenten des elastischen Tensors, charakterisiert, oder durch elastische Moduln, welche die entsprechenden gemittelten Größen darstellen. Die elastischen Konstanten können durch eine Taylor-Entwicklung der freien Energie oder der Spannung als Funktion der Kristallverformung (Verzerrung) definiert werden. Die Koeffizienten der Taylorreihe stellen dabei die elastischen Kostanten verschiedener Ordnung dar.

Um die elastischen Konstanten zu berechnen, benötigt man die Gesamtenergie oder die Spannung eines verformten Kristalls als Funktion der Verzerrung. Einen geeigneten quantenmechanischen Rahmen zur Bestimmung dieser Größen stellt die Dichtefunktionaltheorie (DFT) dar, die auch in der vorliegenden Arbeit eingesetzt wurde. Wir verwenden state-of-the-art DFT-Programme für die Berechnung der Energien und/oder der Spannung. Wir untersuchen elastische Konstanten zweiter Ordnung für ausgewählte, typische Materialien aller Gitterarten und elastische Konstanten dritter Ordnung jeweils für einen Prototypen eines kubischen, hexagonalen, und rhomboedrischen Systems. Die Implemetierung ist also allgemein in dem Sinne, dass für die elastischen Konstanten zweiter Ordnung alle Symmetrien berücksichtigt werden. Daneben legen wir besonderes Augenmerk auf die Auswertung der numerischen Daten zu Energie und Spannung. Wir schlagen eine neue Vorgangsweise vor, die die Bestimmung elastischer Konstanten auf der Basis von Ab-initio-Rechnungen so zuverlässig wie möglich macht.

Eine konkrete Anwendung von `ElaStic` im Rahmen dieser Disertation stellen Nickel-Titan-Legierungen dar, die zu einer Materialklasse zählen, welche bekannt für ihre Form-Gedächtnis-Eigenschaften ist. Da die entsprechenden Phasenumwandlungen zwischen den beteiligten kristallographischen Phasen durch Gitterverzerrungen vor sich gehen, spielen die elastischen Eigenschaften natürlicherweise eine zentrale Rolle. Wir haben die elastischen Konstanten und makroskopischen Moduln für die Kristallstrukturen B2, B19, B19′ and B33 berechnet. Wir zeigen, dass die B19 Struktur im Gegensatz zur B2-Struktur instabil ist und deshalb keine Zwischenphase für die Form-Gedächtnis-Legierung NiTi sein kann.

Summary

Elastic properties play a key role in science and technology as they characterize the mechanical and thermodynamical behavior of a material. Although mechanical properties may even strongly depend on the material's microstructure, they are determined by interactions happening on the atomistic scale. Thus, computational solid-state theory based on quantum-mechanics can provide insight which is crucial for the understanding of the materials's macroscopic behavior. The main goal of this thesis was the development and implementation of a scheme to reliably compute elastic properties of crystalline materials from first principles.

Elastic properties are either characterized by elastic constants, which are the components of the elastic tensor, or by elastic moduli, which are the corresponding averaged quantities. Elastic constants can be defined by a Taylor expansion of the free energy or stress in terms of the crystal deformation, *i.e.*, the strain. The coefficients of the Taylor series provide the elastic constants of different order.

To calculate elastic constants, one has to compute the total energy or stress of the deformed crystal. A well suited quantum-mechanical framework for doing so is density-functional theory (DFT) which was employed in the present work. We use state-of-the-art DFT codes for energy and stress calculations. We present second-order elastic constants choosing prototype materials for all crystal lattice types, and third-order elastic-constants for prototypes of cubic, hexagonal, and rhombohedral crystals, respectively.

Besides this general implementation in terms of symmetry, we place emphasis on the evaluation of numerical energy and stress data. We propose a new recipe to obtain elastic constants out of *ab initio* calculations in the most reliable manner. All the work has been collected in the software package called **ElaStic**. **ElaStic** is utilizing either the full-potential all-electron codes **exciting** and WIEN2k or the pseudo-potential plane-wave code Quantum ESPRESSO. It provides the elastic compliances tensor and applies the Voigt and Reuss averaging procedure in order to obtain bulk, shear, and Young moduli as well as the Poisson ratio for polycrystalline samples.

A specific application of **ElaStic** within this thesis, is given by nickel-titanium compounds, a material class which is well-known for shape-memory behavior. As the corresponding phase transformations between the involved crystallographic phases occur through lattice distortion, it is natural that elastic properties thereby play a central role. We have calculated the elastic constants and macroscopic elastic moduli for the B2, B19, B19′, and B33 crystal structure. We show that, in contrast to the B2 structure, the B19 phase is instable and, thus, can not be an intermediate phase for the NiTi shape-memory alloy. Analyzing our results, we argue that a direct transformation from the B2 to the B19′ phase is more probable than going through the B19 phase.

Contents

1 Introduction

Elastic properties play an important role in science and technology as they characterize the mechanical and thermodynamical behavior of materials. They are described by elastic constants of different order and elastic moduli. Elastic constants determine the response of a material to external stresses while elastic moduli, *e.g.* bulk modulus and shear modulus, determine the strength of materials to specific deformation.

Mathematically, elastic properties of condensed matter are described within *elasticity theory* which is a major area of continuum mechanics. It describes materials that return to their rest shape when applied stresses are removed. In this theory, second-order elastic constants are defined by Hooke's law which is valid upon linear-elastic deformation of materials. Higher-order elastic constants can be obtained by generalizing Hooke's law to cover the nonlinear-elastic deformation range of materials. Elastic moduli are expressed by averaging over the second-order elastic constants.

Experimentally, there are several methods to measure elastic properties, like ultrasonic wave transmission, Brillouin scattering, neutron scattering, and X-ray thermal diffuse scattering methods. Ultrasonic wave transmission and Brillouin scattering are the most widely used methods and the most complete sets of elastic constants are measured by ultrasonic wave transmission. However, for many materials, experimental values of elastic constants are not yet available.

Computational physics, which is a relatively new field, opened a new perspective for the investigation of the elastic properties. Mechanical properties are strongly dependent on the materials microstructure. In perfect crystals, they can be studied by interactions happening on the atomistic scale. Computational solid-state theory based on *quantum-mechanics* can provide insight which is crucial for the understanding of the material's macroscopic behavior.

In this thesis, we combine quantum mechanics with computational techniques to investigate elastic constants of crystalline solids. We introduce `ElaStic` as a tool for the *ab initio* calculation of SOECs and TOECs using two approaches

based on the numerical differentiation of (i) the total energy and (ii) the physical stress of a crystal as a function of the imposed strain. The current implementation of **ElaStic** is interfaced with the computer packages **exciting**, WIEN2k, and Quantum ESPRESSO, all of them based on density-functional theory [1, 2]. Furthermore, we introduce a fitting procedure to reduce the numerical errors appearing in the calculation of derivatives of the energy (or stress) with respect to the imposed strain of a crystal. In order to show the potential and accuracy of **ElaStic**, we have applied this tool to a set of prototype materials covering all crystal families and different types of atomic bonds.

In addition, we show an application of our work on NiTi as an example of *shape-memory* materials. Shape-memory alloys are a class of materials with the ability to recover their shape when the temperature is changed. In spite of their various applications from airplanes to small coffee-maker machines in our kitchens, these materials are not fully understood on the microscopic level. The shape recovery in shape-memory alloys happens by going through a *martensitic* transformation. This transformation takes place without long-range atomic diffusion but rather by some form of cooperative, homogeneous movement of many atoms resulting in a change in crystal structure. Since the martensitic transformation occurs upon crystal distortion, it is natural that elastic properties play a central role during the transformation. Therefore, in order to understand the behavior of shape-memory materials, it is important to obtain their elastic properties. In this thesis, we examine the elastic properties of different NiTi ordered crystal phases by investigations their elastic constants and bulk moduli.

A large amount of effort in the computational investigation of elastic properties is focused on the calculation of second-order elastic constants (SOECs) and third-order elastic constants (TOECs), because many physical properties like the mechanical and thermodynamical properties are related to them. The knowledge of these elastic constants is a cornerstone to determine characteristic physical properties of materials, such as inter-atomic potentials, equations of state, phonon spectra, mechanical stability, and phase transitions. Thermodynamically, they are related to specific heat, thermal expansion, Debye temperature, melting point, and Grüneisen parameters.

SOECs obey certain relations in a stable or metastable phase. It has been shown computationally that fcc MoN [3], bcc Al [4] and bcc Ir [4, 5], do not exist in nature because they are elastically unstable. Knowledge of SOECs may be implied to predict the existence and properties of new materials and phases. For instance, a new metastable phase of Si with five-fold coordination has been predicted [6].

TOECs and higher-order elastic constants play an important role in explaining anharmonic properties of solids. In the following, some examples are mentioned. The thermal expansion of a solid occurs due to the anharmonicity

of interatomic forces, therefore, the investigation of thermal expansion coefficients requires TOECs [7, 8, 9, 10]. They are useful for studying the generalized Grüneisen parameters [11] which describe the strain dependence of vibrational frequencies. In order to investigate materials under high stress, *e.g.*, solid dislocation which usually happens in the non-elastic deformation regime, a non-linear description of elastic properties and TOECs is important. To study changes in lattice parameter and bulk modulus at high-pressure situations, TOECs are needed [12]. In order to investigate the effect of temperature [13, 14, 15, 16] and pressure [17] on the SOECs, higher-order elastic constants must be taken into account. Third- and higher-order elastic constants are required also in Landau's elastic-phase transition theory [18] which explains first-order phase transitions of strained materials. There is a correlation between higher-order elastic constants and the melting temperature of a solid [19, 20].

Ab initio investigations of elastic constants is an established method to understand the mechanical properties of many materials. This is evidenced by the presence of a large number of papers on the *ab initio* calculation of SOECs and TOECs, *e.g.*, [21, 22, 23, 24, 25, 26, 27], in the literature. In these papers, elastic properties are usually investigated only for selected materials with a given crystal structure. A systematic analysis of SOECs for different lattice types has been presented in Refs. [28, 29] but the authors focused on ceramic materials only. Recently, general methodological approaches for calculating SOECs have been implemented in Refs. [30, 31] as tools using the computer packages CRYSTAL and VASP, respectively. These codes are utilized for the calculation of energy and stresses of distorted crystal lattices, respectively. To the best of our knowledge, there is no comprehensive computational study for TOECs which cover different crystal lattice types. In this work, we aim at covering these issues investigating the elastic constants in different orders, crystal symmetries, and type of materials by means of density-functional calculations.

The chapters and sections of this thesis are organized as follows: In Chapter 2, we introduce elasticity theory and elastic constants in general. We define stress and strain tensors in Sections 2.1 and 2.2, respectively. Then, in Section 2.3, we introduce Hooke's law as a classical stress-strain relation in the linearity limit and then, consequently, the compliance and stiffness SOECs are defined. In Section 2.4, we generalize Hooke's law in order to cover the non-linearity behavior of the stress-strain curve, by introducing higher-order elastic constants. In the same section, we see the influence of crystal symmetry on the SOEC matrix taking the tetragonal crystal as an example. In Section A.1, we show the SOEC and TOEC matrices/tensors for different types of crystals. At the end, in Section 2.5, we discuss how polycrystalline elastic constants are calculated out of single-crystal elastic constants.

For the elastic-constant calculations, energies or the stress tensors of distorted structures are required. We utilize *ab initio* codes for their calculation.

Thus, we dedicate Chapter 3 to the *ab initio* methodology. We start with the many-body crystal Hamiltonian in Section 3.1. Density-functional theory is introduced in Section 3.2. In Section 3.3, we review different methods for solving the Kohn-Sham equations of density-functional theory.

Chapter 4 is assigned to our implementation of elastic-constant calculations in the `ElaStic` code. In Section 4.1, we explain the flowchart of the `ElaStic` code, step by step. Then, in Section 4.2, we examine the accuracy of elastic-constants calculations. We focus on the numerical accuracy of derivatives, discussing a simple model as well as the DFT results. Moreover, we establish a computational method for the calculation of second- and third-order derivatives which ensure reliable results. In Sections 4.3 and 4.4, deformations for different crystals and computational details are introduced. At the end of this chapter, in Section 4.5, we present the elastic constants of representative materials for different classes of crystals.

In Chapter 5, we show an application of `ElaStic` for specific materials, which are different ordered structures of the shape-memory materials NiTi. In Section 5.1, we briefly describe phase transitions in shape-memory materials, and introduce different crystal phases in Section 5.2. At the end, in Section 5.3, we present results for elastic constants.

2 Elasticity

This chapter is dedicated to elasticity theory, as it is implemented in the **ElaStic** code for elastic-constant calculations. We describe how stress and strain can be specified in a solid, define the second-order elastic constants (SOECs) by introducing Hooke's law, deal with third- and higher-order elastic constants by generalizing Hooke's law, and at the end, we analyze the influence of crystal symmetry on the elastic properties. We introduce these topics by following the books "Physical Properties of Crystals" by J. F. Nye [32], "Thermodynamics of Crystals" by D. C. Wallace [33], "Computational Quantum Mechanics for Materials Engineers" by L. Vitos [34], and "Plasticity Theory" by J. Lubliner [35] and apply their notation.

2.1 Stress

Consider a body which is acted on by *external* forces. These external forces generate *internal* forces inside the body, such that each part of the body exerts a force on neighboring parts. In this situation, the body is in a state of *stress*. Stress is a physical quantity related to the internal forces acting between neighboring body particles. A stress is *homogeneous* if the forces acting on the surface, together with their orientations, are independent of the position of the particles in the body. In the following discussion, only homogeneous stresses will be considered.

Consider a unit cube, as shown in Figure 2.1, whose edges are parallel to the axes Ox_1, Ox_2, and Ox_3. The different force components, that in this case correspond to stress components too, are shown in Figure 2.1. Here, σ_{ij} is the force component in direction $+x_i$ which is transmitted from the face that is perpendicular to $+x_j$. The diagonal components σ_{ii} are called *normal* components of stress, and off-diagonal ones, σ_{ij} with $i \neq j$, are the *shear* components. σ_{ij} are the components of a second-rank tensor which can be presented by a 3×3

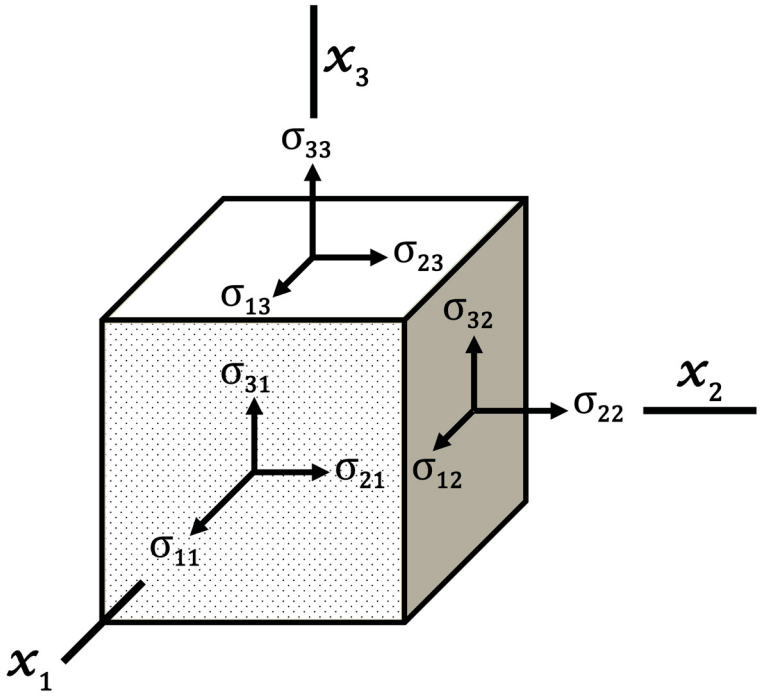

Figure 2.1: The different force contributions which act on the faces of a unit cube in a homogeneously stressed body.

matrix,[1]

$$\underline{\boldsymbol{\sigma}} = \begin{bmatrix} \sigma_{11} & \sigma_{12} & \sigma_{13} \\ \sigma_{21} & \sigma_{22} & \sigma_{23} \\ \sigma_{31} & \sigma_{32} & \sigma_{33} \end{bmatrix} . \tag{2.1}$$

A positive σ_{ii} component corresponds to tensile stress whereas a negative value expresses a compressive stress. This is the standard definition in modern textbooks on elasticity. However, the opposite sign convention is sometimes used.

In the equilibrium state, each infinitesimal volume element of a solid body must be in mechanical equilibrium. This means that no net force can act on the element, *i.e.*,

$$\sum_{j=1}^{3} \sigma_{ij} + f_i = 0 \,, \tag{2.2}$$

where f_i is the ith component of the external force per unit area. Also, no net torque can act on the element, then

$$\sigma_{ij} = \sigma_{ji} \,. \tag{2.3}$$

[1]In this thesis, bold letters are reserved for vector objects and single and double underlined bold letters indicate second- and higher-rank tensor objects, respectively.

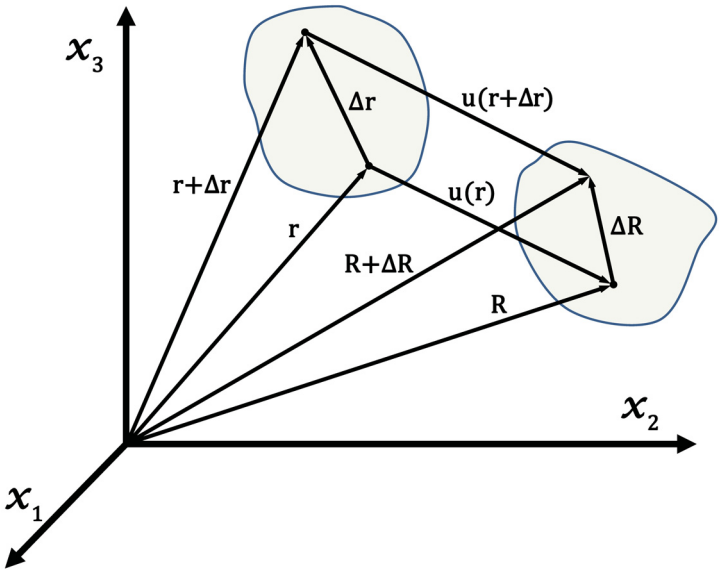

Figure 2.2: A mathematical model for deformation: A point initially located at position $\mathbf{r}$ is displaced by $\mathbf{u}(\mathbf{r})$ to the final position $\mathbf{R}$.

Thus, homogeneous stress can be represented by a symmetric matrix in the absence of body torques.

It should be noticed that stress has a matrix presentation like the dielectric or magnetic susceptibility, but it is not a crystal property. It simply indicates the force impressed on a crystal.

2.2 Strain

In order to understand the response of a solid body to external stresses, first of all we need to give a mathematical description of the solid's deformation.

Consider a solid body in an arbitrary starting configuration, which is taken as a reference. Assume a particle occupies in the reference configuration the point defined by the vector $\mathbf{r} = \sum_{i=1}^{3} x_i \hat{n}_i$. x_i coordinates are called *Lagrangian* coordinates. When the body is under stress, it is displaced such that a particle at point $\mathbf{r}$ moves to a new position $\mathbf{R} = \sum_{i=1}^{3} X_i \hat{n}_i$, as shown in Figure 2.2. The difference, $\mathbf{u}(\mathbf{r}) = \mathbf{R} - \mathbf{r}$, is the *displacement* of the particle and is expressed as a function of $\mathbf{r}$. This defines a vector field in the region occupied by the body in the reference configuration. Consider now a neighboring particle located at $\mathbf{r} + \Delta\mathbf{r}$. In the displaced configuration, the position of this point is

$$\mathbf{R} + \Delta\mathbf{R} = \mathbf{r} + \Delta\mathbf{r} + \mathbf{u}(\mathbf{r} + \Delta\mathbf{r}) \,, \tag{2.4}$$

therefore one can write

$$\Delta\mathbf{R} = \Delta\mathbf{r} + \mathbf{u}(\mathbf{r} + \Delta\mathbf{r}) - \mathbf{u}(\mathbf{r}), \tag{2.5}$$

and, for each component:

$$\Delta X_i = \Delta x_i + u_i(\mathbf{r} + \Delta\mathbf{r}) - u_i(\mathbf{r}). \tag{2.6}$$

If $\Delta\mathbf{r}$ is small enough, the second term in the right-hand side of the previous equation can be written as

$$u_i(\mathbf{r} + \Delta\mathbf{r}) - u_i(\mathbf{r}) \simeq \sum_{j=1}^{3} \frac{\partial u_i(\mathbf{r})}{\partial x_j} \Delta x_j. \tag{2.7}$$

For small displacements, it is convenient to replace $\Delta\mathbf{r}$ by the infinitesimal $d\mathbf{r}$, and to write the approximation as an equality. By defining the displacement-gradient matrix $\underline{\boldsymbol{\alpha}}$ as

$$\alpha_{ij} = \frac{\partial u_i(\mathbf{r})}{\partial x_j}, \tag{2.8}$$

each component in the new configuration, Eq. (2.6), becomes

$$\Delta X_i = \Delta x_i + \sum_{j=1}^{3} \alpha_{ij}\, \Delta x_j, \tag{2.9}$$

and we may write Eq. (2.9) in matrix notation

$$d\mathbf{X} = (\underline{\mathbf{I}} + \underline{\boldsymbol{\alpha}})\, d\mathbf{x}\,. \tag{2.10}$$

In this situation, the new deformed configuration $\mathbf{X}$, can be described by knowing the old reference configuration $\mathbf{x}$ and the matrix $\underline{\boldsymbol{\alpha}}$.

Now consider an infinitesimal neighborhood of the particle in the new configuration, labeled by the vector $\mathbf{R}$. The deformation of the neighborhood in a new configuration can be expressed in terms of the old configuration; therefore, the square of the length of $d\mathbf{R}$ can be written as:

$$\begin{aligned}
|d\mathbf{R}|^2 &= d\mathbf{R}\cdot d\mathbf{R} = d\mathbf{X}^T d\mathbf{X} \\
&= d\mathbf{x}^T(\underline{\mathbf{I}} + \underline{\boldsymbol{\alpha}}^T)(\underline{\mathbf{I}} + \underline{\boldsymbol{\alpha}})\, d\mathbf{x} = d\mathbf{x}^T(\underline{\mathbf{I}} + 2\underline{\boldsymbol{\eta}})\, d\mathbf{x} \\
&= d\mathbf{x}^T d\mathbf{x} + d\mathbf{x}^T 2\underline{\boldsymbol{\eta}}\, d\mathbf{x} = d\mathbf{r}\cdot d\mathbf{r} + d\mathbf{x}^T 2\underline{\boldsymbol{\eta}}\, d\mathbf{x} \\
&= |d\mathbf{r}|^2 + d\mathbf{x}^T 2\underline{\boldsymbol{\eta}}\, d\mathbf{x}\,,
\end{aligned} \tag{2.11}$$

where $\underline{\boldsymbol{\eta}} = \frac{1}{2}\left(\underline{\boldsymbol{\alpha}} + \underline{\boldsymbol{\alpha}}^T + \underline{\boldsymbol{\alpha}}^T\underline{\boldsymbol{\alpha}}\right)$, or in index notation,

$$\eta_{ij} = \frac{1}{2}\left(\alpha_{ij} + \alpha_{ji} + \sum_{k=1}^{3} \alpha_{ki}\,\alpha_{kj}\right). \tag{2.12}$$

This defines the symmetric matrix $\underline{\boldsymbol{\eta}}$, known as the *Lagrangian* strain matrix. In general, strain is a description of deformation in terms of relative displacements of particles in the body. In particular, the Lagrangian strain allows to evaluate how much the new configuration differs from the reference one, Eq. (2.11). The Lagrangian strain, $\underline{\boldsymbol{\eta}}(\mathbf{r})$, describes the deformation of the infinitesimal neighborhood of $\mathbf{r}$. The deformation of a solid is called homogeneous if $\underline{\boldsymbol{\eta}}$ is constant. Obviously, a necessary and sufficient condition for the deformation to be homogeneous is that the α_{ij} are constant, or equivalently, that $\mathbf{u}$ varies linearly with $\mathbf{r}$.

We further define the symmetric and antisymmetric matrix $\underline{\boldsymbol{\epsilon}}$ and $\underline{\boldsymbol{\omega}}$, respectively, by

$$\begin{aligned} \epsilon_{ij} &= \frac{1}{2}(\alpha_{ij} + \alpha_{ji}) \\ \omega_{ij} &= \frac{1}{2}(\alpha_{ij} - \alpha_{ji})\,. \end{aligned} \tag{2.13}$$

Therefore $\alpha_{ij} = \epsilon_{ij} + \omega_{ij}$, and

$$\eta_{ij} = \epsilon_{ij} + \frac{1}{2}\sum_{k=1}^{3}(\epsilon_{ik}\,\epsilon_{kj} + \epsilon_{ik}\,\omega_{kj} - \omega_{ik}\,\epsilon_{kj} - \omega_{ik}\,\omega_{kj}). \tag{2.14}$$

If $|\epsilon_{ij}| \ll 1$ and $|\omega_{ij}| \ll 1$ for all i, j, then $\underline{\boldsymbol{\epsilon}}$ is an approximation to $\underline{\boldsymbol{\eta}}$. If $\underline{\boldsymbol{\epsilon}} = 0$, then $\underline{\boldsymbol{\alpha}} = \underline{\boldsymbol{\omega}}$, and therefore $d\mathbf{X} = (\underline{\mathbf{I}} + \underline{\boldsymbol{\omega}})\,d\mathbf{x}$. In this situation, the squared length of the $d\mathbf{R}$ vector can be calculated as

$$\begin{aligned} |d\mathbf{R}|^2 &= d\mathbf{X}^T d\mathbf{X} = d\mathbf{x}^T(\underline{\mathbf{I}} + \underline{\boldsymbol{\omega}})^T(\underline{\mathbf{I}} + \underline{\boldsymbol{\omega}})d\mathbf{x} \\ &= d\mathbf{x}^T(\underline{\mathbf{I}} + \underline{\boldsymbol{\omega}} + \underline{\boldsymbol{\omega}}^T + \underline{\boldsymbol{\omega}}^T\underline{\boldsymbol{\omega}})d\mathbf{x} \\ &= d\mathbf{x}^T d\mathbf{x} = |d\mathbf{r}|^2\,. \end{aligned} \tag{2.15}$$

Here, we have used $\underline{\boldsymbol{\omega}} + \underline{\boldsymbol{\omega}}^T = 0$ by definition, and we have neglected the second order term in $\underline{\boldsymbol{\omega}}$. From Eq. (2.15), $\underline{\boldsymbol{\omega}}$ is identified as the part of the deformation that does not change the distance between the elements of a solid body. This is exactly what one would expect from a rotation. Thus, $\underline{\boldsymbol{\omega}}$ is defined as the *rotation* strain matrix, while $\underline{\boldsymbol{\epsilon}}$ is known as the *physical* strain. If we are interested to know how much a given displacement changes upon deformation, it is enough to

take into account the physical strain tensor only. In this case, we can write the Lagrangian strain is

$$\underline{\boldsymbol{\eta}} = \underline{\boldsymbol{\epsilon}} + \frac{1}{2}\underline{\boldsymbol{\epsilon}}^2. \tag{2.16}$$

This expression for $\underline{\boldsymbol{\eta}}$ describes a solid body that is free of rotations, however this physical freedom has no effect on the calculation of elastic constants.

As the counterpart of the Lagrangian strain, the Lagrangian stress [36] $\underline{\boldsymbol{\tau}}$ is defined as

$$\underline{\boldsymbol{\tau}} = \det(\underline{\mathbf{I}} + \underline{\boldsymbol{\epsilon}})\,(\underline{\mathbf{I}} + \underline{\boldsymbol{\epsilon}})^{-1} \cdot \underline{\boldsymbol{\sigma}} \cdot (\underline{\mathbf{I}} + \underline{\boldsymbol{\epsilon}})^{-1}\,, \tag{2.17}$$

where $\underline{\boldsymbol{\sigma}}$ is the physical stress, as discussed in Section 2.1, and the dot $(\cdot)$ indicates a matrix product.

2.3 Hooke's Law

Hooke's law states that strain and stress in a solid body are linearly dependent. This law is valid only for a small amount of stress which is called *linear-elastic* regime. This relationship can be written in terms of Lagrangian strain and Lagrangian stress, as

$$\underline{\boldsymbol{\eta}} = \underline{\underline{\mathbf{s}}} \cdot \underline{\boldsymbol{\tau}}\,, \tag{2.18}$$

where $\underline{\underline{\mathbf{s}}}$ is a forth-rank tensor constant, called *elastic-compliance* constant, or shortly *compliance* constant. As an alternative, Hooke's law can be written as

$$\underline{\boldsymbol{\tau}} = \underline{\underline{\mathbf{c}}} \cdot \underline{\boldsymbol{\eta}}\,, \qquad \underline{\underline{\mathbf{c}}} = \underline{\underline{\mathbf{s}}}^{-1}, \tag{2.19}$$

where $\underline{\underline{\mathbf{c}}}$ is the *elastic-stiffness* constant or, in short, the *stiffness*. The explicit form of Hooke's law for different components is

$$\eta_{ij} = \sum_{k,l=1}^{3} s_{ijkl}\,\tau_{kl}\,. \tag{2.20}$$

Stress components can also be expressed in terms of the strain by

$$\tau_{ij} = \sum_{k,l=1}^{3} c_{ijkl}\,\eta_{kl}\,. \tag{2.21}$$

s_{ijkl}, or c_{ijkl}, are in total 81 independent elastic constants.

As already discussed in Sections 2.1 and 2.2, $\underline{\boldsymbol{\eta}}$ and $\underline{\boldsymbol{\tau}}$ are symmetric matrices. Therefore, in order to have symmetric matrices on both sides of Eqs. (2.20) and (2.21), the tensors $\underline{\underline{\mathbf{s}}}$ and $\underline{\underline{\mathbf{c}}}$ must fulfill the following symmetry conditions:

$$s_{ijkl} = s_{ijlk}\,, \quad s_{ijkl} = s_{jikl}\,, \tag{2.22}$$

and

$$c_{ijkl} = c_{ijlk}\,, \quad c_{ijkl} = c_{jikl}\,. \tag{2.23}$$

Equations (2.22) and (2.23) reduce the number of independent elastic constants from 81 to 36.

The symmetry of s_{ijkl} and c_{ijkl} in ij and kl makes it possible to represent them in a matrix notation instead of a forth-rank tensor. In this notation, which is known as *Voigt* notation, both Lagrangian stress and Lagrangian strain matrices are represented in form of a vector instead of a matrix and their components are written with a single index running from 1 to 6,

$$\begin{bmatrix} \tau_{11} & \tau_{12} & \tau_{13} \\ \tau_{12} & \tau_{22} & \tau_{23} \\ \tau_{13} & \tau_{23} & \tau_{33} \end{bmatrix} = \begin{bmatrix} \tau_1 & \tau_6 & \tau_5 \\ \tau_6 & \tau_2 & \tau_4 \\ \tau_5 & \tau_4 & \tau_3 \end{bmatrix} \Longrightarrow \begin{bmatrix} \tau_1 \\ \tau_2 \\ \tau_3 \\ \tau_4 \\ \tau_5 \\ \tau_6 \end{bmatrix}, \tag{2.24}$$

and

$$\begin{bmatrix} \eta_{11} & \eta_{12} & \eta_{13} \\ \eta_{12} & \eta_{22} & \eta_{23} \\ \eta_{13} & \eta_{23} & \eta_{33} \end{bmatrix} = \begin{bmatrix} \eta_1 & \frac{1}{2}\eta_6 & \frac{1}{2}\eta_5 \\ \frac{1}{2}\eta_6 & \eta_2 & \frac{1}{2}\eta_4 \\ \frac{1}{2}\eta_5 & \frac{1}{2}\eta_4 & \eta_3 \end{bmatrix} \Longrightarrow \begin{bmatrix} \eta_1 \\ \eta_2 \\ \eta_3 \\ \eta_4 \\ \eta_5 \\ \eta_6 \end{bmatrix}. \tag{2.25}$$

The following relations hold between Voigt and Cartesian indices:

ij	11	22	33	23	13	12
α	1	2	3	4	5	6

Using Voigt notation, Eqs. (2.20) and (2.21) can be simplified as

$$\eta_\alpha = \sum_{\beta=1}^{6} s_{\alpha\beta}\,\tau_\beta \tag{2.26}$$

and

$$\tau_\alpha = \sum_{\beta=1}^{6} c_{\alpha\beta}\,\eta_\beta\,, \tag{2.27}$$

respectively.

In the new representation, the compliance tensor ($\underline{\underline{\boldsymbol{s}}}$) can be expressed by the compliance matrix

$$\underline{\underline{\boldsymbol{s}}} = \begin{bmatrix} s_{11} & s_{12} & s_{13} & s_{14} & s_{15} & s_{16} \\ s_{12} & s_{22} & s_{23} & s_{24} & s_{25} & s_{26} \\ s_{13} & s_{23} & s_{33} & s_{34} & s_{35} & s_{36} \\ s_{14} & s_{24} & s_{34} & s_{44} & s_{45} & s_{46} \\ s_{15} & s_{25} & s_{35} & s_{45} & s_{55} & s_{56} \\ s_{16} & s_{26} & s_{36} & s_{46} & s_{56} & s_{66} \end{bmatrix}, \tag{2.28}$$

and the stiffness tensor $\underline{\underline{\boldsymbol{c}}}$ by the stiffness matrix

$$\underline{\underline{\boldsymbol{c}}} = \begin{bmatrix} c_{11} & c_{12} & c_{13} & c_{14} & c_{15} & c_{16} \\ c_{12} & c_{22} & c_{23} & c_{24} & c_{25} & c_{26} \\ c_{13} & c_{23} & c_{33} & c_{34} & c_{35} & c_{36} \\ c_{14} & c_{24} & c_{34} & c_{44} & c_{45} & c_{46} \\ c_{15} & c_{25} & c_{35} & c_{45} & c_{55} & c_{56} \\ c_{16} & c_{26} & c_{36} & c_{46} & c_{56} & c_{66} \end{bmatrix}. \tag{2.29}$$

In the reminder of this thesis, the Voigt notation will be assumed, unless explicitly stated otherwise. Note that $s_{\alpha\beta}$ and $c_{\alpha\beta}$ are not the components of a physical second-rank tensor, and so do not transform as such. For this reason, in order to transform them into another coordinate system, it is necessary to go back to the fourth-rank notation.

2.4 Linear and Non-Linear Elastic Constants

As mentioned in Section 2.3, Hooke's law is valid only in the linear-elastic limit. When a stress applied to a solid body is large enough, the body will pass the threshold of the linear-elastic limit. Therefore, Hooke's law must be generalized mathematically in order to cover both the linear and non-linear elastic regimes. For any type of deformation, the Lagrangian stress of the deformed crystal can be expressed as a power series of the Lagrangian strain, as

$$\boldsymbol{\tau} = \boldsymbol{\tau_0} + \underline{\underline{\mathbf{c}}}^{(2)} \cdot \boldsymbol{\eta} + \boldsymbol{\eta}^T \cdot \underline{\underline{\mathbf{c}}}^{(3)} \cdot \ \boldsymbol{\eta} + \cdots \tag{2.30}$$

where $\boldsymbol{\tau_0}$ is the Lagrangian stress of the reference configuration. If the reference crystal structure is chosen to be the equilibrium one, all $\boldsymbol{\tau_0}$ components vanish, because at equilibrium the crystal is stress free. $\underline{\underline{\mathbf{c}}}^{(2)}$ introduced in Eq. (2.30) coincides with $\underline{\underline{\mathbf{c}}}$ used in Section 2.3, while $\underline{\underline{\mathbf{c}}}^{(3)}$ is a three dimensional matrix in Voigt notation (corresponding to a sixth-rank symmetric tensor in Cartesian notation). By this definition, the third term of Eq. (2.30) is of order $\mathcal{O}(\eta^2)$ and, therefore, negligible for small deformations.

For every τ_{ij} component of the Lagrangian stress (returning to the Cartesian notation for a moment), we generalize Eq. (2.30) as

$$\tau_{ij} = \sum_{k,l=1}^{3} c_{ijkl}\,\eta_{kl} + \sum_{k,l,m,n=1}^{3} c_{ijklmn}\,\eta_{kl}\,\eta_{mn} + \cdots . \tag{2.31}$$

In Voigt notation, this equation can be rewritten as

$$\tau_{\alpha} = \sum_{\beta=1}^{3} c_{\alpha\beta}\,\eta_{\beta} + \sum_{\beta,\gamma=1}^{3} c_{\alpha\beta\gamma}\,\eta_{\beta}\,\eta_{\gamma} + \cdots . \tag{2.32}$$

Here, the coefficients $c_{\alpha\beta}$ and $c_{\alpha\beta\gamma}$ represent the second-order elastic constants (SOECs) and third-order elastic constants (TOECs), respectively. Therefore, according to Eq. (2.32), the elastic constants $c_{\alpha\beta}$ and $c_{\alpha\beta\gamma}$ can be derived using

$$c_{\alpha\beta} = \left.\frac{\partial \tau_{\alpha}}{\partial \eta_{\beta}}\right|_{\boldsymbol{\eta}=0} \tag{2.33}$$

and

$$c_{\alpha\beta\gamma} = \left.\frac{\partial^2 \tau_{\alpha}}{\partial \eta_{\beta}\partial \eta_{\gamma}}\right|_{\boldsymbol{\eta}=0}, \tag{2.34}$$

respectively, and the derivatives are calculated at the reference configuration where $\boldsymbol{\eta} = 0$.

The Lagrangian stress of a deformed crystal, τ_{α}, is defined as the first derivative of the *internal energy* with respect to the η_{α}, *i.e.*,

$$\tau_{\alpha} = \frac{1}{V_0}\frac{\partial E}{\partial \eta_{\alpha}} \tag{2.35}$$

where V_0 is the volume of the reference equilibrium structure.

Thus, Eqs. (2.33) and (2.34) can be expressed in terms of derivatives of the internal energy as

$$c_{\alpha\beta} = \left.\frac{1}{V_0}\frac{\partial^2 E}{\partial \eta_{\alpha}\partial \eta_{\beta}}\right|_{\boldsymbol{\eta}=0} \tag{2.36}$$

and

$$c_{\alpha\beta\gamma} = \left.\frac{1}{V_0}\frac{\partial^3 E}{\partial \eta_{\alpha}\partial \eta_{\beta}\partial \eta_{\gamma}}\right|_{\boldsymbol{\eta}=0} . \tag{2.37}$$

In this thesis, we denominate the procedure based on stress calculations (Eqs. (2.33) and (2.34)) as "*stress approach*". Correspondingly, the calculation of the elastic constants using Eqs. (2.36) and (2.37) will be referred to as "*energy approach*".

2.5 Polycrystalline Elastic Constants

A polycrystalline material consists of many single crystal grains which are oriented randomly. An isotropic system can be described completely by the bulk modulus B and the shear modulus G [34]. Both of these moduli can be calculated by averaging over SOECs. The Young modulus E and Poisson ratio are related to B and G by the following equations

$$E = \frac{9BG}{3B+G}\,, \tag{2.38}$$

and,

$$\nu = \frac{3B-2G}{2(3B+G)}\,. \tag{2.39}$$

The most appropriate way to determine the *ab initio* polycrystalline elastic moduli is to first calculate the single crystal elastic constants $c_{\alpha\beta}$ and/or $s_{\alpha\beta}$, and then to transform these data to macroscopic quantities by suitable averaging methods. Different methods have been proposed for averaging $c_{\alpha\beta}$ to obtain isotropic elastic constants. In the following, we will describe the three most widely used averaging methods for the bulk and shear moduli.

2.5.1 Voigt and Reuss Averaging Methods

In the Voigt averaging method [37] a uniform strain, while in the Reuss method [38] a uniform stress is assumed. The former is calculated using the elastic constants $c_{\alpha\beta}$ and the latter applying the elastic compliance $s_{\alpha\beta}$. In the Voigt approach, the general expressions for the bulk and shear moduli are

$$B_V = \frac{1}{9}\left[(c_{11}+c_{22}+c_{33})+2(c_{12}+c_{13}+c_{23})\right], \tag{2.40}$$

and

$$G_V = \frac{1}{15}\left[(c_{11}+c_{22}+c_{33})-(c_{12}+c_{13}+c_{23})+3(c_{44}+c_{55}+c_{66})\right]. \tag{2.41}$$

The corresponding expressions for the Reuss approach are

$$B_R = \left[(s_{11}+s_{22}+s_{33})+2(s_{12}+s_{13}+s_{23})\right]^{-1}\,, \tag{2.42}$$

$$G_R = 15\left[4(s_{11}+s_{22}+s_{33})-(s_{12}+s_{13}+s_{23})+3(s_{44}+s_{55}+s_{66})\right]^{-1}. \tag{2.43}$$

2.5.2 Hill's Averaging Method

Hill [39, 40] has shown that the Voigt and Reuss elastic moduli are the strict upper and lower bound, respectively. Thus, the Hill-averaged bulk and shear moduli can be determined from these upper and lower limits as

$$G_H = \frac{1}{2}(G_V + G_R), \tag{2.44}$$

$$B_H = \frac{1}{2}(B_V + B_R). \tag{2.45}$$

Alternatively, one may prefer to use geometric or harmonic means instead of the arithmetic average. In weakly anisotropic materials, all these average methods lead to similar mean values of B and G [34].

3 *Ab Initio* Methodology

In Chapter 2, we have seen that internal energy and stress are required for elastic-constant calculations. They are provided by *ab initio* codes which are interfaced with `ElaStic`. In order to obtain precise results, accurate total energies and/or stress tensors of deformed crystals are required. Therefore, this chapter is dedicated to the *ab initio* methodology, and it is organized as follows: The Hamiltonian of the many-body crystal system will be introduced; then, basics of density-functional theory and the solution of the Kohn-Sham equations will be presented.

3.1 Many-Body Crystal Hamiltonian

The non-relativistic many-body Hamiltonian $\hat{H}$, for a system containing N_e electrons and N_I nuclei, is given by

$$\begin{aligned}\hat{H} &= -\sum_{I=1}^{N_I}\frac{\hbar^2}{2M_I}\nabla^2_{\mathbf{R}_I}-\sum_{i=1}^{N_e}\frac{\hbar^2}{2m_e}\nabla^2_{\mathbf{r}_i} \\ &\quad +\frac{1}{2}\sum_{I\neq J}\frac{Z_I Z_J e^2}{|\mathbf{R}_I-\mathbf{R}_J|}+\frac{1}{2}\sum_{i\neq j}\frac{e^2}{|\mathbf{r}_i-\mathbf{r}_j|}-\sum_{i,I}\frac{Z_I e^2}{|\mathbf{r}_i-\mathbf{R}_I|}\,. \end{aligned} \tag{3.1}$$

Here, coordinates of nuclei and electrons are indicated by $\mathbf{R}$ and $\mathbf{r}$, respectively. Capital letters are used to label nuclei, while lower-case indices refer to electrons. Mass and charge of the I-th nucleus are M_I and $Z_I e$, while the electronic mass and charge are m_e and $-e$, respectively. The first and second term of Eq. (3.1) are the kinetic energy of nuclei and electrons. The third and fourth terms are the pairwise electrostatic nucleus-nucleus and electron-electron interactions, respectively. The last term corresponds to the electron-nuclei attraction.

In principle, all properties of a quantum mechanical system can be derived by solving the many-body Schrödinger equation,

$$\hat{H}\Psi(r,R)=E\Psi(r,R)\,, \tag{3.2}$$

where $r(\equiv \{\mathbf{r}_i\})$ and $R(\equiv \{\mathbf{R}_I\})$ represent all electrons and nuclei coordinates, respectively. Using the standard *adiabatic approximation* proposed by Born and Oppenheimer [41], the nuclear and electronic degrees of freedom are separated. As a consequence, an electronic wave-function, $\psi(r;R)$, is introduced, which satisfies the equation

$$\left[-\sum_{i=1}^{N_e}\frac{\hbar^2}{2m_e}\nabla^2_{\mathbf{r}_i}+V_{ee}+V_{eI}+V_{II}\right]\psi(r;R)=E_{\rm pes}(R)\,\psi(r;R)\;, \tag{3.3}$$

where, V_{ee}, V_{eI}, and V_{II} are the electron-electron, electron-ion, and ion-ion interaction potentials, respectively. $E_{\rm pes}(R)$ is the so-called Born-Oppenheimer *potential-energy surface* and corresponds to the ground-state energy of the electronic system in a fixed nuclei configuration R. The adiabatic approximation allows to reduce the complexity of the many-body problem. However, the resulting Eq. (3.3) can not be exactly solved in practical cases, *i.e.*, for systems consisting of more than a few electrons. Density-functional theory (DFT), which will be discussed in the next section, provides a useful framework which allows for practical calculations.

3.2 Density-Functional Theory

Density-functional theory is based on the Hohenberg-Kohn (HK) theorem [1], which states that there is a unique correspondence (apart from a trivial additive constant) between the external potential, $v_{\rm ext}(\mathbf{r})$, acting on an interacting electronic system and the ground-state electron density of the system, $n_{\rm GS}(\mathbf{r})$. Therefore, all properties of this systems can be written, in principle, as functionals of $n_{\rm GS}(\mathbf{r})$. In particular, this is true for the ground-state energy

$$E_{\rm GS}=E_{\rm GS}[n_{\rm GS}]\;.$$

Furthermore, the HK theorem states that the ground-state energy functional $E_{\rm GS}[n]$ is minimum for $n(\mathbf{r})=n_{\rm GS}(\mathbf{r})$. The previous statement allows for calculating $n_{\rm GS}(\mathbf{r})$ by direct minimization of the functional $E_{\rm GS}[n]$ with the condition that the total number of electrons, N_e, is preserved, *i.e.*,

$$\int n(\mathbf{r})\,d\mathbf{r}=N_e\;. \tag{3.4}$$

The minimization can be performed using the Euler-Lagrange multipliers formalism and leads to

$$\delta\left[E_{\rm GS}[n]-\mu\left(\int n(\mathbf{r})\,d\mathbf{r}-N_e\right)\right]=\int\delta n(\mathbf{r})\left\{\frac{\delta E_{\rm GS}[n]}{\delta n}-\mu\right\}d\mathbf{r}=0\,, \tag{3.5}$$

where the Lagrange multiplier μ has also the meaning of chemical potential.

The ground-state energy functional can be written as

$$E_{\rm GS}[n] \equiv E[n] = T[n] + E_{ee}[n] + E_{\rm ext}[n] \; ,$$

where $T[n]$ and $E_{ee}[n]$ are the kinetic-energy and electron-electron interaction energy functionals, respectively, and

$$E_{\rm ext}[n] = \int v_{\rm ext}(\mathbf{r})\, n(\mathbf{r})\, d\mathbf{r} \; .$$

The exact expression of $E[n]$ is not known, because $T[n]$ and $E_{ee}[n]$ are not known. However, $E[n]$ can be written in terms of known quantities as

$$\begin{aligned} E[n] &= T_s[n] + E_H[n] + E_{\rm ext}[n] \\ &\quad + \underbrace{T[n] - T_s[n] + E_{ee}[n] - E_H[n]}_{E_{xc}[n]} \; , \end{aligned} \tag{3.6}$$

where

- $T_s[n]$ is the kinetic-energy functional for a *non-interacting* electron system with density $n(\mathbf{r})$;[1]
- $E_H[n]$ is the Hartree energy

$$E_H[n] = \frac{e^2}{2} \iint \frac{n(\mathbf{r})\, n(\mathbf{r}')}{|\mathbf{r} - \mathbf{r}'|}\, d\mathbf{r}\, d\mathbf{r}' = \frac{1}{2} \int v_H(\mathbf{r})\, n(\mathbf{r})\, d\mathbf{r} \; , \tag{3.7}$$

  where $v_H(\mathbf{r})$ is the Hartree potential;
- all the unknown many-body contributions of $T[n]$ and $E_{ee}[n]$ are incorporated into $E_{xc}[n]$, the so-called *exchange-correlation* energy functional.

3.2.1 Kohn-Sham Equations

Following the idea of Kohn and Sham [2], the explicit minimization of the ground-state energy functional in Eq. (3.6) leads to the expression

$$\int \delta n(\mathbf{r}) \left\{ \frac{\delta T_s[n]}{\delta n} + v_{\rm ext} + v_H + v_{xc} - \mu \right\} d\mathbf{r} = 0 \; , \tag{3.8}$$

where $v_{xc}(\mathbf{r})$ is the exchange-correlation potential, which is defined as

$$v_{xc}(\mathbf{r}) = \frac{\delta E_{xc}[n]}{\delta n(\mathbf{r})} \; . \tag{3.9}$$

[1] Here, we are following the notation which can be found in standard DFT textbooks [42, 43].

One can notice that Eq. (3.8) is mathematically equivalent to the equation which is obtained for a *non-interacting* electron system in the external (effective) potential

$$V_s(\mathbf{r}) = v_{\text{ext}}(\mathbf{r}) + v_H(\mathbf{r}) + v_{xc}(\mathbf{r}). \tag{3.10}$$

The solution for the non-interacting system is known, and the electron density which minimizes the ground-state energy functional can be exactly expressed in terms of a set of single-particle wave-functions, $\varphi_i(\mathbf{r})$, which are the solutions of the Kohn-Sham (KS) equations

$$h(\mathbf{r})\,\varphi_i(\mathbf{r}) = \left[-\frac{\hbar^2}{2m}\nabla^2 + V_s(\mathbf{r})\right]\varphi_i(\mathbf{r}) = \epsilon_i\,\varphi_i(\mathbf{r}), \tag{3.11}$$

where ϵ_i are the single-particle KS energies. However, the effective potential $V_s(\mathbf{r})$ is itself a functional of the electron density. This means that the one-particle Schrödinger equations in Eq. (3.11) must be solved self-consistently, according to the following steps:

a) The KS equations for the non-interacting electrons in the potential $V_s(\mathbf{r})$ obtained from a previous iteration step are solved.

b) The electron density of the system is calculated from the KS one-electron wave-functions obtained in (a) as

$$n(\mathbf{r}) = \sum_{i=1}^{N_e} |\varphi_i(\mathbf{r})|^2. \tag{3.12}$$

c) The effective potential $V_s(\mathbf{r})$ is updated using the new electron density given by Eq. (3.12).

The iteration procedure (a)-(c) is repeated until the desired convergence is achieved.

3.2.2 Exchange-Correlation Functionals

An approximation for the exchange-correlation (XC) energy functional defined in Eq. (3.6) must be chosen for any practical calculation of the ground-state energy of an electronic system. In this thesis, we use XC functionals obtained in the local-density and generalized-gradient approximations.

Within the local-density approximation (LDA) [44, 45, 46], the XC energy functional is

$$E_{xc}^{\text{LDA}}[n] = \int \epsilon_{xc}(n(\mathbf{r}))\; n(\mathbf{r})\, d\mathbf{r}\;, \tag{3.13}$$

where $\epsilon_{xc}(y)$ is the exchange-correlation energy density of homogeneous electron system with (constant) electron density y. Applications of LDA functionals are successful for systems at the limit of high density and for slowly varying electron density. However, LDA typically overestimates crystal cohesive and molecular binding energies and it is not well suited for strongly correlated systems.

Beyond LDA, we used the generalized-gradient approximation (GGA) proposed by Perdew, Burke and Enzerhof (PBE) [47]. In this case, the exchange-correlation functional depends not only on the electron density $n(\mathbf{r})$, but also on its gradients, $\nabla n(\mathbf{r})$. The general expression for the XC energy within this GGA is

$$E_{xc}^{\mathrm{GGA}}[n] = \int \epsilon_x(n(\mathbf{r}))\; F_{xc}(n, \nabla n)\, n(\mathbf{r})\, d\mathbf{r}, \tag{3.14}$$

where, $\epsilon_x(y)$ is the exchange-energy density of the uniform electron gas with density y, and F_{xc} is a dimensionless factor explicitly dependent on the density gradient. In this thesis, we also use the implementation of the PBE energy functional in the slightly revised form PBEsol [48]. The latter functional improves the equilibrium properties of densely-packed solids and their surfaces, while it is typically worse than PBE for dissociation or cohesive energies.

3.3 Solving the KS Equations for a Crystal

In order to solve the KS equations, a convenient wave-function representation should be introduced to reduce the KS equations to standard linear algebra. In a crystal, due to the periodicity of the effective potential, the single-particle KS wave-functions can be labeled by the wave-vector $\mathbf{k}$. Therefore, if a set of basis functions $\{\phi_j^{\mathbf{k}}(\mathbf{r})\}$ is chosen, a KS wave-function can be written as

$$\varphi_{\mathbf{k}}(\mathbf{r}) = \sum_j C_j^{\mathbf{k}}\, \phi_j^{\mathbf{k}}(\mathbf{r})\,, \tag{3.15}$$

where the $C_j^{\mathbf{k}}$ are the expansion coefficients. Thus, the KS equations, Eq. (3.11), are transformed into a *secular equation*, *i.e.*, a generalized matrix eigenvalue problem of the form

$$\sum_j \left(H_{ij}^{\mathbf{k}} - \epsilon_{\mathbf{k}}\, S_{ij}^{\mathbf{k}}\right)\; C_j^{\mathbf{k}} = 0\,, \tag{3.16}$$

where $H_{ij}^{\mathbf{k}}$ are the matrix elements of the single-particle KS Hamiltonian $h(\mathbf{r})$,

$$H_{ij}^{\mathbf{k}} = \int \left[\phi_i^{\mathbf{k}}(\mathbf{r})\right]^*\, h(\mathbf{r})\; \phi_j^{\mathbf{k}}(\mathbf{r})\, d\mathbf{r}\,, \tag{3.17}$$

and $S_{ij}^{\mathbf{k}}$ denote the overlap matrix elements, which are defined as

$$S_{ij}^{\mathbf{k}} = \int \left[\phi_i^{\mathbf{k}}(\mathbf{r})\right]^* \phi_j^{\mathbf{k}}(\mathbf{r})\, d\mathbf{r} \ . \tag{3.18}$$

The KS wave-functions are rapidly varying in the region close to the nuclei. This fact must be taken into account for the choice of both the basis functions and the method of solution of the secular equation. The sets of basis functions which are used in this thesis are presented in the next sections.

3.3.1 Plane-Wave Basis Set and Pseudo-Potential Method

The periodicity of the KS wave-functions, $\varphi_{\mathbf{k}}(\mathbf{r})$, in a crystal, suggests to use a basis function consisting of plane waves (PWs). In this representation, the functions $\varphi_{\mathbf{k}}(\mathbf{r})$ are given as

$$\varphi_{\mathbf{k}}(\mathbf{r}) = \sum_{\mathbf{G}} C_{\mathbf{k}}(\mathbf{G})\, \phi_{\mathbf{k}+\mathbf{G}}(\mathbf{r}) = \frac{1}{\sqrt{V}} \sum_{\mathbf{G}} C_{\mathbf{k}}(\mathbf{G})\, e^{i(\mathbf{k}+\mathbf{G})\cdot\mathbf{r}} \ , \tag{3.19}$$

where $\mathbf{G}$ is a reciprocal-lattice vector, V is the unit-cell volume, and

$$\phi_{\mathbf{k}+\mathbf{G}}(\mathbf{r}) = \frac{1}{\sqrt{V}}\, e^{i(\mathbf{k}+\mathbf{G})\cdot\mathbf{r}} \ . \tag{3.20}$$

In principle, the number of reciprocal-lattice vectors in the expansion in Eq. (3.19) is infinite. This leads to an infinite number of matrix elements in the secular equation which would make numerical solution impossible. The infinite-dimensional problem can be reduced to a finite one by introducing a kinetic-energy cut-off, $E_{\mathrm{cut}}^{\mathrm{wfc}}$, and restricting the basis set such that

$$\frac{\hbar^2}{2m_e}|\mathbf{k}+\mathbf{G}|^2 < E_{\mathrm{cut}}^{\mathrm{wfc}} \ . \tag{3.21}$$

Plane-wave basis sets are mostly used in connection with DFT implementations that rely on the pseudo-potential method. The main idea behind this method is that some properties, such as chemical reactivity or bond formations, mostly depend on the behavior of the valence electrons. This allows to consider core electrons and nucleus as a rigid core unit. In this way, the strong Coulomb potential of the nucleus, responsible for the large oscillations of the wave-functions, can be replaced by the weaker "pseudo" potential generated by the core unit. Within this approximation, the use of a PW basis set of reasonable size becomes feasible.

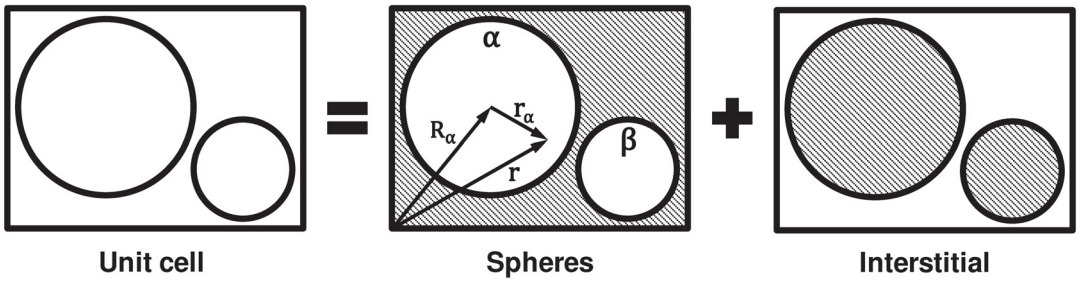

Figure 3.1: Splitting of the unit-cell volume into the interstitial region and non-overlapping spheres in the APW methods.

3.3.2 Augmented Plane-Wave Basis Sets

An efficient way to deal with the strong oscillations of the wave-functions around the nuclei is the choice of a basis set made of augmented plane waves (APWs) [49]. The straightforward idea, illustrated in Figure 3.1, is to partition the unit cell of the crystal in two parts, namely *i*) a region consisting of non-overlapping atomic spheres ($S = \sum_\alpha S_\alpha$) centered at nuclear positions, and *ii*) an interstitial region (I). Inside the spheres, the basis set is built with atomic-like functions, while, in the interstitial region, plane waves are utilized. Thus, the APW basis set is

$$\phi^{\mathrm{APW}}_{\mathbf{k}+\mathbf{G}}(\mathbf{r}) = \begin{cases} \dfrac{1}{\sqrt{V}}\, e^{i(\mathbf{k}+\mathbf{G})\cdot\mathbf{r}} & \text{if } \mathbf{r} \in I \\ \displaystyle\sum_{l=0}^{l_{\max}} \sum_{m=-l}^{+l} A^\alpha_{lm}(\mathbf{k}+\mathbf{G})\, u_l(r_\alpha, E)\, Y_{lm}(\hat{r}_\alpha) & \text{if } \mathbf{r} \in S_\alpha\,. \end{cases} \quad (3.22)$$

Here, $u_l(r_\alpha, E)$ is a radial wave-function, $Y_{lm}(\hat{r}_\alpha)$ are spherical harmonics, and the coefficients $A^\alpha_{lm}(\mathbf{k}+\mathbf{G})$ are determined by imposing the continuity of the basis functions at the sphere boundary. The vector $\mathbf{r}_\alpha$ is defined in Figure 3.1. Notice that the radial wave-function $u_l(r_\alpha, E)$ is energy dependent. This means that the solution of the secular equation leads to a non-linear eigenvalue problem which is computationally very demanding. For more details about the APW method see Ref. [50].

Contrary to the pseudo-potential method, the use of APW-like basis sets allows the modern DFT implementations to deal with the *full electron-nucleus potential* without any restrictions. At the same time, APW based methods permit to treat explicitly all (*i.e.*, both valence and core) electrons.

In the following, other APW-based basis sets are briefly summarized.

Linearized Augmented Plane-Wave Method

In order to overcome the computational complexity of the APW method related to the explicit energy dependence of the basis functions, the linearized-augmented plane-wave (LAPW) method [51] was introduced. Here, the basis functions inside the atomic spheres in LAPW are

$$\phi^{\mathrm{LAPW}}_{\mathbf{k}+\mathbf{G}}(\mathbf{r}) = \sum_{l=0}^{l_{\max}} \sum_{m=-l}^{+l} \left[A^{\alpha}_{lm}(\mathbf{k}+\mathbf{G})\, u_l(r_\alpha, E_l) + B^{\alpha}_{lm}(\mathbf{k}+\mathbf{G})\, \dot{u}_l(r_\alpha, E_l)\right] Y_{lm}(\hat{r}_\alpha). \tag{3.23}$$

The main difference between the above equation and Eq. (3.22) is the presence of the energy derivative of the radial function in the solution inside the atomic spheres. This allows, the LAPW basis functions to be evaluated at a fixed trial energy, which depends only on the angular quantum number l. Thus, the solution of a non-linear eigenvalue problem is avoided [51].

Local Orbitals

Local orbitals (lo) have been introduced to the LAPW method to treat semi-core states [52]. These orbitals are completely confined within the muffin-tin spheres. For given quantum numbers lm, they are defined as

$$\phi^{\mathrm{lo}}_{lm}(\mathbf{r}) = \begin{cases} 0 & \text{if } \mathbf{r} \in I \\ \left[A_{lm}\, u_l(r_\alpha, E_l) + B_{lm}\, \dot{u}_l(r_\alpha, E_l) + C_{lm}\, u_l(r_\alpha, E_{\mathrm{lo}})\right] Y_{lm}(\hat{r}_\alpha) & \text{if } \mathbf{r} \in S_\alpha\,. \end{cases}$$

In the above equation, the radial function with the coefficient C_{lm} is evaluated at the linearization energy E_{lo} which corresponds to the semi-core state, while E_l is the trial energy of the corresponding LAPW function (Eq. (3.23)). The coefficient C_{lm} is chosen in such a way that the local-orbitals basis function vanishes at the muffin-tin sphere boundary. Further details about this topic can be found in Refs. [52, 50].

APW+lo Basis

The APW and LAPW+lo methods can be combined [53] by removing the energy derivative in the LAPW function, Eq. (3.23), and by adding local orbitals at the same energy. The variational freedom of the basis is improved in this way. Therefore, the so-called APW+lo consists of APW functions with fixed linearization energies plus local orbitals.

4 Implementation

In Chapter 2, we have discussed theoretically how second- and third-order elastic constants can be derived from energy and stress as a function of strain for a crystal structure. In the current chapter, we focus on this problem from the computationally point of view and present the **ElaStic** code, which is a code for elastic constant calculations for any crystal symmetry. This code is written in Python uses the program SGROUP as a symmetry and space-group calculator and utilizes the density functional codes **exciting**, WIEN2k, and Quantum ESPRESSO for energy and stress calculations.

This chapter is organized as follows. We present the algorithm of the **ElaStic** code, first. Then, we examine the accuracy of elastic-constant calculations and we show how their errors can be minimized. At the end, we show our calculated elastic constants for different crystal classes.

4.1 Algorithm

In this section, we describe the fully-automated procedure for the calculation of SOECs and TOECs used in **ElaStic** for any arbitrary crystal. As a starting point, we assume that the geometry of the crystal has been optimized with respect to both cell parameters and atomic positions, such that the equilibrium configuration is used as reference system. In this case, all the curves representing the energy as a function of strain have a minimum at zero strain. Correspondingly, the stress-strain curves pass through the origin. The flowchart of **ElaStic** shown in Figure 4.1, displays the single steps of the procedure:

i) *Specify the DFT code, method, and order of elastic constant*
One of the available computer packages **exciting**, WIEN2k, and Quantum ESPRESSO is chosen to perform the DFT calculations. Note that the addition of interfaces with other *ab initio* DFT codes to **ElaStic** is straightforward. **ElaStic** asks interactively about the method of calculation, *i.e.*,

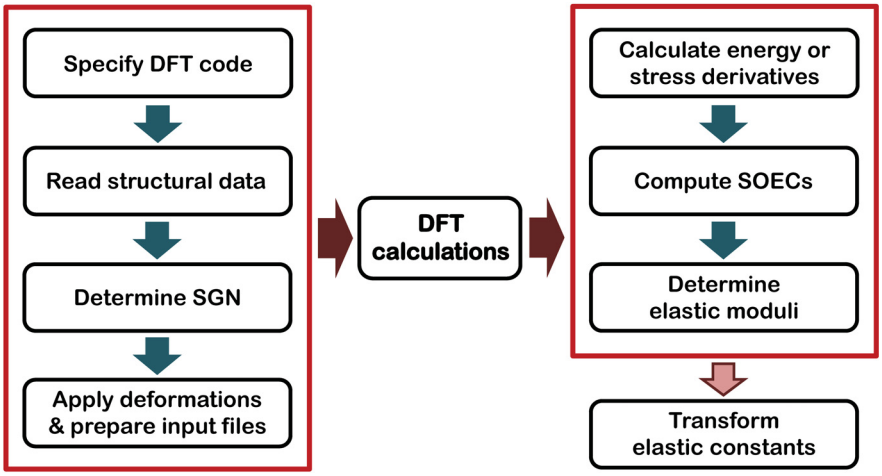

Figure 4.1: Flowchart of the procedure of the `ElaStic` code. The left side dependence on the used DFT code, while the right side in independent of it.

energy or stress, and order of elastic constant, *i.e.*, second or third order. A snapshot of the execution of `ElaStic` is shown in Figure 4.2.

ii) *Read the structure file*
An input file containing information about the structure (*e.g.*, crystal lattice, atomic positions) should be provided. For this purpose, `ElaStic` requires the input file which is used by the selected DFT code for a calculation at the equilibrium structure with relaxed atomic positions. The structural data contained in the input file are read by `ElaStic`.

iii) *Determine the space-group number*
In order to fully characterize the system crystallographically, the space-group number (SGN) must be determined. This is performed by the code SGROUP [54]. A classification of the different crystal structures including the corresponding number of independent SOECs/TOECs is given in Table A.1.

iv) *Deform the crystal and prepare input files*
Using this SGN information, a set of deformation types is specified. All deformation types utilized in `ElaStic` are shown in Tables 4.1 and 4.2 for the energy and stress approach, respectively.
For a given deformation type $\boldsymbol{\eta}_{\mathbf{V}}$ in Voigt notation, the deformation matrix

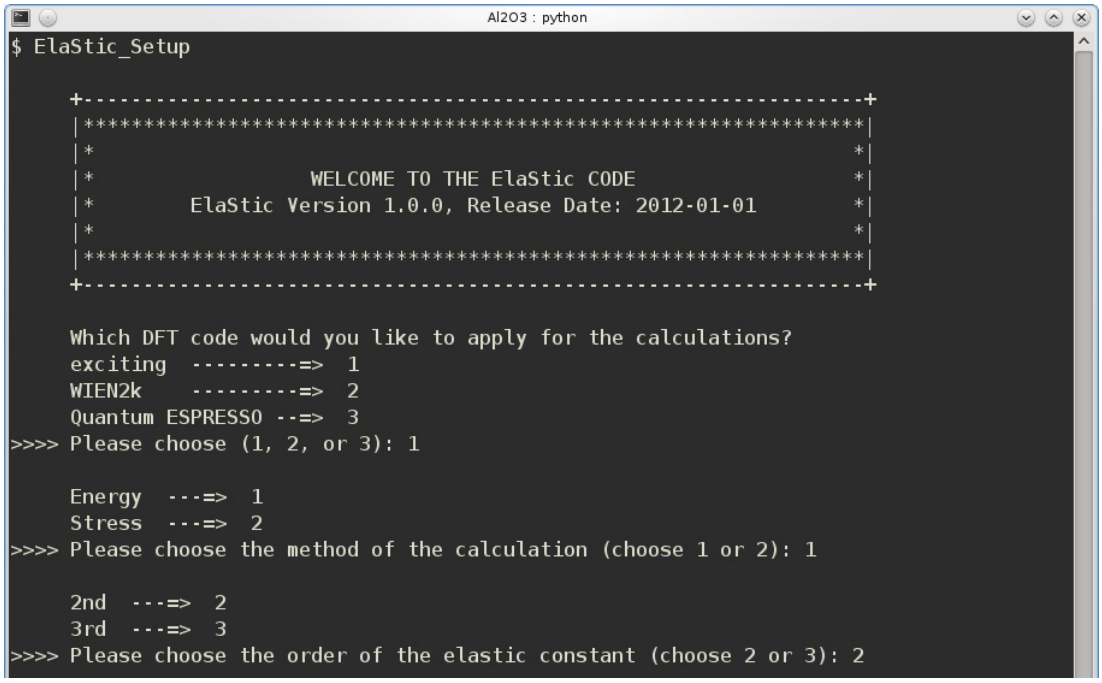

Figure 4.2: First snapshot of the `ElaStic` execution. `ElaStic` asks interactively about the DFT code, method, and order of elastic-constant calculations.

$\underline{\mathbf{D}}$ is constructed as follows:

$$\boldsymbol{\eta}_{\mathbf{V}} = \begin{bmatrix} \eta_1 \\ \eta_2 \\ \eta_3 \\ \eta_4 \\ \eta_5 \\ \eta_6 \end{bmatrix} \Longrightarrow \underline{\boldsymbol{\eta}} = \begin{bmatrix} \eta_1 & \frac{1}{2}\eta_6 & \frac{1}{2}\eta_5 \\ \frac{1}{2}\eta_6 & \eta_2 & \frac{1}{2}\eta_4 \\ \frac{1}{2}\eta_5 & \frac{1}{2}\eta_4 & \eta_3 \end{bmatrix} \Longrightarrow \underline{\mathbf{D}} = \underline{\mathbf{I}} + \underline{\boldsymbol{\eta}} \tag{4.1}$$

where $\underline{\mathbf{I}}$ is the identity matrix. Then, the primitive lattice vectors $\boldsymbol{a}$, $\boldsymbol{b}$, and $\boldsymbol{c}$ are transformed to the new vectors $\boldsymbol{a}'$, $\boldsymbol{b}'$, and $\boldsymbol{c}'$, respectively, as

$$\begin{bmatrix} \boldsymbol{a} \\ \boldsymbol{b} \\ \boldsymbol{c} \end{bmatrix} \cdot \underline{\mathbf{D}} = \begin{bmatrix} \boldsymbol{a} \\ \boldsymbol{b} \\ \boldsymbol{c} \end{bmatrix} \cdot \begin{bmatrix} 1+\eta_1 & \frac{1}{2}\eta_6 & \frac{1}{2}\eta_5 \\ \frac{1}{2}\eta_6 & 1+\eta_2 & \frac{1}{2}\eta_4 \\ \frac{1}{2}\eta_5 & \frac{1}{2}\eta_4 & 1+\eta_3 \end{bmatrix} = \begin{bmatrix} \boldsymbol{a}' \\ \boldsymbol{b}' \\ \boldsymbol{c}' \end{bmatrix} \tag{4.2}$$

Two input values, the maximum absolute value for the Lagrangian strain, $\eta_{\max}$, and the number of distorted structures with strain values between $-\eta_{\max}$ and $\eta_{\max}$, should be provided by the user at this stage, see Figure 4.3. Then, input files for the chosen DFT code are created for each deformed structure.

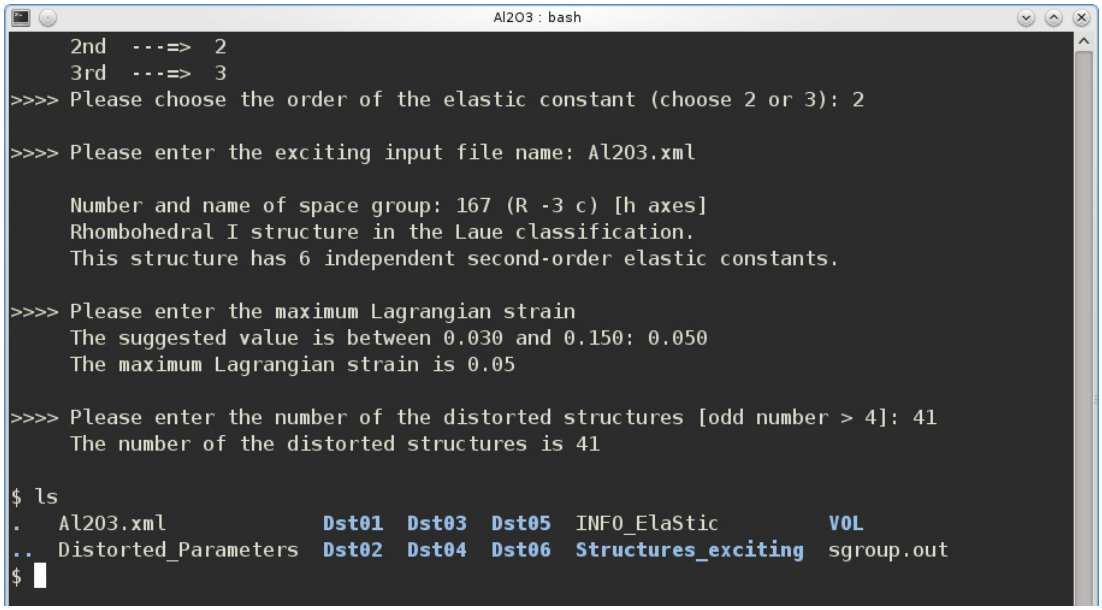

Figure 4.3: Second snapshot of the `ElaStic` execution. Using the SGN information, which is obtained by SGROUP, the crystal symmetry is specified. Then, the maximum absolute value of the Lagrangian strain, $\eta_{\max}$, and the number of distorted structures between $-\eta_{\max}$ and $\eta_{\max}$ are asked for. At the end, the input files for the chosen DFT code are created for each deformation type and different strain steps.

Table 4.1: Deformation types, expressed in the Voigt notation, that are used by `ElaStic` in the energy approach. Here, the generic (i-th) strain tensor is represented as a vector $\boldsymbol{\eta}^{(i)} = (\eta_1, \eta_2, \eta_3, \eta_4, \eta_5, \eta_6)$.

$\boldsymbol{\eta}^{(i)}$	η_1	η_2	η_3	η_4	η_5	η_6
$\boldsymbol{\eta}^{(1)}$	η	η	η	0	0	0
$\boldsymbol{\eta}^{(2)}$	η	0	0	0	0	0
$\boldsymbol{\eta}^{(3)}$	0	η	0	0	0	0
$\boldsymbol{\eta}^{(4)}$	0	0	η	0	0	0
$\boldsymbol{\eta}^{(5)}$	0	0	0	2η	0	0
$\boldsymbol{\eta}^{(6)}$	0	0	0	0	2η	0
$\boldsymbol{\eta}^{(7)}$	0	0	0	0	0	2η
$\boldsymbol{\eta}^{(8)}$	η	η	0	0	0	0
$\boldsymbol{\eta}^{(9)}$	η	0	η	0	0	0
$\boldsymbol{\eta}^{(10)}$	η	0	0	2η	0	0

Continued on next page

Table 4.1 – continued from previous page

$\boldsymbol{\eta}^{(i)}$	η_1	η_2	η_3	η_4	η_5	η_6
$\boldsymbol{\eta}^{(11)}$	η	0	0	0	2η	0
$\boldsymbol{\eta}^{(12)}$	η	0	0	0	0	2η
$\boldsymbol{\eta}^{(13)}$	0	η	η	0	0	0
$\boldsymbol{\eta}^{(14)}$	0	η	0	2η	0	0
$\boldsymbol{\eta}^{(15)}$	0	η	0	0	2η	0
$\boldsymbol{\eta}^{(16)}$	0	η	0	0	0	2η
$\boldsymbol{\eta}^{(17)}$	0	0	η	2η	0	0
$\boldsymbol{\eta}^{(18)}$	0	0	η	0	2η	0
$\boldsymbol{\eta}^{(19)}$	0	0	η	0	0	2η
$\boldsymbol{\eta}^{(20)}$	0	0	0	2η	2η	0
$\boldsymbol{\eta}^{(21)}$	0	0	0	2η	0	2η
$\boldsymbol{\eta}^{(22)}$	0	0	0	0	2η	2η
$\boldsymbol{\eta}^{(23)}$	0	0	0	2η	2η	2η
$\boldsymbol{\eta}^{(24)}$	$-\eta$	$\frac{1}{2}\eta$	$\frac{1}{2}\eta$	0	0	0
$\boldsymbol{\eta}^{(25)}$	$\frac{1}{2}\eta$	$-\eta$	$\frac{1}{2}\eta$	0	0	0
$\boldsymbol{\eta}^{(26)}$	$\frac{1}{2}\eta$	$\frac{1}{2}\eta$	$-\eta$	0	0	0
$\boldsymbol{\eta}^{(27)}$	η	$-\eta$	0	0	0	0
$\boldsymbol{\eta}^{(28)}$	η	$-\eta$	0	0	0	2η
$\boldsymbol{\eta}^{(29)}$	0	η	$-\eta$	0	0	2η
$\boldsymbol{\eta}^{(30)}$	η	0	$-\eta$	0	2η	0
$\boldsymbol{\eta}^{(31)}$	0	η	$-\eta$	0	0	2η
$\boldsymbol{\eta}^{(32)}$	η	η	$-\eta$	2η	2η	2η
$\boldsymbol{\eta}^{(33)}$	η	0	0	2η	2η	0
$\boldsymbol{\eta}^{(34)}$	0	η	0	2η	2η	0
$\boldsymbol{\eta}^{(35)}$	η	η	0	2η	2η	0
$\boldsymbol{\eta}^{(36)}$	η	η	0	2η	0	0
$\boldsymbol{\eta}^{(37)}$	η	η	$-\eta$	0	0	0
$\boldsymbol{\eta}^{(38)}$	η	η	η	-2η	-2η	-2η

Table 4.2: Same as Table 4.1 for the stress approach. The choice of deformation types is made according to Ref. [31].

$\tilde{\boldsymbol{\eta}}_i$	η_1	η_2	η_3	η_4	η_5	η_6
$\tilde{\boldsymbol{\eta}}^{(1)}$	η	2η	3η	4η	5η	6η
$\tilde{\boldsymbol{\eta}}^{(2)}$	-2η	η	4η	-3η	6η	-5η
$\tilde{\boldsymbol{\eta}}^{(3)}$	3η	-5η	$-\eta$	6η	2η	-4η
$\tilde{\boldsymbol{\eta}}^{(4)}$	-4η	-6η	5η	η	-3η	2η
$\tilde{\boldsymbol{\eta}}^{(5)}$	5η	4η	6η	-2η	$-\eta$	-3η
$\tilde{\boldsymbol{\eta}}^{(6)}$	-6η	3η	-2η	5η	-4η	η

v) *Perform ab initio calculations*
The energy or stress for the set of distorted structures created at the previous step is calculated by the selected DFT code. For each deformed structure, the internal degrees of freedom are optimized.

vi) *Calculate derivatives: Best polynomial fit*
A polynomial fitting procedure is applied to calculate the appropriate derivative of the energy or stress with respect to the Lagrangian strain at the equilibrium point. We discuss in Section 4.2, the polynomial-fit order and the range of distortion influence on the accuracy of the elastic constants.

vii) *Calculate elastic constants: Least-squares fit*
The coefficients of the best fitting polynomial achieved at the previous step can be expressed as a linear combination of the elastic constants. This procedure is repeated for a number of different deformation types, thus obtaining a set of linear equations which is (possibly) redundant in terms of the variables, *i.e.*, of the elastic constants. This set of linear equations is solved using the least-square fit method.

viii) *Calculate elastic moduli*
Appropriate averaging procedures can determine isotropic elastic constants such as the bulk, shear, and Young modulus as well as the Poisson ratio. This method of calculation is explained in Section 2.5.

ix) *Post processing: Transform elastic tensors*
In addition to the main code, `ElaStic` can be used to perform some post-processing of the obtained results. For further explanation readers are referred to Appendix B.

In order to have precise elastic constants one has to utilize a proper polynomial fit. Therefore, the next section is dedicated to the accuracy of the numerical differentiation.

4.2 Accuracy and Numerical Differentiation

The numerical accuracy of the elastic-constant calculations is strongly correlated with the numerical differentiation needed for the evaluation of Eqs. (2.33), (2.34), (2.36), and (2.37). In fact, we deal with a function (energy or stress) which is calculated only for a finite set of strain values. The evaluation of the numerical derivative of such a function is a non trivial issue. Several parameters play an important role, like the number and range of data points included in the fit and the kind of procedure used for the differentiation. In addition, the calculated data points suffer from intrinsic numerical uncertainties, as in the case of the numerical determination of energies and stresses in numerical *ab initio* DFT codes. In order to keep all these parameters under control and to estimate the numerical error of the *ab initio* calculation of energies and stresses, we have developed a special fitting procedure, which will be illustrated in the next section for a simple model. Then, the application of this procedure will be shown for some prototypical real materials. Here, only results for the energy approach are shown. However, the extension to the stress approach is straightforward.

4.2.1 Analytical Examples

In the following, we demonstrate the reliability of numerical second- and third-energy derivatives by two simple mathematical test cases. We assume that the energy *vs.* strain relationships are known and are *exactly* given as polynomial functions $E^{(2)} = \sum_i A_i^{(2)} \eta^i$ and $E^{(3)} = \sum_i A_i^{(3)} \eta^i$ with known $A_i^{(2)}$ and $A_i^{(3)}$ coefficients. The $E^{(2)}$ and $E^{(3)}$ functions are used for the second- and third-derivative calculations. In these examples, without loss of generality, we consider the highest degree of the polynomial's terms to be 6 and 8 for $E^{(2)}$ and $E^{(3)}$, respectively. The energy functions are

$$E^{(2)}(\eta) \;=\; 10^2\,\eta^2 + 10^4\,\eta^4 + 10^6\,\eta^6, \tag{4.3}$$

and

$$E^{(3)}(\eta) \;=\; 10^2\,\eta^2 - 10^3\,\eta^3 + 10^4\,\eta^4 + 10^5\,\eta^6 \; - 5\times 10^4\,\eta^7 + 10^7\,\eta^8. \tag{4.4}$$

All coefficients $A_i^{(2)}$ and $A_i^{(3)}$ are considered to be known. The coefficients $A_2^{(2)}$ and $A_3^{(3)}$, which are needed for the calculation of the second- and third-derivative at zero strain of the $E^{(2)}$ and $E^{(3)}$ energy-strain curves, are set as to $A_2^{(2)} = 100$

and $A_3^{(3)} = -1000$ (in arbitrary units), respectively. Obviously, in these special cases, the differentiation can be performed analytically; nevertheless, we calculate the second- and third-order derivatives with standard numerical techniques. Therefore, we generate a set of 51 equally-spaced strain points with symmetric distribution around the origin in the range $\eta \in [-0.1, 0.1]$ and $\eta \in [-0.15, 0.15]$ where the energy values are obtained using Eqs. (4.3) and (4.4), respectively. A polynomial fit yields the exact value of $A_2^{(2)}$ and $A_3^{(3)}$, if the order of the polynomial is equal to or larger than 6 and 8, respectively. The procedure can be repeated by taking into account only strain points in the range $\eta \in [-\eta_{\max}, \eta_{\max}]$ for different values of $\eta_{\max}$ (keeping the strain-point density fixed). The energy as a function of η calculated from Eqs. (4.3) and (4.4) and the values of $A_2^{(2)}$ and $A_3^{(3)}$ as a function of $\eta_{\max}$ are shown together in Figure 4.4.

Due to the choice of a symmetric distribution of strain points around the origin, the fitting polynomials of order n and $n+1$ with even n provide the same value of $A_2^{(2)}$ and $A_3^{(3)}$, as can be seen in the right panels of Figure 4.4. The calculated $A_2^{(2)}$ and $A_3^{(3)}$ using the quadratic and third-order polynomial fit are close to the correct value if only the $\eta_{\max}$ is less than 0.01 and 0.02 values, respectively. Similarly, the polynomial fit order $n = 4$ and $n = 5$ provides the correct result for $\eta_{\max}$ are less than 0.35 and 0.65, respectively, while the order $n = 6$ and $n = 7$ can be used for any value of $\eta_{\max}$.

The example considered up to here is very simple and somehow trivial. However, the situation is different considering that the values of the function $E(\eta)$ are not known exactly, but include some intrinsic numerical error introduced by calculating DFT total energies. We simulate the effect of such errors by adding a random noise of given amplitude to the polynomial function in Eqs. (4.3) and (4.4), as given by

$$\widetilde{E}_{\Delta}^{(2)}(\eta) = E^{(2)}(\eta) + \xi\Delta\left(E_{\max}^{(2)} - E_{\min}^{(2)}\right), \tag{4.5}$$

and

$$\widetilde{E}_{\Delta}^{(3)}(\eta) = E^{(3)}(\eta) + \xi\Delta\left(E_{\max}^{(3)} - E_{\min}^{(3)}\right), \tag{4.6}$$

respectively, where $E_{\max}$ and $E_{\min}$ are the maximum and minimum of the energy function in range of functions and ξ is a randomly generated number in range $\xi \in [-1, 1]$.

The calculated values of $A_2^{(2)}$ and $A_3^{(3)}$ for Δ =0, 0.001, 0.005, 0.02 and Δ =0, 0.0001, 0.0005, 0.0015, respectively, are shown in Figure 4.4. The main effect of the noise is to generate deviations from the unperturbed curves, strongly depending on the order of the polynomial fit, $\eta_{\max}$, and the noise amplitude. Analysis of the plots with different amount of noise reveals two different trends in dependence of the fitting order:

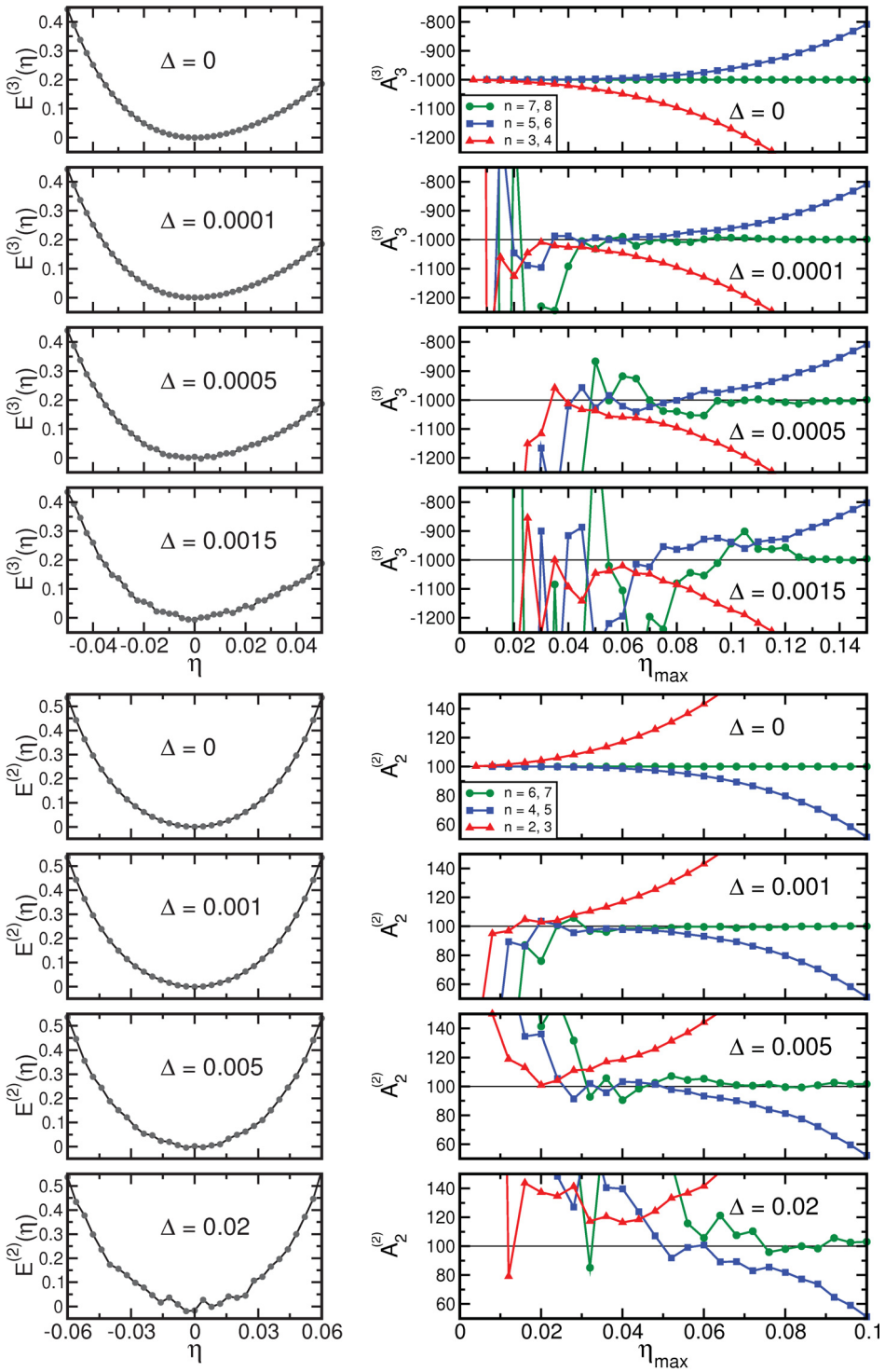

Figure 4.4: Energy as a function of strain η calculated from Eqs. (4.5) and (4.6) for different amplitudes of noise, $\Delta = 0$, 0.001, 0.005, and 0.02 and $\Delta = 0$, 0.0001, 0.0005, and 0.0015, receptively, and the corresponding coefficient $A_2^{(2)}$ and $A_3^{(3)}$ as obtained from different polynomial fits. In order to make the noise visible in the left panels, we draw energy curves in smaller energy range, compared to the right panels.

i) For small deformations, the best results for the derivative, *i.e.*, the closest ones to the imposed value, are obtained by using a low-order polynomial fit. The same result holds also if only a few data points are taken into account for the fit. The better values for the derivative arise in this case from the fact that the noise is partially averaged out using low-order polynomials, while high-order ones follow the noise much more, developing unphysical wiggles and, thus, yielding completely wrong coefficients.

ii) The results obtained for large deformations are very close to the correct value for high-order polynomial fits, in particular, in the strain regions where the curves in the right panel of Figure 4.4 are flat.

From this, we conclude that for a fixed order of the polynomial fit, the *exact* values of $A_2^{(2)}$ and $A_3^{(3)}$ are best reproduced in the region of $\eta_{\max}$, which are characterized by a *plateau* of the displayed curves. For instance, for the largest noise amplitude, for the range $\eta_{\max} > 0.08$ ($\eta_{\max} > 0.1225$) only the sixth-order (eight-order) polynomial fit gives *reasonable* results for the coefficient $A_2^{(2)}$ ($A_3^{(3)}$). Therefore, considering the fact that a low-order polynomial fit gives good results only for small values of $\eta_{\max}$, the application of a high-order polynomial fit is preferable. This means, in turn, that large values of $\eta_{\max}$ and a considerable number of strain points should be used in order to identify the plateaus.

These results allow one to establish a general criterion for finding the best numerical derivative of a function. In practice, one needs to the identify the flat regions (plateaus), which typically move to higher values of $\eta_{\max}$ when applying a higher-order polynomial fit.

In addition to this analysis, the simple model introduced above can be used to investigate the intrinsic accuracy of the energy values. This can be done with the help of a cross-validation (CV) method [55, 56, 57]. In general, the CV technique allows for optimization of the fitting procedure performed on a sample of statistical data. In practice, we apply the leave-one-out cross-validation score. In our context, it is used as follows.

In our simple examples, the statistical sample consists of N pairs of the type (η_i, E_i). The CV error of a polynomial fit of order n can be calculated as

$$\delta_{\mathrm{CV}}^{(n)} = \sqrt{\frac{1}{N}\sum_{i=1}^{N}\left[E_i - p^{(n)}(\eta_i)\right]^2}\,, \tag{4.7}$$

where $p^{(n)}(\eta_i)$ is the value at η_i of the polynomial function of order n which has been obtained by applying the polynomial fit of order n to $N-1$ points of the sample, *i.e.*, excluding the pair (η_i, E_i).

The CV error defined in Eq. (4.7) as a function of $\eta_{\max}$ for different orders of the polynomial fit is shown in Figure 4.5. The behavior of the different curves

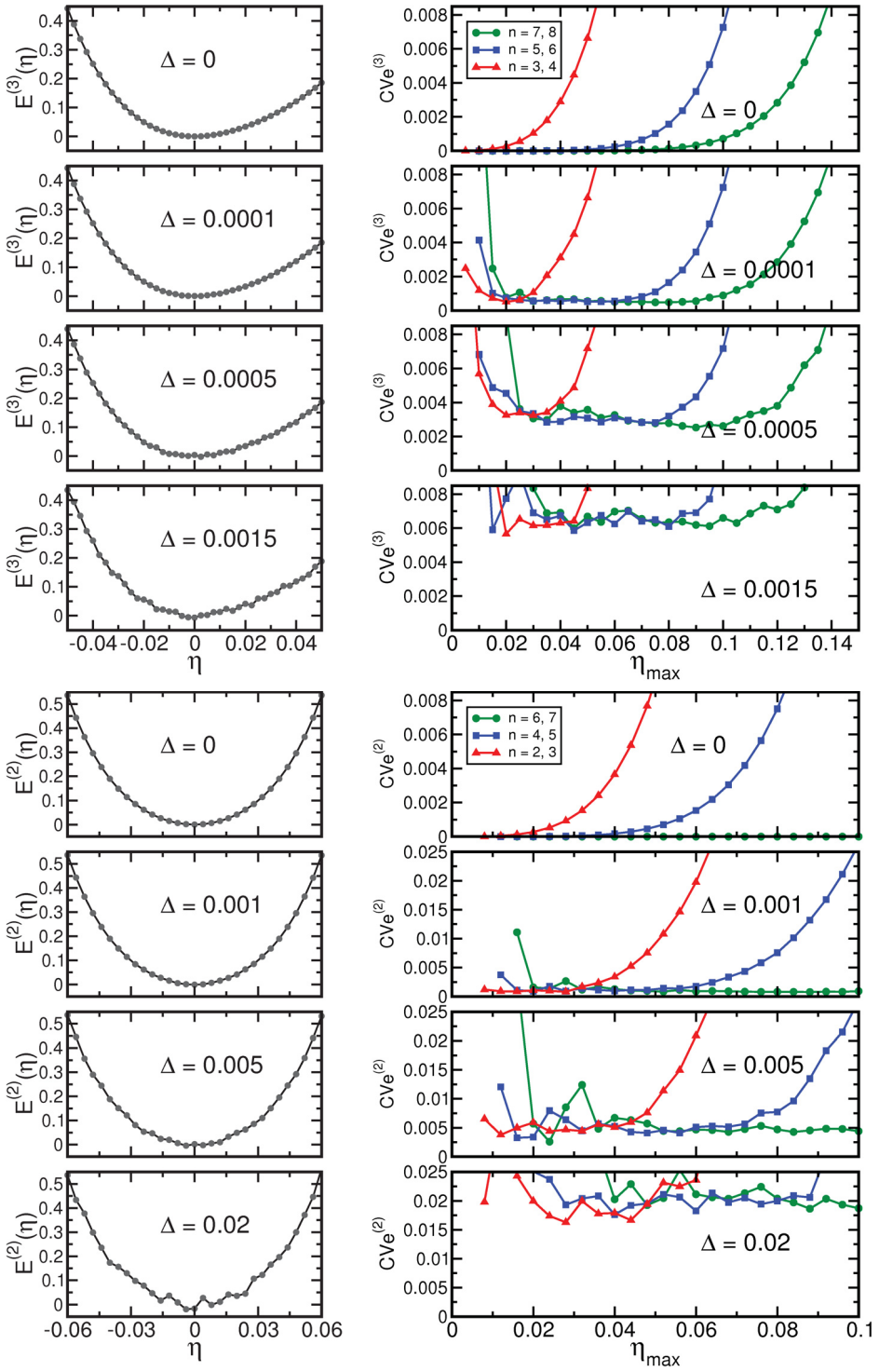

Figure 4.5: The left panels are the same as Figure 4.4. The cross-validation error (CVe) defined in Eq. (4.7) as a function of $\eta_{\max}$ for different values of the maximum noise amplitude for the simple model as discussed in the text. The lower- (upper-)right panels, illustrate the calculated $\mathrm{CVe}^{(2)}$ ($\mathrm{CVe}^{(3)}$) for different amounts of noise.

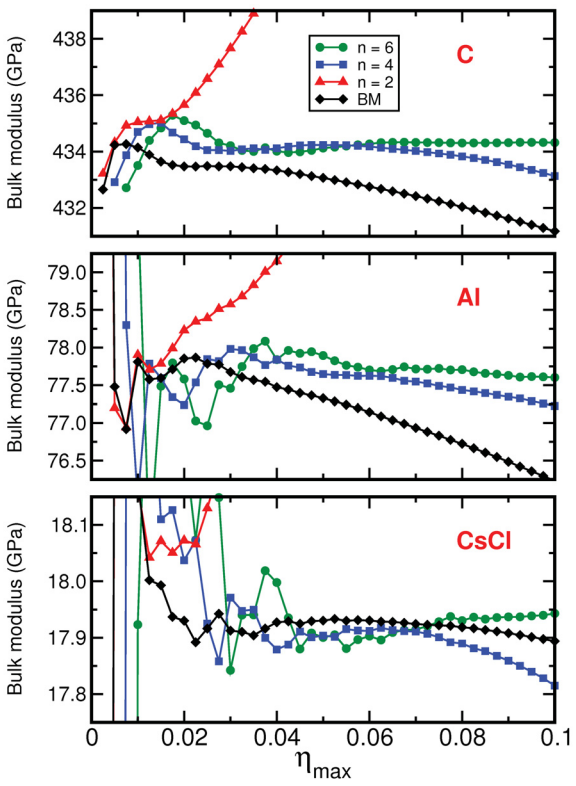

Figure 4.6: Bulk modulus as a function of the maximum absolute value of deformation, $\eta_{\max}$, for three cubic materials: diamond (upper panel), fcc Al (middle panel), and sc CsCl (lower panel). The calculations have been performed using the WIEN2k code.

is similar to the corresponding ones in Figure 4.4. However, in this case, each plateau value gives an estimation of the maximum noise amplitude. Therefore, for real materials, this result can be used to check the numerical accuracy of the energy obtained by the *ab initio* calculation. In fact, if a too large plateau value is found in this case, the accuracy of the DFT computations should probably be increased.

4.2.2 Test Examples for Real Materials

The method illustrated in the previous section can also be applied to real systems, under the assumption that the errors in the calculated DFT energies are statistically independent. In this section, we consider as test cases three materials with cubic structure. These materials are diamond, Al, and CsCl. They are representative systems which can be classified from the elastic point of view as hard, medium, and soft materials, respectively.

The elastic property that we investigate in this test is the bulk modulus. (For cubic systems the different definitions for the bulk modulus give the same value.) In Figure 4.6, we show the result of WIEN2k calculations of the bulk modulus for the test materials as a function of $\eta_{\max}$ and for different orders of the polynomial used in the fitting procedure. As explained in the previous section, only even values of the polynomial order are significant. The deformation type which is used here is a uniform volume change. In addition to the results of the polynomial fit, Figure 4.6 also displays the value of the bulk modulus as obtained using the equation-of-state fitting procedure proposed by Birch and Murnaghan (BM) [58]. The trends observed for the polynomial fits in Figure 4.6 are the same as for the *noisy* curves of the simple model (right panel of Figure 4.4). The converged values of the bulk modulus for the polynomial and the equation-of-state fit, as denoted by the flat part of curves in Figure 4.6, are comparable. Note that the application of the equation-of-state fit is possible for deformations which change only the volume of a system. Therefore, this kind of fit can only be used to obtain a restricted number of elastic properties, *i.e.*, the bulk modulus or its pressure derivative. We have, therefore, implemented the more general approach, *i.e.*, the polynomial-fit procedure in the `ElaStic` code. The choice of the optimal fitting parameters depends on both the material and the applied deformation type. In most cases, for the elastic-constant calculations of the prototype materials reported in Section 4.5, results have been obtained using a sixth-order and seventh-order polynomial fit with values of $\eta_{\max}$ in the range $\eta_{\max} \in [0.05, 0.08]$ and $\eta_{\max} \in [0.05, 0.10]$ for SOECs and TOECs, respectively.

4.3 Choice of Deformation

The type of deformation plays an important role for the accuracy of elastic-constant calculations. The deformation types being used in the `ElaStic` code are presented in Tables 4.3, 4.4 and Table 4.5. Different criteria are applied depending on the used approach.

In the stress approach, the deformation types are defined according to Ref. [31]. These deformations correspond to the so-called universal linear-independent coupling strains [31]. The corresponding deformed structures exhibit very low symmetry, consequently, in a small number of deformation types is required.

A different criterion is followed in the case of the energy approach. We have chosen the set of deformation types where the symmetry of the unperturbed system is least reduced by applying strain. This is done for two reasons: The first is to minimize the computational effort as DFT codes can make use of symmetry. Second, low symmetry may also lead to very slow convergence with respect to computational parameters as has been reported in the literature [59].

The choice of too large values for $\eta_{\max}$ should be avoided due to the possible

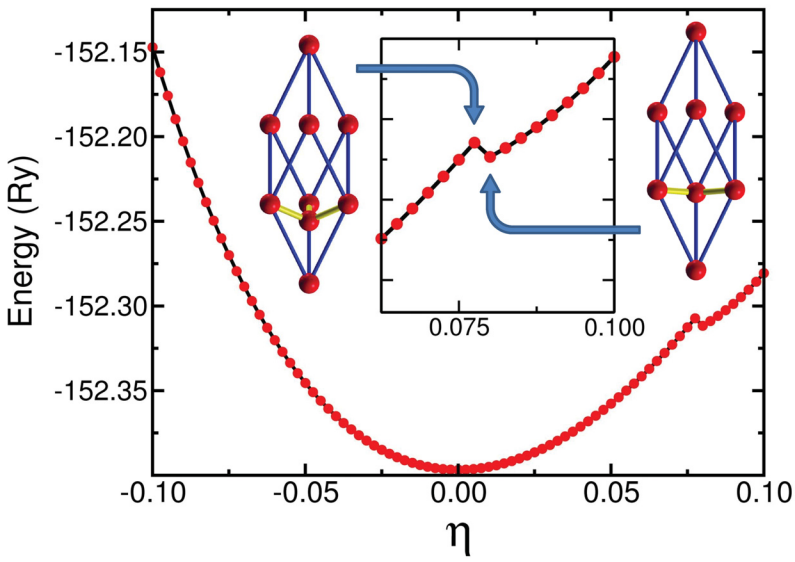

Figure 4.7: Total energy of the deformed diamond structure by applying the $\boldsymbol{\eta}^{(23)}$ deformation type. At $\eta = 0.08$, the kink indicates the transition to a different rhombohedral structure.

onset of a phase transition. For instance, this happens in the calculation of c_{44} for cubic diamond when applying the $\boldsymbol{\eta}^{(23)}$ deformation type. The total energy as a function of the strain for this case is shown in Figure 4.7. The curve exhibits a kink at $\eta = 0.08$ related to the onset of a phase transition from the (deformed) diamond structure to a lamellar rhombohedral system where the carbon sheets are oriented orthogonally to the (1,1,1) direction of the cubic diamond structure.

4.4 Computational Details

The energies and stresses of the distorted structures are calculated using the DFT codes **`exciting`**, WIEN2k, and Quantum ESPRESSO. In all these codes, the electronic states and density are obtained by solving the self-consistent Kohn-Sham equations of DFT [2]. However, they differ in the choice of the basis set which is used to represent electronic states. While **`exciting`** and WIEN2k are based on the full-potential (linearized) augmented plane-wave and local-orbitals (FP-(L)APW+lo) method, the Quantum ESPRESSO software package uses a plane-wave basis set and pseudo-potential approximation. In the most recent implementations, the direct calculation of the stress tensor is available only for the Quantum ESPRESSO package; therefore our results for the stress approach have been obtained by using this code.

First-principles calculations have been performed for a set of materials. At

least one representative crystal for each crystal system has been chosen. Extensive tests for each considered crystal have been carried out to ensure that the calculated properties are converged within a certain accuracy, with respect to all computational parameters, *e.g.*, the **k**-point mesh, the basis set size, and the expansion of the charge density. The main computational parameters which have been used to perform the calculations presented in this work are shown in Tables 4.6 (for **exciting** and WIEN2k) and 4.7 (for Quantum ESPRESSO).

In all calculations, exchange-correlation effects have been treated within the generalized-gradient approximation (GGA) with the PBE [47] functional. The accuracy of the PBE functional in providing results for the elastic constants has been already shown in the literature [21, 22, 23, 24, 25, 26, 27]. Exceptionally, for the calculation of CsCl we have used the PBEsol [48] exchange-correlation functional which allows for a better description of the interatomic bonding, in particular for systems which are characterized by small SOECs value, such as CsCl. In fact, the agreement with experimental data for the elastic constants is improved from about 21% deviation to less than 2% using the PBEsol instead of the PBE functional.

For the integration over the Brillouin zone, we have employed the improved tetrahedron method [60] as well as summations over special points within the Monkhorst-Pack scheme [61]. For metallic systems, the Gaussian-smearing technique [62] has been used. For lattice relaxations, residual forces and stresses have been converged to yield an accuracy better than 0.1 mRy/bohr and 50 MPa, respectively.

4.5 Results

In this section, we present the results for the SOECs and TOECs obtained by the **ElaStic** code. Our main goal is to show the reliability of results and used procedures. We do not particularly aim at matching experimental values, which could be obtained under conditions which are different from the ones considered for the calculations. For instance, theoretical data obtained using DFT should be interpreted only as $T = 0$ K values, while most experiments are performed at room temperature.

Table 4.8: Optimized lattice parameters (a, b, and c, in atomic units) and angles (α, β, and γ, in degrees) for representative materials. $\mathcal{X}$, $\mathcal{W}$, and $\mathcal{Q}$ denote calculations performed with the codes `exciting`, WIEN2k, and Quantum ESPRESSO, respectively. For elemental Ti, the labels (us) and (paw) indicate the use of ultra-soft pseudo-potentials and the Projector-Augmented-Wave method, respectively. The quoted references refer to experimental values.

Laue Group	Material	Code	a	b	c	α	β	γ
C_I	C	$\mathcal{X}$	6.747					
		$\mathcal{W}$	6.749					
		$\mathcal{Q}$	6.741					
		[63]	6.741					
	Al	$\mathcal{W}$	7.636					
		$\mathcal{Q}$	7.669					
		[64]	7.653					
	CsCl	$\mathcal{W}$	7.702					
		[65]	7.797					
H_I	Mg	$\mathcal{Q}$	6.055		9.824			
		[66]	6.053		9.825			
	Ti	$\mathcal{W}$	5.552		8.803			
		$\mathcal{Q}^{(\text{paw})}$	5.555		8.791			
		$\mathcal{Q}^{(\text{us})}$	5.412		8.554			
		[67]	5.575		8.844			
	TiB_2	$\mathcal{W}$	5.729		6.107			
		$\mathcal{Q}$	5.727		6.079			
		[68]	5.726		6.108			
R_I	Al_2O_3	$\mathcal{W}$	9.800			55.28		
		$\mathcal{Q}$	9.741			55.29		
		[69]	9.691			55.28		
R_{II}	$CaMg(CO_3)_2$	$\mathcal{Q}$	11.439			47.24		
		[70]	11.363			47.12		
T_I	MgF_2	$\mathcal{W}$	8.898		5.857			
		$\mathcal{Q}$	8.873		5.855			
		[71]	8.721		5.750			
T_{II}	$CaMoO_4$	$\mathcal{W}$	10.003		21.931			
		$\mathcal{Q}$	10.061		21.881			
		[72]	9.868		21.590			

Continued on next page

Table 4.8 – continued from previous page

Laue Group	Material	Code	a	b	c	α	β	γ
O	$TiSi_2$	$\mathcal{W}$	9.072	15.654	16.200			
		$\mathcal{Q}$	9.048	15.624	16.204			
		[73]	9.071	15.628	16.157			
M	ZrO_2	$\mathcal{W}$	10.128	9.812	9.931			99.63
		$\mathcal{Q}$	10.138	9.786	9.897			99.62
		[74]	10.048	9.733	9.849			99.23
N	$TiSi_2$	$\mathcal{W}$	9.284	9.047	11.264	53.04	51.14	75.82

For the *ab initio* calculation of the elastic constants, first one has to optimize lattice parameters and ionic positions. This optimization has been performed for all the crystal systems we have studied. The results for the equilibrium lattice parameters of the different materials are shown in Table 5.1 for all the used codes. The errors concerning the numerical differentiation have been minimized by using the procedure shown in Section 4.2. Obviously, the different codes (**exciting**, WIEN2k, and Quantum ESPRESSO) and different approaches (energy and stress) should achieve very similar results. If this is not the case, the failure should be attributed to the one or the other approximation which is implicit in the theoretical methods or in their implementation.

Below, results for the different structure families are discussed separately.

4.5.1 Cubic Family

SOECs

For cubic crystals structures, the second-order elastic tensor is fully determined by three independent elastic constants. We have chosen three examples representing different ranges of elastic moduli: diamond, Al, and CsCl, which are known as hard, medium, and soft material, respectively. Hard materials, like diamond, are characterized by very deep energy-strain and very steep stress-strain curves. This situation corresponds to relatively large SOEC values. On the other hand, in soft materials like CsCl, the curves representing the energy/stress as a function of the strain are much flatter, which can cause larger errors in the resulting elastic properties. In fact, while a given accuracy in the evaluation of the total energy may lead to small errors for hard materials, the same accuracy may yield large errors for a soft material.

In Tables 4.9 and 4.10, the SOECs obtained with different approaches and codes are shown. As can be seen in Table 4.9, all the theoretical results for diamond are very similar and very close to the experimental values. The largest

deviation is found for the values of c_{11} and c_{44} which appear smaller than experimental data. The tendency of GGA to slightly overestimate the bonding strength corresponds to an underestimation of the crystal's stiffness. For Al and CsCl, the agreement of all the values with their experimental counterparts (see Table 4.10) is also very good.

TOECs

There are two different classes C_I and C_{II} for cubic crystals, those with point groups 432, $\overline{4}3m$ and $\frac{4}{m}\overline{3}\frac{2}{m}$ are labeled C_I and the cubic crystals with point groups 23 and $\frac{2}{m}\overline{3}$ are specified as C_{II}. The third-order elastic tensor is fully determined by six and eight independent elastic constants for C_I and C_{II}, respectively.

The space group of diamond structure is Fd$\overline{3}$m. It belongs to point group $\frac{4}{m}\overline{3}\frac{2}{m}$ and C_I Laue class. We have calculated the TOECs of C using different codes. Six third-order independent elastic constants are listed in Table (4.11). The results obtained with different codes are in good agreement with each other.

4.5.2 Hexagonal Family

Two different crystal systems belong to the hexagonal family: the primitive hexagonal and the trigonal systems (see Table A.1). In the following, the two systems will be discussed in separate sections.

SOECs

For primitive hexagonal structures, there are five independent second-order elastic constants. As representative for this crystal system, the elemental metal Ti and the metal-like ceramic TiB_2 have been chosen. According to the results presented in Tables 4.12 and 4.13, elastic constants for TiB_2 obtained with different methods and codes are very similar, while for Ti, large deviations are observed among theoretical results obtained with different pseudo-potentials. SOECs calculated using the PAW method [77], are very close to the ones obtained by the WIEN2k code. In both methods, *e.i.*, PAW and all-electron, electrons have been treated in the same way. We have considered the first and second shells, *e.i.*, $1s^2$ $2s^2$ $2p^6$ and the third and fourth shells, *e.i.*, $3s^2$ $3p^6$ $4s^4$ $3d^2$ in the Ti atoms as core and valance electrons, respectively. In contrast, the results based on ultrasoft (us) potentials [78] are significantly different. These deviations indicate a failure of this kind of pseudo-potential approximation for describing the metallic interaction in hexagonal titanium.

In Tables 4.14 and 4.15, we list the calculated SOECs for materials belonging to the trigonal family. In trigonal lattices, there are either six or seven independent elastic constants, and the two cases are distinguishable on the basis of the SGN. We have chosen Al_2O_3 and $CaMg(CO_3)_2$ as examples for the Laue groups R_I and R_{II}, respectively. The calculation of the SOECs for trigonal crystals deserves special attention. First, there is an intrinsic difference between trigonal crystal structures of type P and R (see Table A.1). In contrast to the trigonal R structures, the trigonal P structures are treated on the same footing as the primitive hexagonal ones. Second, the default choice of the reference Cartesian coordinate frame used for these crystals is not the same for all DFT codes. As a consequence, for the trigonal family, the calculated second-order elastic matrix can be different as well, as demonstrated below. The different choices of the default Cartesian reference frame used in **ElaStic** for the DFT codes considered in this thesis are presented in the Table A.2.

According to the literature concerning the SOECs in trigonal R materials, the sign of c_{14} and c_{15} is an open issue. Different signs of c_{14} of Al_2O_3 are found in experimental [81, 82, 83, 84] as well as theoretical work [85, 86, 87, 88]. These discrepancies may be related to the ambiguity in the choice of the Cartesian coordinate frame for the trigonal R structure. In the literature, this structure is referred to as *rhombohedral*, and this denomination will be adopted in the following. Systems with rhombohedral symmetry can be described using a supercell with hexagonal symmetry. The setting of the hexagonal primitive cell with respect to the rhombohedral unit cell is not unique, allowing for different choices of the Cartesian reference frame. An additional complication appears, as in different DFT codes the Cartesian frames are defined differently (see Table A.2). In order to sketch the situation, we show in Figure 4.8 two different choices for the hexagonal and rhombohedral cells of Al_2O_3 together with the rhombohedral primitive vectors projected onto the xy plane. As shown in Figure 4.8, there are two different Cartesian coordinate frames which the elastic constants of rhombohedral structures can be referred to. The two frames are labeled by "+" and "−", which correspond to the sign of c_{14} in our calculated examples. As can be seen in Tables 4.14 and 4.15, our calculated values of c_{14} for Al_2O_3 and $CaMg(CO_3)_2$ are negative, which is due to the choice of the "−" Cartesian coordinate system in the **ElaStic** code.

TOECs

The primitive hexagonal crystals are divided into two classes in Laue classification, H_I and H_{II}. The full third-order elastic tensors of H_I and H_{II} are described by ten and twelve elastic constants, respectively. We have calculated the TOECs of single crystal Mg using the Quantum ESPRESSO code. They are presented in Table 4.16.

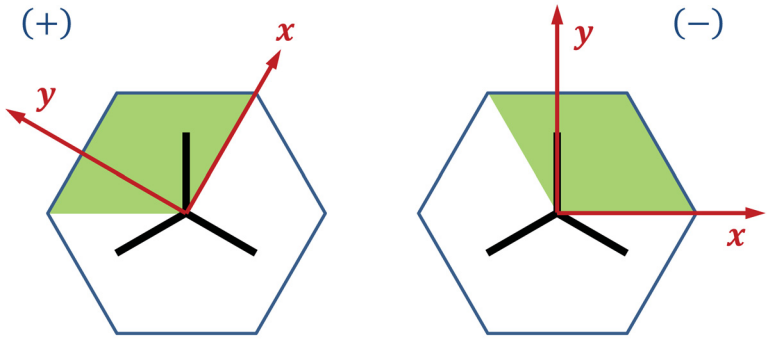

Figure 4.8: Two possible choices for Cartesian coordinates in the trigonal R (rhombohedral) structure. For the coordinate system in the right (left) panel, negative (positive) values are obtained for c_{14} for Al_2O_3. Black bold lines indicate the projection of the primitive rhombohedral lattice vectors onto the xy plane. The shaded (green) areas correspond to the hexagonal primitive cells.

There are 14 and 20 independent third-order elastic constants for the Laue groups R_I and R_{II}, respectively. In Table 4.17, we have presented the TOECs for Al_2O_3 with trigonal structure.

4.5.3 Tetragonal and Orthorhombic Families

Our results for crystals with tetragonal (T_I and T_{II}) as well as orthorhombic symmetry are summarized in Tables 4.18, 4.19, and 4.20, respectively. In the tetragonal systems, there are either six (T_I) or seven (T_{II}) independent elastic constants. We have studied MgF_2 and $CaMoO_4$ as examples for the T_I and T_{II} lattice types, respectively. All calculated results are in reasonable agreement with experimental data. The stress and energy approach, as well as the use of WIEN2k and Quantum ESPRESSO, lead to similar elastic constants, except for c_{12} for $CaMoO_4$ obtained with the WIEN2k code.

The SOECs for the orthorhombic system $TiSi_2$ are listed in Table 4.20. In this case, there are nine independent elastic constants. The comparison between the values obtained by pseudo-potential calculations with the full-potential and experimental results shows large deviations for some elastic constants, *e.g*, c_{13}, c_{22}, c_{33}, and c_{66}. Like before, we assign these discrepancies to the pseudo-potential approximation.

4.5.4 Monoclinic and Triclinic Families

The monoclinic structure is characterized by thirteen independent elastic constants. Due to the large number of SOECs and the low symmetry, calculations

for this structure family are computationally more demanding. We have chosen ZrO_2, zirconia, as representative material.

Theoretical data for monoclinic zirconia are listed in Table 4.21. The choice of Cartesian reference frame for monoclinic structures in the Quantum ESPRESSO and WIEN2k codes is different, as explained in Section A.1. Therefore, in order to compare results of different codes, we have transformed all the elastic constants to the Cartesian coordinate system used in experiment [95] by applying Eq. (B.2). Deviation between theory and experiment may be related to temperature effects.

Triclinic structures exhibit the lowest symmetry, where all the 21 Voigt components of the elastic tensor are independent. Moreover, triclinic materials typically, have more than ten atoms in the unit cell. Hence, in this case the calculations are very demanding. In order to make calculations feasible at reasonable computational cost, we have chosen the primitive orthorhombic cell of $TiSi_2$ as an example, but treated it without considering symmetry. Instead of comparing with the experimental results, we have made a comparison between the elastic constants calculated directly for the triclinic primitive unit cell and those obtained from the transformation of the previous results for the orthorhombic unit cell. The comparison is shown in Table 4.22.

4.6 Summary and Discussion

In this chapter, we have introduced `ElaStic`, a tool for calculating SOECs and TOECs using two alternative approaches that are based on the calculation of the total energy and stress, respectively. The two approaches provide equivalent results, but have some intrinsic differences.

The stress approach allows for relying on a much smaller set of deformations, thus reducing the computational effort. Furthermore, only first and second-order derivatives have to be calculated for SOECs and TOECs, respectively, which improve the accuracy of numerical differentiation. However, the symmetry of the distorted structures in this case is lowered to monoclinic or triclinic, thereby increasing CPU time and memory consumption. In order to achieve the same accuracy by directly computing the stress tensor rather than through total-energy calculations, often computational parameters (*e.g.*, kinetic-energy cutoff, **k**-point sampling, *etc.*) have to be readjusted, which increases the computational costs. In addition, this direct calculation of the stress tensor is not available in every considered code.

On the other hand, a larger number of distortion types must be considered for the energy approach, which also requires the numerical calculation of second-order derivatives for SOEC and third-order derivatives for TOECs. Deformation types, however, can be selected such to preserve the symmetry of the reference system as

much as possible. For more symmetric crystal structures, *e.g.*, cubic or hexagonal, both approaches are equally suitable, but for less symmetric crystal structures like monoclinic or triclinic systems, the stress approach is more efficient.

In order to demonstrate the ability and reliability of **ElaStic**, we have presented SOECs for prototypical example materials of all crystal families and TOECs for some crystal lattices. The results produced with different codes based on total-energy calculations, are in good agreement with each other. Results from the total-energy and the stress approach calculated with Quantum ESPRESSO are also consistent, emphasizing that both procedures are suitable and comparable for the calculations of elastic constants.

At the end of this chapter, we want to emphasize that it is crucial to precisely determine numerical derivatives of the energy (or stress) of a crystal with respect to the Lagrangian strain in order to obtain reliable results for elastic constants. To this extent, we have developed a numerical method which allows the users to do so in an automatized manner.

ElaStic is freely available and can be downloaded from *http://exciting-code.org/*.

Table 4.3: List of deformation types for different Laue groups which are used in `ElaStic` for the SOEC calculations in the energy approach. The number of deformation types, equal to the number of independent SOECs, is denoted by N_{DT}. Deformation types are labeled according to Table 4.1.

Laue group	N_{DT}	Deformation types
$\mathrm{C_{I,II}}$	3	$\boldsymbol{\eta}^{(1)}$,$\boldsymbol{\eta}^{(8)}$,$\boldsymbol{\eta}^{(23)}$
$\mathrm{H_{I,II}}$	5	$\boldsymbol{\eta}^{(1)}$,$\boldsymbol{\eta}^{(3)}$,$\boldsymbol{\eta}^{(4)}$,$\boldsymbol{\eta}^{(17)}$,$\boldsymbol{\eta}^{(26)}$
$\mathrm{R_I}$	6	$\boldsymbol{\eta}^{(1)}$,$\boldsymbol{\eta}^{(2)}$,$\boldsymbol{\eta}^{(4)}$,$\boldsymbol{\eta}^{(5)}$,$\boldsymbol{\eta}^{(8)}$,$\boldsymbol{\eta}^{(10)}$
$\mathrm{R_{II}}$	7	$\boldsymbol{\eta}^{(1)}$,$\boldsymbol{\eta}^{(2)}$,$\boldsymbol{\eta}^{(4)}$,$\boldsymbol{\eta}^{(5)}$,$\boldsymbol{\eta}^{(8)}$,$\boldsymbol{\eta}^{(10)}$,$\boldsymbol{\eta}^{(11)}$
$\mathrm{T_I}$	6	$\boldsymbol{\eta}^{(1)}$,$\boldsymbol{\eta}^{(4)}$,$\boldsymbol{\eta}^{(5)}$,$\boldsymbol{\eta}^{(7)}$,$\boldsymbol{\eta}^{(26)}$,$\boldsymbol{\eta}^{(27)}$
$\mathrm{T_{II}}$	7	$\boldsymbol{\eta}^{(1)}$,$\boldsymbol{\eta}^{(4)}$,$\boldsymbol{\eta}^{(5)}$,$\boldsymbol{\eta}^{(7)}$,$\boldsymbol{\eta}^{(26)}$,$\boldsymbol{\eta}^{(27)}$,$\boldsymbol{\eta}^{(28)}$
O	9	$\boldsymbol{\eta}^{(1)}$,$\boldsymbol{\eta}^{(3)}$,$\boldsymbol{\eta}^{(4)}$,$\boldsymbol{\eta}^{(5)}$,$\boldsymbol{\eta}^{(6)}$,$\boldsymbol{\eta}^{(7)}$,$\boldsymbol{\eta}^{(25)}$ $\boldsymbol{\eta}^{(26)}$,$\boldsymbol{\eta}^{(27)}$
M	13	$\boldsymbol{\eta}^{(1)}$,$\boldsymbol{\eta}^{(3)}$,$\boldsymbol{\eta}^{(4)}$,$\boldsymbol{\eta}^{(5)}$,$\boldsymbol{\eta}^{(6)}$,$\boldsymbol{\eta}^{(7)}$,$\boldsymbol{\eta}^{(12)}$ $\boldsymbol{\eta}^{(20)}$,$\boldsymbol{\eta}^{(24)}$,$\boldsymbol{\eta}^{(25)}$, $\boldsymbol{\eta}^{(27)}$, $\boldsymbol{\eta}^{(28)}$, $\boldsymbol{\eta}^{(29)}$
N	21	$\boldsymbol{\eta}^{(2)}$,$\boldsymbol{\eta}^{(3)}$,$\boldsymbol{\eta}^{(4)}$,$\boldsymbol{\eta}^{(5)}$,$\boldsymbol{\eta}^{(6)}$,$\boldsymbol{\eta}^{(7)}$, $\boldsymbol{\eta}^{(8)}$ $\boldsymbol{\eta}^{(9)}$,$\boldsymbol{\eta}^{(10)}$,$\boldsymbol{\eta}^{(11)}$,$\boldsymbol{\eta}^{(12)}$,$\boldsymbol{\eta}^{(13)}$,$\boldsymbol{\eta}^{(14)}$,$\boldsymbol{\eta}^{(15)}$ $\boldsymbol{\eta}^{(16)}$,$\boldsymbol{\eta}^{(17)}$,$\boldsymbol{\eta}^{(18)}$,$\boldsymbol{\eta}^{(19)}$,$\boldsymbol{\eta}^{(20)}$,$\boldsymbol{\eta}^{(21)}$,$\boldsymbol{\eta}^{(22)}$

Table 4.4: List of deformation types for different Laue groups which are used in `ElaStic` for TOEC calculations in the energy approach. The number of deformation types, equal to the number of independent TOECs, is denoted by N_{DT}. Deformation types are labeled according to Table 4.1.

Laue group	N_{DT}	Deformation types
$\mathrm{C_I}$	6	$\boldsymbol{\eta}^{(1)}$,$\boldsymbol{\eta}^{(8)}$,$\boldsymbol{\eta}^{(10)}$,$\boldsymbol{\eta}^{(11)}$,$\boldsymbol{\eta}^{(23)}$,$\boldsymbol{\eta}^{(32)}$
$\mathrm{C_{II}}$	8	$\boldsymbol{\eta}^{(1)}$,$\boldsymbol{\eta}^{(8)}$,$\boldsymbol{\eta}^{(9)}$,$\boldsymbol{\eta}^{(10)}$,$\boldsymbol{\eta}^{(11)}$,$\boldsymbol{\eta}^{(12)}$,$\boldsymbol{\eta}^{(23)}$,$\boldsymbol{\eta}^{(32)}$
$\mathrm{H_I}$	10	$\boldsymbol{\eta}^{(1)}$,$\boldsymbol{\eta}^{(2)}$,$\boldsymbol{\eta}^{(3)}$,$\boldsymbol{\eta}^{(4)}$,$\boldsymbol{\eta}^{(8)}$,$\boldsymbol{\eta}^{(10)}$,$\boldsymbol{\eta}^{(14)}$,$\boldsymbol{\eta}^{(17)}$ $\boldsymbol{\eta}^{(26)}$,$\boldsymbol{\eta}^{(30)}$
$\mathrm{H_I}$	12	$\boldsymbol{\eta}^{(1)}$,$\boldsymbol{\eta}^{(2)}$,$\boldsymbol{\eta}^{(3)}$,$\boldsymbol{\eta}^{(4)}$,$\boldsymbol{\eta}^{(8)}$,$\boldsymbol{\eta}^{(10)}$,$\boldsymbol{\eta}^{(12)}$,$\boldsymbol{\eta}^{(14)}$ $\boldsymbol{\eta}^{(17)}$,$\boldsymbol{\eta}^{(26)}$,$\boldsymbol{\eta}^{(30)}$,$\boldsymbol{\eta}^{(31)}$
$\mathrm{R_I}$	14	$\boldsymbol{\eta}^{(1)}$,$\boldsymbol{\eta}^{(2)}$,$\boldsymbol{\eta}^{(3)}$,$\boldsymbol{\eta}^{(4)}$,$\boldsymbol{\eta}^{(5)}$,$\boldsymbol{\eta}^{(8)}$,$\boldsymbol{\eta}^{(9)}$,$\boldsymbol{\eta}^{(10)}$ $\boldsymbol{\eta}^{(11)}$,$\boldsymbol{\eta}^{(17)}$,$\boldsymbol{\eta}^{(26)}$,$\boldsymbol{\eta}^{(33)}$,$\boldsymbol{\eta}^{(34)}$,$\boldsymbol{\eta}^{(35)}$

Table 4.5: List of deformation types for different Laue groups which are used in `ElaStic` for the SOEC calculations in the stress approach. The number of deformation types is denoted by N_{DT}. Deformation types are labeled according to Table 4.2.

Laue group	N_{DT}	Deformation types
$\mathrm{C_{I,II}}$	1	$\tilde{\boldsymbol{\eta}}^{(1)}$
$\mathrm{H_{I,II}}$	2	$\tilde{\boldsymbol{\eta}}^{(1)}$, $\tilde{\boldsymbol{\eta}}^{(3)}$
$\mathrm{R_{I,II}}$	2	$\tilde{\boldsymbol{\eta}}^{(1)}$, $\tilde{\boldsymbol{\eta}}^{(3)}$
$\mathrm{T_{I,II}}$	2	$\tilde{\boldsymbol{\eta}}^{(1)}$, $\tilde{\boldsymbol{\eta}}^{(3)}$
O	3	$\tilde{\boldsymbol{\eta}}^{(1)}$, $\tilde{\boldsymbol{\eta}}^{(3)}$, $\tilde{\boldsymbol{\eta}}^{(5)}$
M	5	$\tilde{\boldsymbol{\eta}}^{(1)}$, $\tilde{\boldsymbol{\eta}}^{(2)}$, $\tilde{\boldsymbol{\eta}}^{(3)}$, $\tilde{\boldsymbol{\eta}}^{(4)}$, $\tilde{\boldsymbol{\eta}}^{(5)}$
N	6	$\tilde{\boldsymbol{\eta}}^{(1)}$, $\tilde{\boldsymbol{\eta}}^{(2)}$, $\tilde{\boldsymbol{\eta}}^{(3)}$, $\tilde{\boldsymbol{\eta}}^{(4)}$, $\tilde{\boldsymbol{\eta}}^{(5)}$, $\tilde{\boldsymbol{\eta}}^{(6)}$

Table 4.6: Computational parameters used for lattice optimization and elastic-constant calculations with **exciting** and WIEN2k. Smearing values (σ_{smear}) are given in Ry, muffin-tin radii (R_{MT}) are in atomic units.

Material	Atom	R_{MT}	$R_{\mathrm{MT}}K_{\mathrm{max}}$	**k**-mesh	σ_{smear}
C	C	1.15	8.0	15×15×15	–
Al	Al	2.00	9.0	36×36×36	0.025
CsCl	Cs	2.00	9.0	15×15×15	–
	Cl	2.00			
Ti	Ti	2.00	8.0	16×16×9	0.010
TiB_2	Ti	2.23	9.0	15×15×12	–
	B	1.54			
Al_2O_3	Al	1.64	8.0	8×8×8	–
	O	1.64			
MgF_2	Mg	1.80	8.0	10×10×16	–
	F	1.40			
$CaMoO_4$	Ca	1.60	8.0	8×8×8	0.010
	Mo	1.60			
	O	1.50			
$TiSi_2$	Ti	2.10	8.5	8×8×8	–
	Si	1.50			
ZrO_2	Zr	1.75	8.0	7×8×7	–
	O	1.55			
$TiSi_2$	Ti	2.00	8.5	14×12×14	–
	Si	2.00			

Table 4.7: Computational parameters used for lattice optimization and elastic-constant calculations with the Quantum ESPRESSO code. Kinetic-energy cutoffs (E_{cut}) and smearing values (σ_{smear}) are given in Ry.

Material	$E_{\mathrm{cut}}^{(\mathrm{wfc})}$	$E_{\mathrm{cut}}^{(\mathrm{rho})}$	**k**-mesh	σ_{smear}
C	80	480	15×15×15	–
Al	80	800	36×36×36	0.025
Mg	80	800	26×26×16	0.060
Ti	80	800	16×16× 9	0.010
TiB_2	100	1000	15×15×12	–
Al_2O_3	80	800	8× 8× 8	–
MgF_2	80	800	10×10×16	–
$CaMoO_4$	80	800	8× 8× 8	0.010
$TiSi_2$	80	800	8× 8× 8	0.010
ZrO_2	80	800	7× 8× 7	–

Table 4.9: Elastic constants ($c_{\alpha\beta}$) for single-crystal C with the cubic diamond structure. We also show results for the isotropic bulk (B) and shear (G) modulus for polycrystalline samples obtained using both the Voigt and Reuss averaging procedure. (Note that for cubic structures $B_{\mathrm{V}} = B_{\mathrm{R}} = B$.) The Young's modulus ($E$) and Poisson's ratio ($\nu$) are estimated from Hill's approximation. All data except ν, which is dimensionless, are given in GPa. The symbols $\mathcal{W}$, $\mathcal{X}$, and $\mathcal{Q}$ denote calculations performed with the codes WIEN2k, **exciting**, and Quantum ESPRESSO, respectively. The subscripts $\mathcal{E}$ and $\boldsymbol{\tau}$ indicate the use of the energy and stress approach, respectively. Experimental values for the elastic constants are taken from Ref. [75], the experimental elastic moduli are obtained from these values using Eqs. (2.38), (2.39), (2.40), (2.41), (2.42), and (2.43).

C	$\mathcal{W}_{\mathcal{E}}$	$\mathcal{X}_{\mathcal{E}}$	$\mathcal{Q}_{\mathcal{E}}$	$\mathcal{Q}_{\boldsymbol{\tau}}$	[75]
c_{11}	1052.3	1055.9	1052.7	1053.0	1077.0
c_{12}	125.0	125.1	121.5	121.3	124.6
c_{44}	559.3	560.6	560.3	560.6	577.0
B	434.1	435.4	431.9	431.8	442.1
G_{V}	521.0	522.5	522.4	522.7	536.7
G_{R}	516.7	518.2	518.2	518.4	532.0
E_{H}	1113.1	1116.3	1113.7	1114.0	1142.6
ν_{H}	0.07	0.07	0.07	0.07	0.07

Table 4.10: Same as Table 4.9 for Al (left) and CsCl (right) in the cubic structure. Data from Refs. [75] and [76] are experimental values.

	Al				CsCl	
	$\mathcal{W}_\mathcal{E}$	$\mathcal{Q}_\mathcal{E}$	$\mathcal{Q}_{\boldsymbol{\tau}}$	[75]	$\mathcal{W}_\mathcal{E}$	[76]
c_{11}	112.1	109.3	109.0	108.0	36.9	36.4
c_{12}	60.3	57.5	57.7	62.0	8.4	8.8
c_{44}	32.8	30.1	34.6	28.3	8.4	8.0
B	77.6	74.8	74.8	77.3	17.9	18.0
G_V	30.1	28.4	31.0	26.2	10.8	10.3
G_R	29.7	28.3	30.4	25.9	10.8	9.6
E_H	79.4	75.5	81.1	70.2	26.2	25.2
ν_H	0.33	0.33	0.32	0.35	0.26	0.27

Table 4.11: TOECs (in GPa) for single crystal C in the first class of cubic structures in the Laue classification, calculated using the **exciting**, WIEN2k, and Quantum ESPRESSO codes.

	c_{111}	c_{112}	c_{123}	c_{144}	c_{155}	c_{456}
$\mathcal{X}_\mathcal{E}$	–5790.1	–1664.3	592.5	–207.2	–2778.7	–1150.5
$\mathcal{W}_\mathcal{E}$	–5851.6	–1641.7	601.5	–207.9	–2779.3	–1147.4
$\mathcal{Q}_\mathcal{E}$	–5925.1	–1602.5	626.3	–196.6	–2772.2	–1154.5

Table 4.12: Same as Table 4.9 for TiB_2 in the primitive hexagonal structure. Data from Ref. [79] are the experimental values.

TiB_2	$\mathcal{W}_\mathcal{E}$	$\mathcal{Q}_\mathcal{E}$	$\mathcal{Q}_\boldsymbol{\tau}$	[79]
c_{11}	652	654	652	660
c_{12}	69	71	69	48
c_{13}	103	100	98	93
c_{33}	448	459	463	432
c_{44}	258	260	259	260
B_V	256	256	256	247
B_R	250	251	251	240
G_V	260	262	262	266
G_R	254	257	257	258
E_H	576	581	581	579
ν_H	0.12	0.12	0.12	0.10

Table 4.13: Same as Table 4.9 for Ti in the primitive hexagonal structure. The labels (us) and (paw) indicate the use of ultra-soft pseudo-potentials and the PAW method, respectively. Data from Ref. [80] are experimental values.

Ti	$\mathcal{W}_\mathcal{E}$	$\mathcal{Q}_\mathcal{E}^{(\mathrm{paw})}$	$\mathcal{Q}_\mathcal{E}^{(\mathrm{us})}$	[80]
c_{11}	179	174	190	160
c_{12}	85	85	99	90
c_{13}	74	77	91	66
c_{33}	187	181	213	181
c_{44}	44	44	39	46
B_V	112	112	128	105
B_R	112	112	128	105
G_V	48	46	45	44
G_R	48	46	44	42
E_H	125	120	120	114
ν_H	0.31	0.32	0.34	0.32

Table 4.14: Same as Table 4.9 for Al_2O_3 in the trigonal R_I structure. Data from Ref. [80] are the experimental values.

Al_2O_3	$\mathcal{W}_\mathcal{E}$	$\mathcal{Q}_\mathcal{E}$	$\mathcal{Q}_\tau$	[80]
c_{11}	453.4	463.8	460.9	497.4
c_{12}	151.2	148.5	148.7	164.0
c_{13}	108.0	107.9	107.8	112.2
c_{14}	–20.5	–20.3	–20.4	–23.6
c_{33}	452.0	469.9	466.4	499.1
c_{44}	132.2	139.0	137.6	147.4
B_V	232.6	236.2	235.2	252.3
B_R	232.2	236.0	234.9	251.8
G_V	149.2	156.0	154.5	166.0
G_R	144.7	151.7	150.2	160.6
E_H	364.1	379.3	375.8	403.0
ν_H	0.24	0.23	0.23	0.23

Table 4.15: Same as Table 4.9 for $CaMg(CO_3)_2$ (dolomite) in the trigonal R_{II} structure. Data from Ref. [89] are the experimental values.

$CaMg(CO_3)_2$	$\mathcal{Q}_\mathcal{E}$	$\mathcal{Q}_\tau$	[89]
c_{11}	194.3	194.5	205.0
c_{12}	66.5	66.7	71.0
c_{13}	56.8	56.4	57.4
c_{14}	–17.5	–17.7	–19.5
c_{15}	11.5	11.1	13.7
c_{33}	108.5	107.4	113.0
c_{44}	38.8	38.6	39.8
B_V	95.3	95.0	99.4
B_R	87.2	86.6	90.3
G_V	49.4	49.4	51.8
G_R	39.4	39.3	39.7
E_H	114.7	114.4	118.2
ν_H	0.29	0.29	0.29

Table 4.16: TOECs, given in GPa, for single crystal Mg in the first class of the hexagonal structures in Laue classification, calculated using the Quantum ESPRESSO code. Data from Ref. [90] are the experimental values. They are measured at 300 K.

	c_{111}	c_{112}	c_{113}	c_{123}	c_{133}
	–641	–184	18	–80	–113
[90]	–663	–178	30	–76	–86
	c_{144}	c_{155}	c_{222}	c_{333}	c_{344}
	–47	–75	–780	–696	–170
[90]	–30	–58	–864	–726	–193

Table 4.17: TOECs (in GPa) for single crystal Al_2O_3 in the first class of rhombohedral structure in Laue classification calculated using the Quantum ESPRESSO code. Data from Ref. [91] are experimental values.

	c_{111}	c_{112}	c_{113}	c_{114}	c_{123}	c_{124}	c_{133}
	–3601	–986	–764	283	–146	–57	–910
[91]	–3932	–1120	–922	98	–215	–53	–970
	c_{134}	c_{144}	c_{155}	c_{222}	c_{333}	c_{344}	c_{444}
	–133	–441	–1162	–4204	–2913	–1054	34
[91]	–104	–382	–1076	–4515	–3100	–1137	23

Table 4.18: Same as Table 4.9 for MgF_2 in the tetragonal T_I structure. Data from Ref. [92] are experimental values.

MgF_2	$\mathcal{W}_\mathcal{E}$	$\mathcal{Q}_\mathcal{E}$	$\mathcal{Q}_\tau$	[92]
c_{11}	130.0	127.0	126.5	123.7
c_{12}	78.2	80.1	79.8	73.2
c_{13}	54.7	57.3	57.6	53.6
c_{33}	185.0	187.7	187.3	177.0
c_{44}	50.5	50.8	50.7	55.2
c_{66}	83.0	87.2	87.2	97.8
B_V	91.1	92.3	92.2	87.2
B_R	90.5	91.4	91.3	86.4
G_V	54.0	54.2	54.0	57.9
G_R	46.7	45.2	45.0	48.1
E_H	127.4	126.3	126.0	132.1
ν_H	0.27	0.27	0.27	0.25

Table 4.19: Same as Table 4.9 for $CaMoO_4$ in the tetragonal T_{II} structure. Data from Ref. [93] are experimental values.

$CaMoO_4$	$\mathcal{W}_\mathcal{E}$	$\mathcal{Q}_\mathcal{E}$	$\mathcal{Q}_\tau$	[93]
c_{11}	123.4	126.9	125.9	144.7
c_{12}	43.9	58.0	57.5	66.4
c_{13}	48.7	46.6	46.0	46.6
c_{16}	8.1	10.2	10.1	13.4
c_{33}	109.3	110.0	109.3	126.5
c_{44}	31.5	29.0	28.7	36.9
c_{66}	37.4	34.2	34.2	45.1
B_V	71.0	74.0	73.4	81.7
B_R	70.9	73.2	72.6	80.5
G_V	34.4	32.6	32.4	40.9
G_R	33.5	31.1	30.9	38.7
E_H	87.8	83.5	83.0	102.6
ν_H	0.29	0.31	0.31	0.29

Table 4.20: Same as Table 4.9 for $TiSi_2$ in the orthorhombic structure. Data from Ref. [94] are experimental values. For titanium, an ultra-soft pseudo-potential has been used for calculations performed with Quantum ESPRESSO.

$TiSi_2$	$\mathcal{W}_\mathcal{E}$	$\mathcal{Q}_\mathcal{E}$	$\mathcal{Q}_\boldsymbol{\tau}$	[94]
c_{11}	312.5	297.9	306.4	320.4
c_{12}	27.9	18.5	24.8	29.3
c_{13}	83.8	123.3	112.3	86.0
c_{22}	306.3	212.2	204.6	317.5
c_{23}	21.1	31.2	31.5	38.4
c_{33}	406.4	481.9	495.8	413.2
c_{44}	73.1	73.6	73.2	75.8
c_{55}	106.4	108.7	100.0	112.5
c_{66}	117.3	97.5	106.0	117.5
B_V	143.4	148.7	149.4	150.9
B_R	139.4	124.0	124.1	146.8
G_V	118.8	110.5	111.7	120.9
G_R	110.0	101.2	101.6	112.9
E_H	270.3	252.3	253.9	278.1
ν_H	0.180	0.190	0.190	0.188

Table 4.21: Same as Table 4.9 for ZrO_2 (zirconia) in the monoclinic structure. Data from Ref. [29] are obtained using the CASTEP code and the stress approach whereas data from Ref. [95] are experimental values.

ZrO_2	$\mathcal{W}_{\mathcal{E}}$	$\mathcal{Q}_{\mathcal{E}}$	$\mathcal{Q}_{\boldsymbol{\tau}}$	[29]	[95]
c_{11}	356	334	333	341	361
c_{12}	161	151	157	158	142
c_{13}	76	82	85	88	55
c_{15}	32	32	28	29	–21
c_{22}	361	356	363	349	408
c_{23}	120	142	154	156	196
c_{25}	–3	–2	–6	–4	31
c_{33}	217	251	258	274	258
c_{35}	2	7	3	2	–18
c_{44}	80	81	80	80	100
c_{46}	–16	–15	–15	–14	–23
c_{55}	69	71	71	73	81
c_{66}	113	115	115	116	126
B_{V}	183	188	194	196	201
B_{R}	163	174	181	187	175
G_{V}	91	91	90	91	91
G_{R}	83	84	83	84	84
E_{H}	223	226	225	229	226
ν_{H}	0.28	0.29	0.30	0.30	0.29

Table 4.22: Elastic constants (in GPa) for single crystal $TiSi_2$, treated in the primitive unit cell as triclinic structure and calculated using the WIEN2k code. First row values are the results obtained by direct calculations in the triclinic unit cell, second row values are obtained by transforming the results from the centrosymmetric orthorhombic unit cell (lattice class O) to the triclinic structure (N) using Eq. (B.2).

	c_{11}	c_{12}	c_{13}	c_{14}	c_{15}	c_{16}	c_{22}	c_{23}	c_{24}
Direct calculations	354.5	42.2	88.6	–31.4	27.4	–14.4	284.1	48.9	17.2
Transform from O to N	361.1	39.8	89.6	–33.8	30.4	–15.3	285.0	48.8	15.4
	c_{25}	c_{26}	c_{33}	c_{34}	c_{35}	c_{36}	c_{44}	c_{45}	c_{46}
Direct calculations	7.5	14.8	287.3	–17.0	–4.6	–14.0	128.9	–4.0	–8.8
Transform from O to N	5.9	14.0	288.4	–17.7	–3.1	–15.4	129.3	–8.2	–8.3
	c_{55}	c_{56}	c_{66}	B_{V}	B_{R}	G_{V}	G_{R}	E_{H}	ν_{H}
Direct calculations	119.3	–17.5	92.6	142.8	139.3	117.9	109.6	269.0	0.18
Transform from O to N	120.0	–18.4	92.9	143.4	139.4	118.8	110.0	279.4	0.18

5 NiTi- A Shape-Memory Material

In 1890s, Adolf Martens discovered by rapidly cooling down (quenching) carbon steel in the austenite phase, it turned into a new phase that was named the Martensite phase after him. After its discovery, many efforts were made in order to understand the dynamics of this transformation until 1949, when the irreversible martensite transformation was eventually explained thanks to experiments made on CuZn and CuAl martensitic alloys [96]. In 1950s, the thermoelastic martensitic transformation and shape-recovery behavior were demonstrated for alloys such as InTl and CuZn [97, 98]. The discovery of NiTiNOL[1] materials, in 1963, attracted research interest because of the new properties in shape-memory alloys (SMAs). These researches led to more profound understanding of the impacts of composition, microstructure, and heat treatment of SMAs on their properties. Later, it was found that adding a third alloying element such as Co or Fe to the existing NiTi system causes a dramatic decrease in the SMA transformation temperature, thus opening new opportunities for their applications in industries, such as aerospace, automotive, biomedical, and medical.

SMAs are divided into three subgroups: Cu-Zn-Al-Ni, Cu-Al-Ni, and NiTi alloys [99], they exhibit the general practical properties such as shape-memory effect and superelasticity. NiTi alloys have many unique characteristics, such as high ductility and low elastic anisotropy which make them very interesting. In particular, the elastic anisotropy, which is defined as $A = 2c_{44}/(c_{11} - c_{12})$, is $\sim$ 2 whereas in most other SMAs the value of this quantity is $\geq$10. c_{44} decreases when temperature decreases, which is just the opposite behavior of most other shape-memory and normal alloys. Moreover, the reversible martensitic transformation of NiTi takes place near room temperature, while it usually happens at high temperature for other SMAs. Besides, the monoclinic structure appears only in the NiTi alloys, and rhombohedral structure has similarity only with the martensite phase in the AuCd alloys.

[1]The term "NiTiNOL"was created for the NiTi materials in honor of its discovery at the Naval Ordnance Laboratory (NOL).

Due to the complexity of the transformation and sensitivity of some factors like alloying with different elements and thermomechanical treatment, NiTi system is less understood than other alloys.

One way to get a clearer picture of the transition at the atomic level and to understand structural features, phase stability, and possible transition paths is the *ab initio* investigation of these systems. Traditionally, in computational physics, the description of a phase transition is feasible with thermodynamic approaches such as calculating the free-energies of different phases [100, 101, 102]. Unfortunately, these approaches were not able to explain the whole transformation picture. The important examples are the effect of composition, alloying and point defects, which can modify strongly both transformation temperature and transformation path. Moreover, these approaches cannot treat high-temperature effects on every crystal system. Recently, it has been shown that the high-temperature phase of NiTi alloy is stable due to anharmonic effects [103]. Souvatzis *et al.* [103] have taken anharmonicity into account by a self- consistent *ab initio* lattice dynamical method. Unfortunately, this approach is computationally very expensive for alloys with low impurity concentrations. On the other hand, it is known that the martensitic transformation occurs by lattice distortion, so it is important to obtain lattice dynamic properties rather than thermodynamical properties. The investigation of elastic-constants is a tractable way to obtain some insight into lattice-dynamical properties. Due to the difficulty of growing NiTi single crystals in different phases, there have been only a few experimental data for NiTi phases in the past decades. This makes the investigation of the elastic constants of ordered crystals of NiTi with *ab initio* methods highly desirable. Two studies of the elastic properties of NiTi were recently published by Wagner and Windl [104] and Hatcher [105] in which the elastic constants of different phases using the pseudo-potential and FLAPW methods were calculated, respectively. Possible shortcomings of these works are the lack of lattice relaxation in Ref. [105] and the usage of the pseudo-potential approximation in Ref. [104], as been seen in Section 4.5 is problematic for Ti compounds. Then, further investigation and more precise calculations are required.

In this chapter, we aim at investigating the martensitic transformation in the NiTi system by means of the DFT calculations. We point out again that we compute ordered NiTi phases. Nevertheless, at the atomic as discussed in Section 2.5, averaging methods are applied to our results to approach polycrystalline and alloy materials.

The outline of the chapter is as follows: In the Section 5.1, we give a general description of the phase transitions in SMAs. Section 5.2 is dedicated to the NiTi crystal structures. At the end, in the Section 5.3, we present and discuss the *ab initio* results.

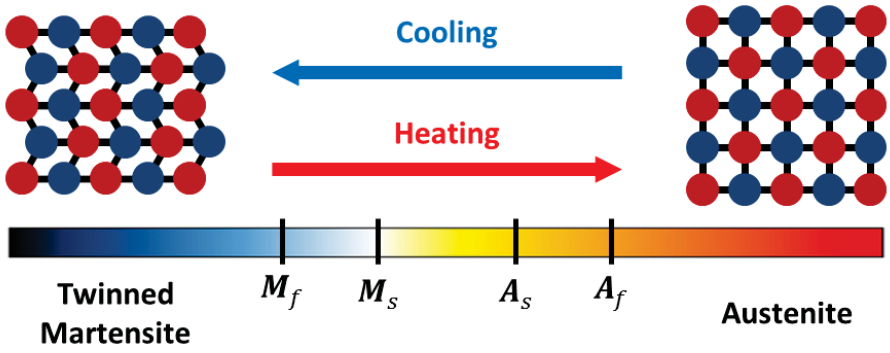

Figure 5.1: Schematic representation of the shape deformations in SMAs in absence of stress, from austenite to twinned martensite and vice versa. The temperatures M_s, M_f, A_s, and A_f temperatures are explained in the text. The illustration is based on Ref. [106].

5.1 Phase Transitions in SMAs

In SMAs, there are usually two phases, with different crystal structures and different properties. One is the high-temperature phase (or parent phase), *austenite* (A), and the other is the low-temperature phase, *martensite* (M). The austenite crystal structure is cubic, while martensite can be tetragonal, orthorhombic or monoclinic. The transformation from one structure to the other does not occur by diffusion of atoms, but rather by shear lattice deformation. This type of transformation is known as *martensitic* transformation. Martensitic phase is formed by different orientated crystal grains, called *variant*. There are two forms of martensitic phases: twinned martensite, which is formed by a combination of different martensitic variants, and detwinned or reoriented martensite, which is deformed by a specific dominant variant.

The reversible phase transformation from austenite to martensite is a unique feature of SMAs. When temperature is decreased in absence stress, the crystal structure changes from austenite to martensite. This fact is shown schematically in Figure 5.1. The phase transition from austenite to martensite is called the *forward* transformation. The transformation yields several martensitic variants which are randomly oriented. For example, there are 24 different orientations for NiTi alloys. Their orientations are such that the average macroscopic shape does not change. As can be seen in Figure 5.1, when the material in the martensitic phase is heated, the crystal structure transforms back to austenite: this transformation is called *reverse* transformation, which is not associated to any shape changes.

There are four characteristic temperatures associated with the martensitic phase transformation. In case of zero stress, during the forward transformation, austenite begins to transform to martensite at the *martensitic start temperature*

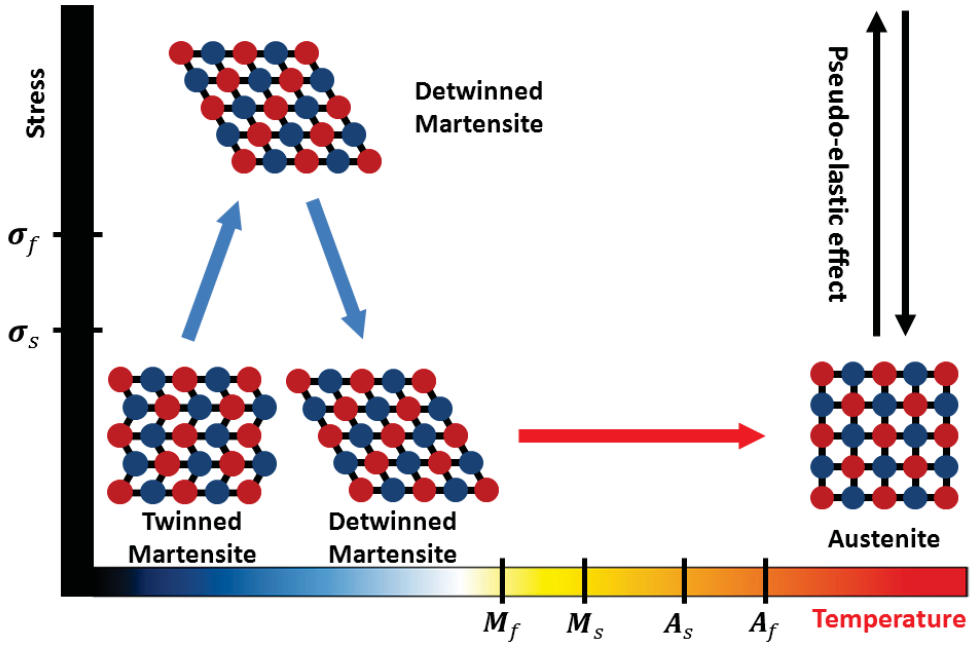

Figure 5.2: Schematic picture of the shape-memory and pseudo-elastic effects of a SMAs. Showing the detwinning of SMA under an applied stress and the release of the stress and subsequent heating to austenite under no stress condition. The illustration is based on Ref. [106].

(M_s). The transformation to martensite will be completed at the *martensitic finish temperature* (M_f) when the material has fully turned into the twinned martensitic phase. In a similar way, when the material is heated the reverse transformation initiates at the *austenitic start temperature* (A_s) and the transformation will be completed at the *austenitic finish temperature* (A_f).

Suppose an external stress is applied to the martensitic phase. In this situation, it is possible to transform the martensite crystals to the austenite phase within two steps. As a first step, a certain number of crystal grains is reoriented, as schematically shown in Figure 5.2. Then, when the stress is released, the deformed configuration will turn back into its original shape and this process results in a change of the macroscopic shape of material. This process is referred to as the *shape-memory effect* (SME). The complete procedure is shown schematically in Figure 5.2. The applied stress must be large enough to start the SME process. The minimum amount of stress which is required for the detwinning procedure to start is called the *detwinning start* stress (σ_s), and the maximum level of stress that results in a complete detwinning of the materials is called the *detwinning finish* stress (σ_f).

The transformation is also possible by applying a very high mechanical stress to the austenite phase. As schematically shown in Figure 5.2, when the temperature is above A_f, a complete shape recovery is observed and the whole material

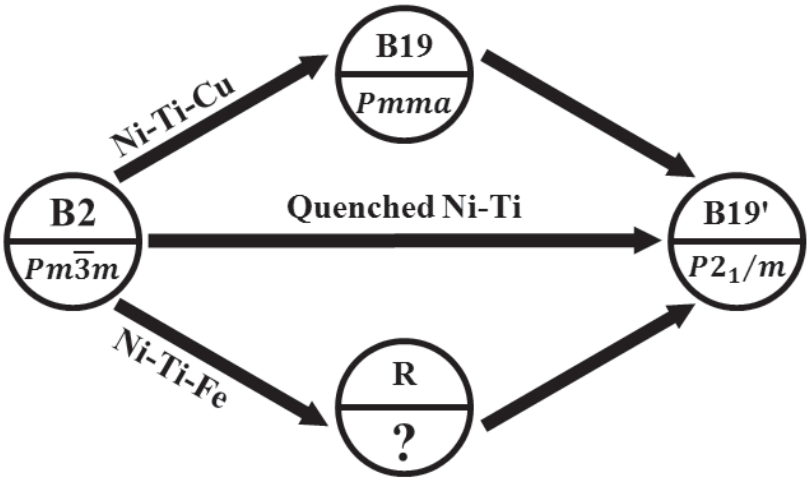

Figure 5.3: Three transformation paths for NiTi alloys from the B2 parent phase to the B19′ martensitic phase. The crystal symmetry of R phase is discussed in Section 5.3.2. The illustration is based on Ref. [107]

transforms to the austenite phase. This behavior of SMA materials is called the *pseudo-elastic* effect. If the material in the austenitic phase is tested at a temperature between M_s and A_f, only partial shape recovery will have happened.

Readers may refer to Refs. [99, 106] for a more detailed description of the phase transitions in SMAs.

The phase transitions in NiTi alloys can be classified by three types of transformations, as shown schematically in Figure 5.3. All transformation paths have a tendency to transform from the B2 parent phase to the B19′ martensitic phase. The next section is dedicated to different ordered crystals of NiTi phases.

5.2 Ordered Crystal Phases of NiTi

In order to understand the martensitic transformation in the NiTi alloy system, it is essential to know first the crystal structure of the different phases. In total, there are three different phases that are observed throughout the martensitic transformation of NiTi:

i) *High-temperature phase*
The parent austenitic phase of NiTi is the B2 [2] structure, which is the CsCl-type structure with space group $Pm\bar{3}m$. This phase was identified early

[2]Here, we use *Strukturbericht* classification which is an usual representation for alloys. It shows the ordered polyatomic crystal structures. For instance, B stands for a compounds with two different types of atom in a crystal. B2, B19′, and B19 symbols represent the cubic, monoclinic, and orthorhombic crystal structures, respectively.

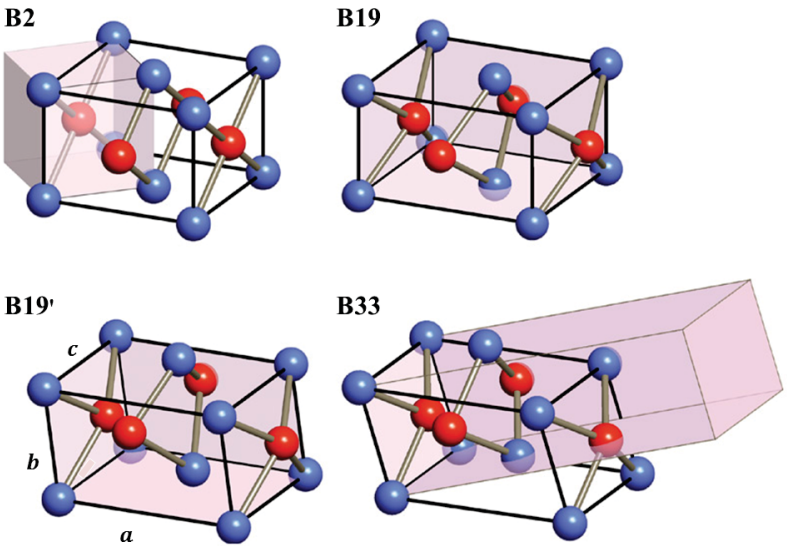

Figure 5.4: Crystal structures relevant for the martensitic transformation in NiTi: B2, B19, B19′, and B33. The relation between the B2 structure, shadowed box, and the $B2_T$ structure is shown in the upper-left picture. The lower-right picture presents the body-centered orthorhombic B33 structure, shadowed box, with space group *Cmcm*. Ti and Ni atoms are indicated by blue and red spheres, respectively. In order to facilitate the comparison between the structures, for all case, the origin has been shifted to a Ti atom. The pictures are based on Ref. [108].

[109, 110] and is now well established as the high-temperature austenite structure [111]. This structure can also be represented by a larger tetragonal four-atom unit cell, as can be seen in Figure 5.4. We use the symbol $B2_T$ for this structure.

ii) *Intermediate phase*
The "R phase" is one of the intermediate phases which can be observed experimentally [112] during the martensitic transformation. The term "R phase" arises from *rhombohedral* distortion, because it has been assumed that the B2 structure propagates to the B19′ structure by rhombohedral distortion [99]. However, later it was established that the structure has trigonal symmetry rather than a rhombohedral one. In general, there are three cases where the transformation goes through R phase: First, a small percentage of Ni is substituted by Fe or Al; Second, for the Ni-rich NiTi alloys such as the Ti_3Ni_4 phase; Third, upon heat-treatment of the NiTi alloys after cold-working to create rearranged dislocation structures. The space group of this structure remains ambiguous despite different measurements and calculations. It has been initially determined as $P\bar{3}1m$ (No. 164) using convergent-beam electron diffraction and transmission electron microscopy with iron alloyed ($Ti_{50}Ni_{47}Fe_3$) samples [113]. Hara's [114] refinement by electron and

powder X-ray diffraction measurements indicated that the Ti and Ni atoms are located in much less symmetric positions rather than atomic positions of the space group $P\bar{3}1m$. This resulted in the suggestion of a different space group with a lower symmetry, namely $P3$ (No. 143). Schryvers *et al.* [115] followed these measurements using high-precision dynamic electron diffraction and least-square minimization analysis with the same samples. They found a more symmetric structure with space group $P\bar{3}$ (No. 147). Gong *et al.* [116] investigated several different initial configurations taken from experiment to calculate optimized lattice constants and atomic positions for equiatomic NiTi. They suggested that the $P31m$ (No. 157) structure is the correct crystalline ground state of the R phase. Nevertheless, the exact space group and the atomic positions of Ni and Ti are not still completely clear. Therefore, in total, there are four suggested space groups for this structure, namely $P3$, $P\bar{3}$, $P31m$, and $P\bar{3}1m$. This point will be discussed in Section 5.3.2.

The second intermediate phase is B19 which has an orthorhombic crystal structure with space group $Pmma$. It is shown in the upper-right panel of Figure 5.4. This phase is observed when NiTi is alloyed with at least 7.5% of Cu or when certain percentages of other elements, such as Pd and Pt, substitute Ni atoms. The B19 phase becomes the martensitic phase also when NiTi is alloyed with at least 20% copper.

iii) *Low-temperature phase*
The crystal structure of the low-temperature phase of NiTi has been an unsolved problem for many years. It took a while to make clear that the space group of this structure is $P2_1/m$ which is called B19′, shown in the lower-left picture of Figure 5.4. The monoclinic structure B19′ [3] has been generally confirmed by experimentalists and theoreticians [109, 110, 117, 118, 119] as the low-temperature phase of NiTi.

Furthermore, Huang [108] showed with first-principles calculations that a base-centered orthorhombic (BCO) structure of space group $Cmcm$ can be a martensitic phase of NiTi and claimed that the experimentally reported B19′ structure is stabilized by internal stresses. This structure can be regarded as a special case of the B19′ structure with the atomic positions obeying certain relations. This crystal structure is best known as B33. In Figure 5.4, the relation between the BCO and the B33 structure is shown.

[3] There are two different choices of axes in a monoclinic crystal system. In the first setting, the unique axis is parallel to c and the monoclinic angle is γ. In the second one, the unique axis is parallel to b and β is the monoclinic angle. In this thesis, we use the first setting to represent the B19′ structure.

5.3 Results

In this section, we investigate elastic constants of different ordered crystal phases of NiTi. All the elastic-constant calculations were performed with the `ElaStic` tool and the WIEN2k code. As discussed in Chapter 4, elastic-constant calculations require the structure to be optimized with respect to the unit cell and all internal degrees of freedom. Thus, first, we present computational details and results of structural optimization. Then, the results which were used for the elastic constants will be given.

5.3.1 Calculated Structural Parameters of NiTi Phases

Equilibrium configurations of B2, B19, B19′, and B33 structures of NiTi were obtained with WIEN2k by minimizing the energy with respect to atomic positions and unit-cell parameters. The convergence of the atomic positions was considered to be achieved when a difference of the atomic force acting on each atom was lower than 0.1 mRy/$a.u.$ In order to calculate the cell parameters, an optimization was performed consisting in minimizing the energy with respect to each degree of freedom in a sequential manner. These sequential optimization steps were repeated cyclically until an energy difference less than 0.01 mRy was achieved. Details about this procedure are explained in Appendix A.

Ground-state calculations were performed using a 2.0 $a.u.$ muffin-tin radius for both Ni and Ti in the B2 structure and a 2.2 $a.u.$ radius for the other structures. Convergence test of the bulk modulus as a function of $R_{\mathrm{mt}}K_{\mathrm{max}}$ were done, where K_{max} is the magnitude of the largest $\mathbf{k}$ vector in the basis set. The results showed that a value of $R_{\mathrm{mt}}K_{\mathrm{max}} \geqslant 8$ was large enough to have an accurate calculation without being computationally time consuming.

For the $\mathbf{k}$-space integration, 5000 k-points for B2 structure and 2500 for the other structures in the first Brillouin zone were used. Self-consistent calculations were considered to be converged when the total energy variations were lower than 0.001 mRy. The Fermi energy was calculated using a Gaussian-smearing method, with a width of 0.01 Ry. In all calculations, the $3s^2\ 3p^6\ 4s^2\ 3d^8$ states of Ni and $3s^2\ 3p^6\ 4s^2\ 3d^2$ states of the Ti atoms were treated as valence electrons. The exchange-correlation contribution to the potential was treated by PBE functional [47].

Table 5.1 summarizes the calculated and measured lattices parameters, volume, and energy differences with respect to the energy of the B2 structure for the four NiTi phases considered. As can be seen, all the results are in good agreement with available experimental data as well as theoretical [105, 104] results. No experimental data for the B33 structure are available in literature.

Table 5.1: Calculated and measured lattice parameters a, b, and c (in atomic units, *a.u.*), angle γ (in degrees), volume (in $a.u.^3$/atom), and total energies relative to the B2 structure (in mRy/atom). B2 lattice parameters are presented for the tetragonal cell ($B2_T$), which contains two Ni and two Ti atoms, in order to allow an easier comparison with the other four-atom structures.

		a	b	c	γ	volume	$E - E_{B2}$
$B2_T$	Present	8.040	5.685	8.040		183.782	0.000
	Theory [105]	8.068	5.705	8.068		185.689	
	Theory [104]	8.039	5.684	8.039		183.666	
	Experiment [111]	8.052	5.694	8.052		184.584	
B19	Present	7.883	5.371	8.696		184.079	–6.980
	Theory [105]	7.899	5.410	8.755		187.080	
	Theory [104]	7.782	5.471	8.664		184.434	
	Experiment [120]	7.982	5.478	8.527		186.344	
B19′	Present	9.040	5.561	7.611	102.76	186.579	–9.328
	Theory [105]	8.838	5.512	7.704	98.00	185.850	
	Theory [104]	8.853	5.558	7.625	97.78	185.865	
	Experiment [118]	8.780	5.476	7.763	97.78	184.909	
B33	Present	9.320	5.537	7.592	107.27	187.054	–9.456
	Theory [105]	9.313	5.543	7.606	107.00	187.720	
	Theory [104]	9.356	5.580	7.544	108.52	186.732	

However, values calculated in the present work are in good agreement with calculations made by Huang *et al.* [108]. γ was calculated for B19′ and B33 only. In the former case, there are some differences, around 5%, with respect to both experimental and theoretical results. The reason is that in Refs. [105, 104]. The authors used experimental values of γ, with the aim of keeping the calculation as close as possible to the experiments. However, our calculations show that some elastic constant, *e.g.* c_{55}, are very sensitive to this angle, and it cannot be fixed to a given value, but rather it must be optimized in order to be in the minimum of the energy-strain curve. This point will be addressed in Section 5.3.3.

In Table 5.2, the atomic positions of the structures B2, B19, B19′, and B33 are shown. Again, results of the present work are in good agreement with both experimental as well as previous theoretical results.

Formation energies for every phase were calculated as the difference between the total energy of the corresponding phase, E_{NiTi}, and the average of the lowest

Table 5.2: Space group (No.) and relaxed atomic positions for the structures B2, B19, B19′, and B33. The atomic positions are given in fractional atomic coordinates. Multiplicity and Wyckoff positions are shown in the column labeled "site".

	space group		atom	site	x	y	z
B2	$Pm\bar{3}m$ (221)	Present	Ni	$1a$	0	0	0
			Ti	$1b$	1/2	1/2	1/2
B19	$Pmma$ (51)	Present	Ni	$2e$	1/4	0	0.6838
			Ti	$2f$	1/4	1/2	0.2230
		Theory [121]	Ni	$2e$	1/4	0	0.6830
			Ti	$2f$	1/4	1/2	0.2240
B19′	$P2_1/m$ (11)	Present	Ni	$2e$	0.6708	0.0655	1/4
			Ti	$2e$	0.2150	0.3842	1/4
		Experiment [118]	Ni	$2e$	0.6752	0.0372	1/4
			Ti	$2e$	0.2164	0.4176	1/4
B33	$P2_1/m$ (11)	Present	Ni	$2e$	0.6699	0.0849	1/4
			Ti	$2e$	0.2137	0.3569	1/4
		Theory [108]	Ni	$2e$	0.6730	0.0860	1/4
			Ti	$2e$	0.2140	0.3580	1/4

energy phases of spin-polarized elemental Ni (fcc) and Ti (hcp) as

$$E_{\text{formation}} = E_{\text{NiTi}} - \left(\frac{1}{2}E_{\text{fccNi}} + \frac{1}{2}E_{\text{hcpTi}}\right). \tag{5.1}$$

Optimized lattice parameters and total energy for fcc Ni and hcp Ti were calculated with the same computational parameters. A spin-polarized calculation was performed for fcc Ni and the resulting magnetic moment was $0.63\mu_B$.

In Table 5.3, experimental and theoretical formation energies for different NiTi phases are listed. As can be seen, the results obtained in this work are in good agreement both with experimental measurements and previous calculations. For the B2 structure, the calculated formation energy is –34.1 kJ/(mol.atom) and this value is very close to the experimental ones of –33.9 kJ/(mol.atom) and –34.0 kJ/(mol.atom) obtained by Gachon *et al.* [122] and Kubaschewski *et al.* [123], respectively. It is also in accordance with the value calculated by Hatcher *et al.* [105]. Unfortunately, no experimental formation energies for B19, B19′, and B33 are available in literature. Nonetheless, results of the present work were compared with the ones by Hatcher *et al.* [105], and the agreement is again satisfactory.

The crystal structure of the R phase is still controversial in spite of the many experimental and theoretical studies. We will discuss the R phase and present

Table 5.3: Formation energies of the NiTi structures, calculated according Eq. (5.1).

Structure	References	Formation energy (kJ/mol.atom)
B2	Present	–34.1
	Experiment [122]	–33.9
	Experiment [123]	–34.0
	Theory [105]	–34.1
	Theory [119]	–38.0
	Theory [124]	–36.0
B19	Present	–38.7
	Theory [105]	–38.0
B19′	Present	–40.3
	Theory [105]	–39.5
B33	Present	–40.4
	Theory [105]	–39.9

our computational results in the following section.

5.3.2 Structural Parameters of the R Phase

The goal of the this section is to refine more accurately the atomic positions in the R phase and clarify computationally the controversy in the determination of its space group.

In Figure 5.5, we show schematic illustrations of the crystal structures for different space groups. Left and right sides, respectively, correspond to the space groups $P3$ (No. 143) and $P\overline{3}$ (No. 147). $P31m$ (No. 157) can be constructed from the left structure of Figure 5.5 in such a way that the two atoms at the Z_1 and Z_4 planes are constrained to be in the same level, *i.e.*, $\Delta_1 = \Delta_2$ and $\Delta_3 = \Delta_4$. Also in the right side of Figure 5.5, if $\Delta_1 = \Delta_2 = 0$ the structure will obtain $P\overline{3}1m$ symmetry (No. 164).

Our *ab initio* calculations were carried out using the Quantum ESPRESSO code. PBE for the exchange-correction energy and ultrasoft pseudo-potentials were employed. A kinetic-energy cut-off of 80 and 800 Ry was used for the plane-wave expansion of wave-function and electron densities, respectively. The Brillouin zone integration was calculated by $7 \times 7 \times 9$ Monkhorst-pack meshes for all the crystal structures. Geometry optimization was considered to be converged when the difference of the total energies between the last iterations did not exceed 10^{-8} Ry. The convergence criterion is satisfied when the force components were

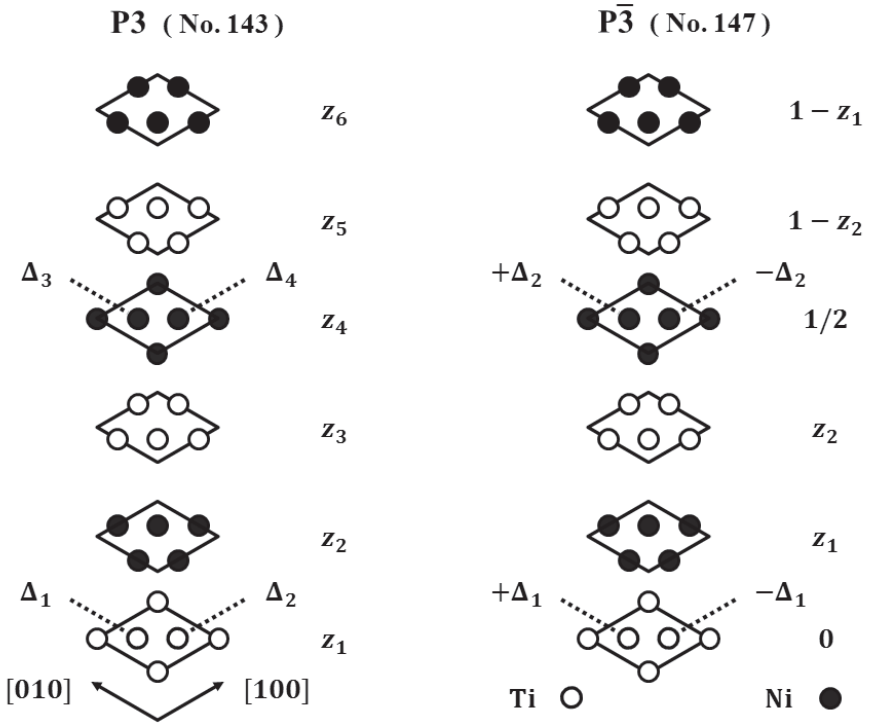

Figure 5.5: Illustration of space group $P3$ (left) and space group $P\bar{3}$ (right), representing possible structures of the R phase. z_i indicate planes of atoms with different z coordinates, and Δ_i refer to shifts out of these planes. If, in the left side, $\Delta_1 = \Delta_2$ and $\Delta_3 = \Delta_4$ the structure turns into space group $P31m$ (No. 157). If, on the right side, $\Delta_1 = \Delta_2 = 0$ the structure changes to space group $P\bar{3}1m$ (No. 164). The illustration is based on Ref. [114]

smaller than 10^{-8} Ry/$a.u.$. The geometry optimizations included not only the atomic positions, but also the lattice parameters.

Table 5.4 shows the atomic positions of the R phase for the space groups $P3$, $P\bar{3}$, $P31m$, and $P\bar{3}1m$ before and after geometry optimization. The initial positions are taken from [114, 115]. We find the space groups unchanged after geometry optimization. The total-energy investigation shows that the difference in the energies of $P3$ and $P31m$ is negligible (10^{-6} mRy/atom). Therefore, their energy can be considered as the minimum energy. The energy difference between $P\bar{3}$ and the minimum energy and the difference between the energy of $P\bar{3}1m$ and the minimum energy, are 0.192 mRy/atom and 1.227 mRy/atom, respectively. We conclude that $P3$ and $P31m$ are possible crystal structures for the R phase of NiTi. However, as alloying can change the structure of a material, these results do not necessarily contradict experiments. The small amounts of Fe or Al substituting Ni atoms may change the symmetry of the R phase from $P3$ or $P31m$ to other symmetries.

5.3.3 Elastic Constants

In this section, we show the elastic constants for different phases of NiTi and from this we will draw some conclusions which help us to better understand the martensitic transformation.

In Table 5.5, we list the calculated and experimental elastic constants for the B2 structure. The experimental elastic constants were performed by Mercier [126] at 298 K which is the lowest temperature of B2 to be stable. Brill [125] measured the elastic constants at 400 K. The comparison between these two measurements shows that the values of c_{11}, c_{12}, c', and B decrease by increasing temperature. This fact proves the consequence of the Landau-Devonshire theory that increasing the temperature softens the elastic constants. Comparing our result with Mercier's measurements [126], we observe that our calculated values overestimate c_{11}, c_{12}, and c_{44} by 7%, 22%, and 57%, respectively. The DFT calculations yield ground-state properties of materials at zero K, such that temperature effects are not taken into account. Therefore, the elastic constants are usually overestimated. Our results show that c_{12} is smaller than c_{11}, yielding a positive value for c', while Wagner and Windl [104] reported c'= -16 GPa.

A crystal is stable against a homogeneous deformation if the elastic constant matrix $c_{\alpha\beta}$ has positive eigenvalues. If one or more of the eigenvalues becomes negative, the crystal may distort continuously to a new structure with a symmetry determined by the eigenvector of that eigenvalue [127]. The values of $c_{11} - c_{12}$ ($=2\,c'$) and $(\eta, -\eta, 0, 0, 0, 0)$ are the eigenvalue and the corresponding eigenvector of the cubic elastic-constant matrix, respectively. Therefore, a negative value of c' would meant that the B2 structure is unstable, and under stress this structure has a tendency to change the lattice shape by a tetragonal distortion. This is a contradiction to measurements and calculations.

In Table 5.6, we show the calculated independent elastic constants of the structures B19, B19′, and B33. We also present the elastic constants of B2 transformed to the reference frame of the tetragonal supercell labeled as $B2_T$. Moreover, in order to have a direct comparison, we have transformed the elastic constants calculated by Hatcher [105] and Wangner and Windl [104] to the Cartesian coordinate system used by us. The calculated bulk moduli for B2 and B19′ (and B33) are almost equal. Also, the unit-cell volume of these structures are equal, which indicates that during the martensitic transformation the volume does not change drastically. This has also been reported in experiment [107]. Another noticeable result is that the values of c_{44} and c_{55} of the $B2_T$ phase are less than those values in the B19′ and B33 phases. This point confirms the softening of the elastic constants during the forward martensitic transformation.

The values of c_{66} for $B2_T$, B19′, and B33 are almost equal, and relatively small compared to other elastic constants. c_{66} corresponds to the deformation of γ and clarifies two important points: First, the $B2_T$ structure is very unstable

under shear deformation. Second, due to the small c_{66} of B19′ and B33, the calculation of those elastic constants which are calculated by γ angle distortion, *i.e.*, c_{16}, c_{26}, and c_{36} are numerically problematic. In these cases, as discussed in Section 4.5.1, the corresponding energy-strain curves of these elastic constants are not relatively deep and the noise effect on such curves are high. As can be seen in Table 5.6, large discrepancies occur in these elastic constants. For instance, we have calculated a positive (negative) c_{16} (c_{36}) for B19′ but Refs. [105, 104] obtained negative (positive) values. The energy *vs.* strain curve of the small elastic constant is relatively flat and it is strongly affected by noise. Therefore, such an elastic constant requires precise calculation. As shown in Section 4.2, `ElaStic` has the proper features for precise elastic-constant calculations.

Our result for c_{44} of the B19 structure, in contrast to Ref. [105], is negative. c_{44} is an eigenvalue of the orthorhombic elastic constant matrix. As we discussed above, this means that the B19 structure of NiTi is an unstable structure. It might, however, become stable if alloyed with Cu.

In Table 5.7, we show the polycrystalline elastic moduli, *i.e.*, the bulk, shear, and Young's moduli as well as Poisson's ratio as obtained from the Voigt and Reuss definitions, denoted with subscripts V and R, respectively, and the Hill averaged modulus, subscripted with H, along with experimental and theoretical comparisons. Our calculations and the previous experimental results for the elastic constants of the B2 phase are in good agreement, and our results compare favorably with previously reported theoretical results [105]. As discussed above, Wagner and Windl [104] obtained $c_{12} > c_{11}$, which yielded a fully unstable B2 phase. For this reason, the macroscopic elastic parameters calculated from their elastic constants are not comparable to the experimental values. Moreover, we list the Zener anisotropy ratio, A, and the $G_{\mathrm{H}}/B_{\mathrm{H}}$ ratio in Table 5.7. The Zener anisotropy ratio for cubic materials is defined as

$$A = \frac{c_{44}}{c'} = \frac{2c_{44}}{c_{11} - c_{12}}\,. \tag{5.2}$$

In isotropic cubic materials, c_{44} is equal to c' and A is equal to one. The experimental values of A for SMA materials are around 10 or more but as shown in Table 5.7, the experimental value for NiTi is around 2. Our calculations show that the A ratio of the B2 structure is less than ten which is a typical value for other types of SMAs.

According to Pugh's empirical rule [128] the ductile/brittle behavior of a material is closely related to the ratio of G/B or the Poisson ratio, ν. Materials exhibiting a G/B ratio less than 0.57 are more likely to be ductile. A high value of G/B and low value of ν is associated with brittleness, so an increase in G/B or decrease in ν indicates a decrease in ductility. We have obtained a G_H/B_H ratio of 0.15, in a good agreement with experimental data; indicating the B2 structure is ductile.

Table 5.8, like Table 5.7, lists the polycrystalline moduli for the phases B19, B19′, and B33 along with the results for the B2 structure. We do not present the Zener anisotropy ratio, because its generalization to non-cubic materials is not straightforward. By comparing the elastic properties of these phases, several trends appear. First, the Voigt bulk modulus is very similar among the phases. Second, the shear modulus increases when going from B2 to other phases. Third, the Young's modulus increases from the B2 to the B19′ phase. This fact is consistent with the Muller-Achenbach-Seelecke model [129], which requires the Young's modulus of the austenite to be smaller than that of the martensite phase. Finally, according to Pugh's empirical rule, during the martensitic transformation, ductility decreases because the $G_{\mathrm{H}}/B_{\mathrm{H}}$ ratio increases, and ν_{H} decreases from the B2 phase to the B19′ phase.

To conclude, we have accurately calculated elastic properties and obtained both single crystal elastic constants and macroscopic elastic parameters. We have found, in contrast to previous calculations, the B2 phase to be a stable phase, and in the same way we have shown that the B19 structure is an unstable phase and cannot be an intermediate phase for the NiTi shape-memory alloy. We expect that the $\mathrm{B2_T}$ structure has a tendency to deform the angle γ because of the small c_{66} value. For these reasons, we believe that the martensitic transformation is more likely to be a direct transformation from the B2 phase to the B19′ phase. Also, during this transformation the volume does not change and ductility decreases.

Table 5.4: Internal coordinates before and after the structural optimization for different space groups of the R phase. Multiplicity and Wyckoff positions are labeled as "site".

	before relaxation				after relaxation			
atom	site	x	y	z	site	x	y	z
	$P3$ [114]				$P3$			
Ti	$1a$	0	0	0	$1a$	0	0	0
Ti	$1b$	1/3	2/3	0.0833	$1b$	1/3	2/3	0.0764
Ti	$1c$	2/3	1/3	0.0092	$1c$	2/3	1/3	0.9999
Ti	$3d$	0.3351	0.9953	0.3612	$3d$	0.3333	0.9867	0.3796
Ti	$3d$	0.6779	0.0106	0.6842	$3d$	0.6752	0.0085	0.6862
Ni	$1a$	0	0	0.4572	$1a$	0	0	0.4621
Ni	$1b$	1/3	2/3	0.5411	$1b$	1/3	2/3	0.6221
Ni	$1c$	2/3	1/3	0.3962	$1c$	2/3	1/3	0.4621
Ni	$3d$	0.3188	0.9774	0.8542	$3d$	0.3333	0.9799	0.8991
Ni	$3d$	0.6886	0.0215	0.1602	$3d$	0.6911	0.0245	0.1792
	$P31m$ [115]				$P31m$			
Ti	$1a$	0	0	0	$1a$	0	0	0
Ti	$2b$	1/3	2/3	0.9100	$2b$	1/3	2/3	0.9236
Ti	$3d$	0.3220	0	0.2990	$3d$	0.3201	0	0.3032
Ti	$3d$	0.6580	0	0.6030	$3d$	0.6582	0	0.6098
Ni	$1a$	0	0	0.5360	$1a$	0	0	0.5457
Ni	$2b$	1/3	2/3	0.3770	$2b$	1/3	2/3	0.3857
Ni	$3d$	0.3160	0	0.8180	$3d$	0.3132	0	0.8227
Ni	$3d$	0.6380	0	0.0950	$3d$	0.6422	0	0.1028
	$P\bar{3}$ [114]				$P\bar{3}$			
Ti	$1a$	0	0	0	$1a$	0	0	0
Ti	$2d$	1/3	2/3	0.0450	$2d$	1/3	2/3	0.0399
Ti	$6g$	0.3460	0.9980	0.3460	$6g$	0.3308	0.9871	0.3449
Ni	$1b$	0	0	1/2	$1b$	0	0	1/2
Ni	$2d$	1/3	2/3	0.5470	$2d$	1/3	2/3	0.5834
Ni	$6g$	0.3320	0.9920	0.8150	$6g$	0.3138	0.9741	0.8581
	$P\bar{3}1m$ [114]				$P\bar{3}1m$			
Ti	$1a$	0	0	0	$1a$	0	0	0
Ti	$2c$	1/3	2/3	0	$2c$	1/3	2/3	0
Ti	$6k$	0.3047	0	0.3594	$6k$	0.3333	0	0.3369
Ni	$1b$	0	0	1/2	$1b$	0	0	1/2
Ni	$2d$	1/3	2/3	1/2	$2d$	1/3	2/3	1/2
Ni	$6k$	0.3038	0	0.8453	$6k$	0.3333	0	0.8458

Table 5.5: Calculated and experimental independent elastic constants, given in GPa, for the B2 structure of NiTi. B is calculated by applying the Birch-Murnaghan fit, Eq. (C.2).

	B2	B2 [a]	B2 [b]	B2 [105]	B2 [104]
c_{11}	173	137	162	183	138
c_{12}	157	120	129	146	169
c_{44}	50	34	34	46	40
c'	8	8	16	19	–16
B	161	126	142	159	159

[a] Experiment [125] at 400 K
[b] Experiment [126] at 298 K

Table 5.6: Calculated independent elastic constants, given in GPa, for NiTi structures. The elastic constants in the first column, $B2_T$, are obtained by transforming the B2 elastic constants to the tetragonal supercell structure to provide comparison to other structures. The bulk modulus B is calculated applying the Birch-Murnaghan equation of state, Eq. (C.2). In order to facilitate comparison between our elastic constants and the results by Hatcher [105] and Wagner and Windl [104], we have transformed their results into the Cartesian coordinate system which has been used as reference in our calculations.

	$B2_T$	B19	[105]	[104]	B19′	[105]	[104]	B33	[105]	[104]
c_{11}	215	256	254	238	254	249	223	261	249	226
c_{12}	115	158	118	127	104	107	99	93	99	113
c_{13}	157	110	105	129	136	129	129	139	133	137
c_{16}					21	–15	–27	–2	–27	–33
c_{22}		143	240	203	180	212	200	191	189	179
c_{23}		105	150	92	151	125	125	154	131	134
c_{26}					0	1	–4	1	11	18
c_{33}	173	238	192	212	248	245	214	249	232	231
c_{36}					–6	3	9	2	15	–1
c_{44}	50	–28	73	–32	91	87	76	94	99	84
c_{45}					–3	4	4	0	–4	–2
c_{55}		56	53	49	93	86	77	98	96	90
c_{66}	8	72	66	65	5	66	21	7	44	23
B	161	153	156	150	158	159	152	159	156	156

Table 5.7: Calculated macroscopic elastic properties for NiTi in the B2 structure. We report the Hill bulk modulus B_{H}, only, because for cubic structures $B_{\mathrm{V}} = B_{\mathrm{R}} = B_{\mathrm{H}}$. All results are given in GPa, except for A, $G_{\mathrm{H}}/B_{\mathrm{H}}$, and ν_{H} which are dimensionless.

	B2	B2 [a]	B2 [b]	B2 [105]	B2 [104]
A	6.32	4.00	2.06	2.49	–2.58
B_{H}	162	126	140	158	159
G_{V}	33	24	27	35	18
G_{R}	16	15	24	29	–93
G_{H}	25	20	25	32	–37
$G_{\mathrm{H}}/B_{\mathrm{H}}$	0.15	0.16	0.18	0.20	–0.23
ν_{H}	0.43	0.43	0.41	0.41	0.63
E_{V}	94	67	76	98	51
E_{R}	47	45	68	82	–345
E_{H}	71	56	72	90	–123

[a] Experiment [125] at 400 K
[b] Experiment [126] at 298 K

Table 5.8: Calculated macroscopic elastic properties for different NiTi structures. Results are given in GPa, except for $G_{\mathrm{H}}/B_{\mathrm{H}}$ and ν_{H} which are dimensionless.

	B2	B19		B19′			B33		
		[105]	[104]		[105]	[104]		[105]	[104]
B_{V}	162	154	159	150	163	159	152	163	155	156
B_{R}	162	134	156	146	127	157	143	154	151	151
B_{H}	162	143	158	148	145	158	148	159	153	154
G_{V}	33	38	59	37	57	71	56	61	68	56
G_{R}	16	63	54	111	5	67	34	24	53	23
G_{H}	25	51	57	74	31	69	45	42	60	39
$G_{\mathrm{H}}/B_{\mathrm{H}}$	0.15	0.36	0.36	0.50	0.21	0.44	0.37	0.26	0.39	0.25
ν_{H}	0.43	0.34	0.34	0.29	0.40	0.31	0.36	0.38	0.33	0.38
E_{V}	94	104	158	102	153	185	149	162	179	151
E_{R}	47	164	145	265	15	176	95	68	141	63
E_{H}	71	136	152	189	87	181	122	116	160	108

A Elastic Constants and Crystal Symmetry

In the most general case, the number of independent SOECs and TOECs are 21 and 56, respectively. However, the crystal symmetry can further reduce the number of independent elastic constants. The elastic matrices are invariant under inversion, which means that if the reference axes are inverted, $Ox_i \Longrightarrow -Ox_i$, the components $c_{\alpha\beta}$ ($s_{\alpha\beta}$) and $c_{\alpha\beta\gamma}$ ($s_{\alpha\beta\gamma}$) do not change. In addition, for a specific crystal, utilizing all symmetries and analyzing their effect on the elastic-constant matrices, allows the determination of the corresponding number of independent elastic constants. In what follows, we discuss how the independent $c_{\alpha\beta}$ can be found by using the symmetry of the crystal.

Consider, for instance, a cubic crystal, with the $\boldsymbol{a}, \boldsymbol{b}$, and $\boldsymbol{c}$ lattice vectors along the Ox_1, Ox_2, and Ox_3 directions, respectively. In cubic crystals, there is a single four-fold (90°) rotation axis parallel to every directions. In the following, we investigate how $c_{\alpha\beta}$ would change, if the x_1x_2 plane is rotated by 90° in counter-clockwise direction. Under this transformation elastic constants for the cubic structure must not change. According to this, the rotation axes transform as follows

$$Ox_1 \Longrightarrow Ox_2, \quad Ox_2 \Longrightarrow -Ox_1, \quad Ox_3 \Longrightarrow Ox_3$$

Hence, in the Cartesian notation, the index pairs transform as follows

$$\begin{aligned} &11 \Longrightarrow 22, \quad 12 \Longrightarrow -12, \quad 13 \Longrightarrow 23, \\ &22 \Longrightarrow 11, \quad 23 \Longrightarrow -13, \quad 33 \Longrightarrow 33. \end{aligned} \tag{A.1}$$

In the two-subscript notation, these transformations are:

$$1 \Longrightarrow 2, \quad 2 \Longrightarrow 1, \quad 3 \Longrightarrow 3, \quad 4 \Longrightarrow -5, \quad 5 \Longrightarrow 4, \quad 6 \Longrightarrow -6.$$

The transformed $c_{\alpha\beta}$ can be written by replacing the new indexes, as

$$\begin{bmatrix} c_{22} & c_{21} & c_{23} & -c_{25} & c_{24} & -c_{26} \\ & c_{11} & c_{13} & -c_{15} & c_{14} & -c_{16} \\ & & c_{33} & -c_{35} & c_{34} & -c_{36} \\ & & & c_{55} & -c_{45} & c_{56} \\ & & & & c_{44} & -c_{46} \\ & & & & & c_{66} \end{bmatrix}.$$

We have not repeated the lower left-hand half of the matrix, since the matrix is symmetric. Also, if we rotate the x_1x_2 plane by 270° in counter-clockwise direction, the $c_{\alpha\beta}$ matrix should not change. If we do so with the same procedure which is explained above, following matrix would be the transformed matrix:

$$\begin{bmatrix} c_{22} & c_{21} & c_{23} & c_{25} & -c_{24} & -c_{26} \\ & c_{11} & c_{13} & c_{15} & -c_{14} & -c_{16} \\ & & c_{33} & c_{35} & -c_{34} & -c_{36} \\ & & & c_{55} & -c_{45} & -c_{56} \\ & & & & c_{44} & c_{46} \\ & & & & & c_{66} \end{bmatrix}.$$

If we repeat whole procedure for the x_2x_3 and x_3x_1 planes, we get four more transformed matrices which in principle must be equal to general elastic-constants matrix. After equating these matrices, component by component, with the general $c_{\alpha\beta}$ matrix, the relation between matrix components indices is displayed by the following scheme,

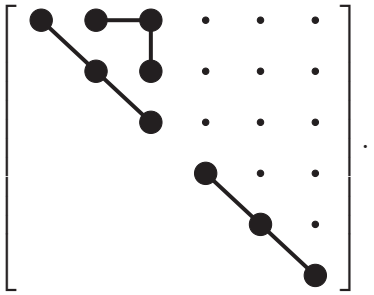

In this kind of presentation, we introduce a special notation for denoting non-zero components of the $c_{\alpha\beta}$ (or $s_{\alpha\beta}$) matrix as well as their relations. The keys of notation are:

- • denotes a component which is zero.
- ● denotes a non-zero component. A line joining two heavy dots means that the two components are numerically equal.

○ linked by a line denotes components whose absolute values are equal, but opposite in sign; black and white circles indicate positive and negative sign, respectively.

★ is equal to $\frac{1}{2}(c_{11} - c_{12})$ and $2(s_{11} - s_{12})$ for $c_{\alpha\beta}$ and $s_{\alpha\beta}$ matrices, respectively.

According to this notation, the number of independent elastic constants of a cubic crystal, is reduced from 21 to 3.

A classification of the different crystal structures including the corresponding number of independent SOECs and TOECs is given in Table A.1.

Table A.1: Classification of crystal families and systems. Centering type, Laue group, Hermann-Mauguin point-group symbols, and space-group numbers (SGN) are provided together with the number of independent SOECs and TOECs.

Crystal family	Crystal system	Centering type(s)	Laue group	Point group classes	SGN	No. of SOECs	No. of TOECs
Cubic	Cubic	P, F, I	C_I	$432,\ \bar{4}3m,\ \frac{4}{m}\bar{3}\frac{2}{m}$	207–230	3	6
			C_{II}	$23,\ \frac{2}{m}\bar{3}$	195–206		8
Hexagonal	Hexagonal	P	H_I	$622, 6mm, \bar{6}2m, \frac{6}{m}\frac{2}{m}\frac{2}{m}$	177–194	5	10
			H_{II}	$6,\ \bar{6},\ \frac{6}{m}$	168–176		12
	Trigonal	P, R	R_I	$32,\ 3m,\ \bar{3}\frac{2}{m}$	149–167	6	14
			R_{II}	$3,\ \bar{3}$	143–148	7	20
Tetragonal	Tetragonal	P, I	T_I	$422,\ 4mm,\ \bar{4}2m,\ \frac{4}{m}\frac{2}{m}\frac{2}{m}$	89–142	6	12
			T_{II}	$4, \bar{4},\ \frac{4}{m}$	75–88	7	16
Orthorhombic	Orthorhombic	P, C, F, I	O	$222,\ mm2,\ \frac{2}{m}\frac{2}{m}\frac{2}{m}$	16–74	9	20
Monoclinic	Monoclinic	P, C	M	$m,\ 2,\ \frac{2}{m}$	3–15	13	32
Triclinic	Triclinic	P	N	$1,\ \bar{1}$	1 and 2	21	56

A.1 Single-Crystal Elastic Constants

In general, crystal properties which are expressed by a tensor or a matrix, like elastic properties, depend on the choice of both the crystal axes and the Cartesian reference frame. This means the value of the elastic constants may change from one choice to another. Therefore, comparison of calculated elastic constants with results of other calculations or experimental data is only possible provided the chosen crystal axes and reference frame are identical. For the sake of clarity, we present the definition of the *standard reference* (STD) for the crystal axes and the Cartesian reference frame which are used by `ElaStic` when dealing with different density-functional theory computer packages. In addition, we show the independent components of the second- and third-order elastic matrices, with Voigt notation, for all the crystal types following from the STD. In the determination of the STD, `ElaStic` follows the *Standards on piezoelectric crystals* (1949), as recommended in Ref. [32].

The term *crystal* is usually applied to solids that have structural symmetry. Depending on their degree of symmetry, crystals are commonly classified in six *systems*: triclinic (the least symmetrical), monoclinic, orthorhombic, tetragonal, hexagonal (we treat trigonal crystals as a division of the hexagonal system), and cubic. The six systems in turn are divided into point-classes (*class*) according to their symmetry with respect to a point. There are thirty-two such classes. We have listed these classes in the fifth column of Table A.1.

Before we go on, it should be mentioned that in the next section $\boldsymbol{a}, \boldsymbol{b}$, and $\boldsymbol{c}$ are indicating three vectors which describe the crystal lattice and α, β, γ are the angles between $\boldsymbol{b}$ and $\boldsymbol{c}$, $\boldsymbol{a}$ and $\boldsymbol{c}$, and $\boldsymbol{a}$ and $\boldsymbol{b}$, respectively.

A.1.1 Triclinic Lattice

In triclinic systems, the lengths of the three lattice vectors, $\boldsymbol{a}, \boldsymbol{b}$, and $\boldsymbol{c}$ are unequal and the angles α, β, and γ are unequal too. There are six equally simple ways to define Cartesian coordinates with the axes Ox_1, Ox_2, and Ox_3. The most logical relation is the one which associates the axes Ox_1, Ox_2, and Ox_3 most closely with a, b, and c, respectively. The Ox_1 axis is put along a, Ox_2 in the $\boldsymbol{ab}$ plane and Ox_3 is perpendicular to the x_1x_2 plane. `ElaStic` takes these axes as Cartesian coordinates for the triclinic system. Triclinic structures have 21 independent

SOECs, and the full elastic constants matrix appears as follows:

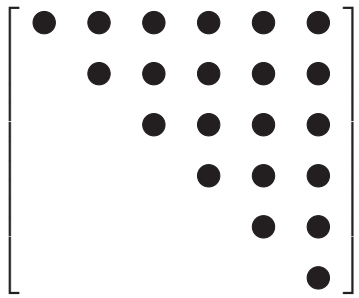

(A.2)

A.1.2 Monoclinic Lattice

If a crystal has a single axis of two-fold symmetry, or a single plane of reflection symmetry, or both, it belongs to the monoclinic system. The two-fold axis or the normal to the plane of symmetry, which are the same if both exist, is called the *unique* axis. The unique axis is usually assigned to $\boldsymbol{b}$ and put along the Ox_2 axis, and β is the angle between $+\boldsymbol{a}$ and $+\boldsymbol{c}$ and always obtuse. Then, there are two choices for the Ox_1 and Ox_3 axes, since either the Ox_1 axis is along the $\boldsymbol{a}$ vector, or, the Ox_3 axis is parallel to $\boldsymbol{c}$. According to the STD, both of these choices are acceptable. We use $\mathrm{M}^{(\mathbf{b})}$, in this thesis, for this type of monoclinic system. In general, the monoclinic system has 13 independent elastic constants. The corresponding elastic constants for $\mathrm{M}^{(\mathbf{b})}$ have the following form:

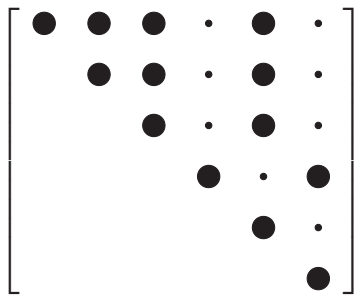

(A.3)

For monoclinic systems with m point-group, there is an alternative choice for the axes Ox_1, Ox_2, and Ox_3. The unique axis is assigned to $\boldsymbol{c}$ which is aligned along Ox_3, and γ is associated with the angle between $+\boldsymbol{a}$ and $+\boldsymbol{b}$. We use the abbreviation $\mathrm{M}^{(\mathbf{c})}$ for this type of monoclinic systems. In this case, there are also two choices for the Cartesian coordinates, namely either Ox_1 axis along the $\boldsymbol{a}$ vector or Ox_2 axis parallel to $\boldsymbol{b}$. The elastic constant matrix for $\mathrm{M}^{(\mathbf{c})}$ has the

form:

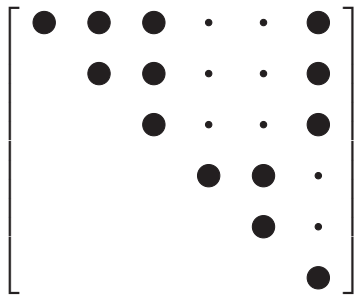

(A.4)

A.1.3 Orthorhombic Lattice

Crystals having three mutually perpendicular two-fold axes, or two mutually perpendicular planes of reflection symmetry, or both, belong to the orthorhombic system. The most logical way to define Cartesian coordinates is Ox_1 along $\boldsymbol{a}$, Ox_2 along $\boldsymbol{b}$, and Ox_3 along $\boldsymbol{c}$. Orthorhombic crystals have 9 independent elastic constants, with the elastic constant matrix having the following form:

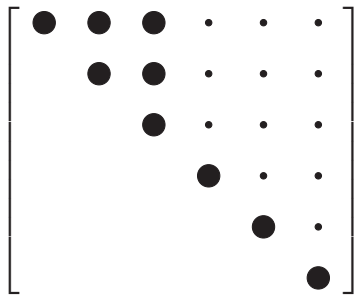

(A.5)

A.1.4 Tetragonal Lattice

Crystals having a single four-fold rotation axis or a four-fold rotoinversion axis belong to the tetragonal system. The $\boldsymbol{c}$ axis is always taken along this four-fold axis, and the Ox_3 axis lies along $\boldsymbol{c}$. The lattice vectors $\boldsymbol{a}$ and $\boldsymbol{b}$ are equivalent in tetragonal systems. The Ox_1 axis may be parallel to either $\boldsymbol{a}$ or $\boldsymbol{b}$; there are thus two possible sets of Ox_1 and Ox_2 axes. In the tetragonal crystal family there are the classes 4, $\overline{4}$, $\frac{4}{m}$, 422, $4mm$, $\overline{4}2m$, $\frac{4}{m}\frac{2}{m}\frac{2}{m}$. Three of these classes, *i.e.* 4, $\overline{4}$, $\frac{4}{m}$, have no two-fold symmetry axis. They form the Laue class $\mathrm{T_{II}}$, and have seven

independent elastic constants with the following matrix form:

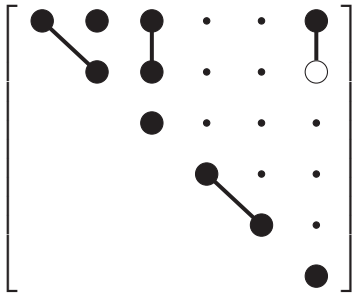

(A.6)

The other four point-group classes, *i.e.*, 422, $4mm$, $\overline{4}2m$, $\frac{4}{m}\frac{2}{m}\frac{2}{m}$ have a two-fold symmetry axis and constitute the Laue class $\mathrm{T_I}$. As a consequence of the higher symmetry, there are less independent elastic constants. The six independent elastic constants have the following matrix form:

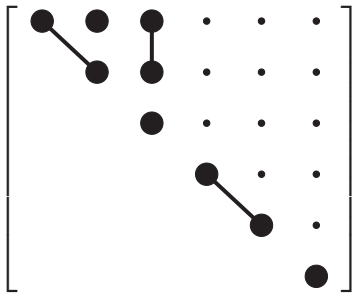

(A.7)

A.1.5 Hexagonal Lattice Family

The hexagonal family consists of the *trigonal* and primitive *hexagonal* crystal structures. The trigonal and hexagonal crystals are distinguished by an axis of three-fold and six-fold symmetry, respectively. This axis is always chosen as the $\boldsymbol{c}$ axis. There are three equivalent choices for the secondary lattice vectors, $\boldsymbol{a}_1, \boldsymbol{a}_2$, and $\boldsymbol{a}_3$, lying 120° apart in a plane normal to $\boldsymbol{c}$. According to the STD coordinate system, the Ox_3 axis is parallel to $\boldsymbol{c}$. The Ox_1 axis coincides in direction with any one of the $\boldsymbol{a}$ vectors. The Ox_2 axis is perpendicular to Ox_1 and Ox_3. There are five point-group classes for trigonal crystals. As you can see in Table A.1, trigonal crystals are classified into the subclasses $\mathrm{R_I}$ and $\mathrm{R_{II}}$, in Laue group notation. The matrices,

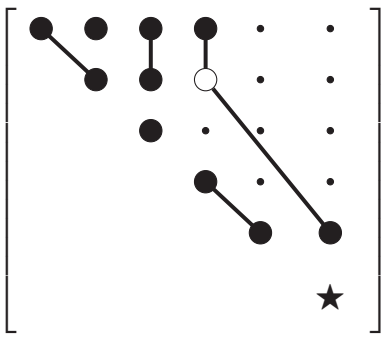

(A.8)

and

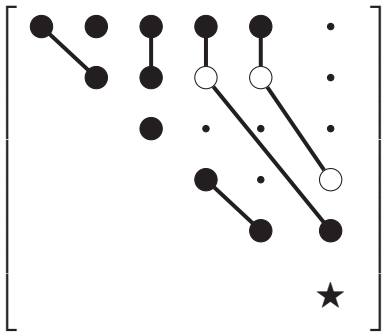

(A.9)

represent the elastic-constants matrix for R_I, for six, and R_{II}, with seven independent elastic constants, respectively. The meaning of the notation, in the matrix above, has been explained on page 77. Here, we give explicitly some of the relations between elastic constant components in these systems. For R_I crystals, the relations are

$$\begin{aligned} c_{24} &= -c_{14}, \quad c_{56} = -c_{24}, \quad c_{66} = \frac{1}{2}(c_{11} - c_{22}); \\ s_{24} &= -s_{14}, \quad s_{56} = -2s_{24}, \quad s_{66} = 2(s_{11} - s_{22}). \end{aligned} \tag{A.10}$$

For R_{II} crystals, the extra relations are

$$\begin{aligned} c_{24} &= -c_{14}, \quad c_{56} = -c_{24}, \\ c_{25} &= -c_{15}, \quad c_{46} = +c_{25}, \quad c_{66} = \frac{1}{2}(c_{11} - c_{22}), \\ s_{24} &= -s_{14}, \quad s_{56} = -2s_{24}, \\ s_{25} &= -s_{15}, \quad s_{46} = +2s_{25}, \quad s_{66} = 2(s_{11} - s_{22}). \end{aligned} \tag{A.11}$$

The following matrix shows the five non-zero components of hexagonal crystals and the relations between them:

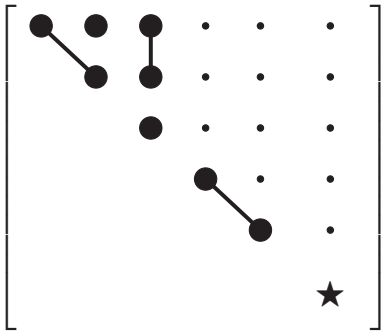

. (A.12)

A.1.6 Cubic Lattice

In the cubic family, the three equivalent lattice vectors are $\boldsymbol{a}$, $\boldsymbol{b}\,(|\boldsymbol{b}| = |\boldsymbol{a}|)$, and $\boldsymbol{c}\,(|\boldsymbol{c}| = |\boldsymbol{a}|)$, often called $\boldsymbol{a_1}, \boldsymbol{a_2}$, and $\boldsymbol{a_3}$. They are chosen parallel to the axes

of four-fold symmetry, or, if there is no true four-fold symmetry, then parallel to the two-fold axes. The Ox_1, Ox_2, and Ox_3 axes form a right-handed system parallel to the $\boldsymbol{a}, \boldsymbol{b}$, and $\boldsymbol{c}$, respectively. The following matrix represents the elastic constant matrix for cubic crystals:

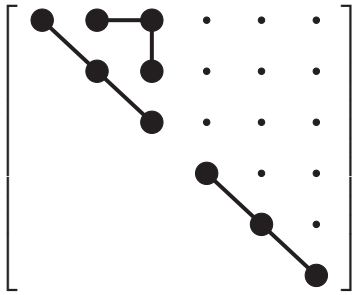

(A.13)

In order to prevent any confusion in applying the `ElaStic` tool, we show in Table A.2 the different choices of the default Cartesian reference frame for the codes considered in this thesis.

A.1.7 Symmetry of Non-Linear Elastic Constant

Similarly to the procedure used above for SOECs, the independent TOECs can be found by applying the crystal symmetries. In the subsequent Table A.3, we display the independent TOECs corresponding to some crystal type for the STD Cartesian coordinates.

Table A.3: Symmetry properties of the three dimensional matrix of TOECs for each Laue group. The three-digit numbers $\alpha\beta\gamma$ stand for $c_{\alpha\beta\gamma}$. They are defined according to Brugger elastic constants. Elastic constants are referred to Cartesian axes according to Table A.2.

N	M$^{(b)}$	M$^{(c)}$	**O**	T$_{II}$	T$_{I}$	R$_{II}$	R$_{I}$	H$_{II}$	H$_{I}$	C$_{II}$	C$_{I}$
111	111	111	111	111	111	111	111	111	111	111	111
112	112	112	112	112	112	112	112	112	112	112	112
113	113	113	113	113	113	113	113	113	113	113	112
114	0	0	0	0	0	114	114	0	0	0	0
115	115	0	0	0	0	115	0	0	0	0	0
116	0	116	0	116	0	116	0	116	0	0	0
122	122	122	122	112	112	*A*	*A*	*A*	*A*	113	112
123	123	123	123	123	123	123	123	123	123	123	123
124	0	0	0	0	0	124	124	0	0	0	0
125	125	0	0	0	0	125	0	0	0	0	0
126	0	126	0	0	0	–116	0	–116	0	0	0
133	133	133	133	133	133	133	133	133	133	112	112
134	0	0	0	0	0	134	134	0	0	0	0
135	135	0	0	0	0	135	0	0	0	0	0
136	0	136	0	136	0	0	0	0	0	0	0
144	144	144	144	144	144	144	144	144	144	144	144
145	0	145	0	145	0	145	0	145	0	0	0
146	146	0	0	0	0	*I*	0	0	0	0	0
155	155	155	155	155	155	155	155	155	155	155	155
156	0	0	0	0	0	*F*	*F*	0	0	0	0
166	166	166	166	166	166	*B*	*B*	*B*	*B*	166	155
222	222	222	222	111	111	222	222	222	222	111	111
223	223	223	223	113	113	113	113	113	113	112	112
224	0	0	0	0	0	*G*	*G*	0	0	0	0
225	225	0	0	0	0	*J*	0	0	0	0	0
226	0	226	0	–116	0	116	0	116	0	0	0
233	233	233	233	133	133	133	133	133	133	113	112
234	0	0	0	0	0	–134	–134	0	0	0	0
235	235	0	0	0	0	–135	0	0	0	0	0

Continued on the next page

Table A.3 – continued from the previous page

N	$M^{(b)}$	$M^{(c)}$	**O**	T_{II}	T_I	R_{II}	R_I	H_{II}	H_I	C_{II}	C_I
236	0	236	0	–136	0	0	0	0	0	0	0
244	244	244	244	155	155	155	155	155	155	166	155
245	0	245	0	–145	0	–145	0	–145	0	0	0
246	246	0	0	0	0	K	0	0	0	0	0
255	255	255	255	144	144	144	144	144	144	144	144
256	0	0	0	0	0	H	H	0	0	0	0
266	266	266	266	166	166	C	C	C	C	155	155
333	333	333	333	333	333	333	333	333	333	111	111
334	0	0	0	0	0	0	0	0	0	0	0
335	335	0	0	0	0	0	0	0	0	0	0
336	0	336	0	0	0	0	0	0	0	0	0
344	344	344	344	344	344	344	344	344	344	155	155
345	0	345	0	0	0	0	0	0	0	0	0
346	346	0	0	0	0	–135	0	0	0	0	0
355	355	355	355	344	344	344	344	344	344	166	155
356	0	0	0	0	0	134	134	0	0	0	0
366	366	366	366	366	366	D	D	D	D	144	144
444	0	0	0	0	0	444	444	0	0	0	0
445	445	0	0	0	0	445	0	0	0	0	0
446	0	446	0	446	0	145	0	145	0	0	0
455	0	0	0	0	0	–444	–444	0	0	0	0
456	456	456	456	456	456	E	E	E	E	456	456
466	0	0	0	0	0	124	124	0	0	0	0
555	555	0	0	0	0	–445	0	0	0	0	0
556	0	556	0	–446	0	–145	0	–145	0	0	0
556	566	0	0	0	0	125	0	0	0	0	0
666	0	666	0	0	0	–116	0	–116	0	0	0

$A = 111 + 112 - 222$
$B = \frac{1}{4}(-2 \cdot 111 - 112 + 3 \cdot 222)$
$C = \frac{1}{4}(2 \cdot 111 - 112 + 222)$
$D = \frac{1}{2}(113 - 123)$
$E = \frac{1}{2}(-144 + 155)$
$F = \frac{1}{2}(114 + 3 \cdot 124)$
$G = -114 - 2 \cdot 124$
$H = \frac{1}{2}(114 - 124)$
$I = \frac{1}{2}(-115 - 3 \cdot 125)$
$J = -114 - 2 \cdot 125$
$K = \frac{1}{2}(-115 + 125)$

Table A.2: Lattice type (in the Laue group notation of Table A.1), centering type(s), and Cartesian components of conventional lattice vectors ($\boldsymbol{a}$, $\boldsymbol{b}$, and $\boldsymbol{c}$) as defined in `ElaStic` when using the codes `exciting` ($\mathcal{X}$), WIEN2k ($\mathcal{W}$), and Quantum ESPRESSO ($\mathcal{Q}$). α, β, and γ are the angles $\widehat{\boldsymbol{bc}}$, $\widehat{\boldsymbol{ac}}$, and $\widehat{\boldsymbol{ab}}$, respectively. The symbol ξ_ϑ (κ_ϑ) represents the sine (cosine) of the angle ϑ. $\mathrm{M}^{(\boldsymbol{b})}$ and $\mathrm{M}^{(\boldsymbol{c})}$ indicate the monoclinic crystal system with the b and c axis as unique axis, respectively.

Laue group	Centering type(s)	$\boldsymbol{a}$	$\boldsymbol{b}$	$\boldsymbol{c}$	$\mathcal{X}$	$\mathcal{W}$	$\mathcal{Q}$
$\mathrm{C_{I,II}}$	P, F, I	$(a,0,0)$	$(0,a,0)$	$(0,0,a)$	✓	✓	✓
$\mathrm{H_{I,II}}$	P	$(a,0,0)$	$\left(-\frac{1}{2}a, \frac{\sqrt{3}}{2}a, 0\right)$	$(0,0,c)$	✓	✓	✓
$\mathrm{R_{I,II}}$	P				✓	✓	✓
	R	$\left(\tilde{a}, -\frac{1}{\sqrt{3}}\tilde{a}, h\right)$	$\left(0, \frac{2}{\sqrt{3}}\tilde{a}, h\right)$	$\left(-\tilde{a}, -\frac{1}{\sqrt{3}}\tilde{a}, h\right)$	✓	✓	✓
$\mathrm{T_{I,II}}$	P, I	$(a,0,0)$	$(0,a,0)$	$(0,0,c)$	✓	✓	✓
O	P, C, F, I	$(a,0,0)$	$(0,b,0)$	$(0,0,c)$	✓	✓	✓
$\mathrm{M}^{(\boldsymbol{b})}$	P, C	$(a,0,0)$	$(0,b,0)$	$(c\,\kappa_\beta, 0, c\,\xi_\beta)$	×	×	✓
$\mathrm{M}^{(\boldsymbol{c})}$	P, C	$(a,0,0)$	$(b\,\kappa_\gamma, b\,\xi_\gamma, 0)$	$(0,0,c)$	✓	×	✓
		$(a\,\xi_\gamma, a\,\kappa_\gamma, 0)$	$(0,b,0)$	$(0,0,c)$	✓	✓	×
N	P	$(a,0,0)$	$(b\,\kappa_\gamma, b\,\xi_\gamma, 0)$	$(c\,\kappa_\beta, \tilde{c}, w)$	✓	✓	✓

$$\tilde{a} = a\,\xi_{\alpha/2}$$

$$h = a\sqrt{1 - \tfrac{4}{3}\xi_{\alpha/2}^2}$$

$$\tilde{c} = c\,\xi_\gamma^{-1}\left(\kappa_\alpha - \kappa_\beta\,\kappa_\gamma\right)$$

$$w = c\,\xi_\gamma^{-1}\sqrt{1 + 2\kappa_\alpha\kappa_\beta\kappa_\gamma - \kappa_\alpha^2 - \kappa_\beta^2 - \kappa_\gamma^2}$$

B Elastic-Constant Transformations

Due to the fact that the definition of elastic constants depends on the choice of the reference Cartesian coordinate system, **ElaStic** includes a tool which converts the elastic-constants tensor referred to an as "*old*" reference system (with Cartesian coordinates $\{x_i\}$) to a "*new*" one (with transformed coordinates $\{X_i\}$). The transformation between the two coordinate systems is defined by

$$X_i = \sum_{j=1}^{3} a_{ij}\, x_j \,, \tag{B.1}$$

where a_{ij} is the cosine of the angle between the directions of OX_i and Ox_j. Finally, the transformation for the components of the elastic-constant tensor are given by

$$C_{ijkl} = \sum_{o,p,q,r=1}^{3} a_{io}\, a_{jp}\, a_{kq}\, a_{lr}\, c_{opqr} \,, \tag{B.2}$$

and

$$C_{ijklmn} = \sum_{o,p,q,r,s,t=1}^{3} a_{io}\, a_{jp}\, a_{kq}\, a_{lr}\, a_{ms}\, a_{nt}\, c_{opqrst} \,, \tag{B.3}$$

where c_{opqr} (C_{ijkl}) and c_{opqrst} (C_{ijklmn}) are the SOECs and TOECs in the old (new) Cartesian coordinates, respectively.

As we mentioned in Section A.1, for some crystals (*e.g.*, for monoclinic structures) there is more than one choice for Cartesian coordinate frames. Sometimes it is useful to transform the elastic tensor from one Cartesian frame to another. This can be accomplished with the help of Eqs. (B.2) and (B.3), which gives the components of the transformed tensor of the SOEC and TOEC from the initial reference axes to the final coordinate system by applying the proper transformation. In the following, we present some of the matrix transformations that may be needed to transform elastic constants.

- To transform elastic constants for the hexagonal crystal family (hexagonal and trigonal crystal systems) from the STD which is used by **ElaStic**, to the coordinate system applied by the code WIEN2k, one has to use the following transformation matrix:

$$T_{\mathrm{H}}^{\mathrm{STD}\to\mathcal{W}} = \begin{pmatrix} \frac{\sqrt{3}}{2} & \frac{1}{2} & 0 \\ -\frac{1}{2} & \frac{\sqrt{3}}{2} & 0 \\ 0 & 0 & 1 \end{pmatrix} . \tag{B.4}$$

- As can be seen in Table A.2, there are two types of settings for monoclinic crystals in the code Quantum ESPRESSO. The elastic constants can be transformed from the $\mathrm{M}^{(\boldsymbol{b})}$ to the $\mathrm{M}^{(\boldsymbol{c})}$ representation by using the transformation matrix

$$T_{\mathrm{M}}^{\mathcal{Q}_b\to\mathcal{Q}_c} = \begin{pmatrix} 1 & 0 & 0 \\ 0 & 0 & -1 \\ 0 & 1 & 0 \end{pmatrix} . \tag{B.5}$$

- The monoclinic settings of $\mathrm{M}^{(\boldsymbol{c})}$ in Quantum ESPRESSO and WIEN2k are different. The SOECs are comparable if the following matrix is applied to transform the calculated result of Quantum ESPRESSO to WIEN2k,

$$T_{\mathrm{M}}^{\mathcal{Q}_c\to\mathcal{W}_c} = \begin{pmatrix} \sin(\gamma) & \cos(\gamma) & 0 \\ -\cos(\gamma) & \sin(\gamma) & 0 \\ 0 & 0 & 1 \end{pmatrix} . \tag{B.6}$$

C Lattice Optimization

The lattice of a crystal is specified by the lattice parameters, a, b, c, α, β, and γ. The three former parameters are connected to the length of the primitive vectors of the crystal and the three latter are the angles between the primitive vectors. In order to relax the lattice parameters, we performed optimization cycles where the energy was minimized with respect to each degree of freedom in a sequential manner. Each cycle involved minimizing the energy with respect to volume, b/a ratio, c/a ratio, and non-right angle, as follows:

i) *Volume*
All the lattice parameters are changed by the same amount of distortion. The following deformation matrix is applied for volume optimization,

$$\begin{pmatrix} 1+\epsilon & 0 & 0 \\ 0 & 1+\epsilon & 0 \\ 0 & 0 & 1+\epsilon \end{pmatrix}, \tag{C.1}$$

where ϵ is the physical strain. The equilibrium volume and bulk modulus are obtained from least-square fits to the Birch-Murnaghan equation of state [58]

$$E(V) = E_0 + \frac{9V_0B_0}{16}\left\{\left[\left(\frac{V_0}{V}\right)^{\frac{2}{3}} - 1\right]^3 B_0^{'} + \left[\left(\frac{V_0}{V}\right)^{\frac{2}{3}} - 1\right]^2 \left[6 - 4\left(\frac{V_0}{V}\right)^{\frac{2}{3}}\right]\right\}, \tag{C.2}$$

where E_0, V_0, B_0, and $B_0^{'}$ are the minimum energy, equilibrium volume, bulk modulus, and first derivative of bulk modulus with respect to the pressure, respectively.

ii) *b/a ratio*
The b/a ratio was optimized such that the volume of the crystal and the c/a ratio were conserved. The following deformation matrix was applied in order

to get the deformed structures:

$$\begin{pmatrix} \frac{1}{\sqrt{1+\epsilon}} & 0 & 0 \\ 0 & 1+\epsilon & 0 \\ 0 & 0 & \frac{1}{\sqrt{1+\epsilon}} \end{pmatrix}. \tag{C.3}$$

The equilibrium physical strain is obtained from the fit of a fourth-order polynomial function to the energy points of the distorted structures.

iii) *c/a ratio*
The c/a ratio was optimized in the same way as the c/a ratio, but at this stage the b/a ratio and volume are maintained constant. The following matrix is the deformation matrix;

$$\begin{pmatrix} \frac{1}{\sqrt{1+\epsilon}} & 0 & 0 \\ 0 & \frac{1}{\sqrt{1+\epsilon}} & 0 \\ 0 & 0 & 1+\epsilon \end{pmatrix}. \tag{C.4}$$

iv) *Angle α*
α is the angle between the primitive vectors $\boldsymbol{b}$ and $\boldsymbol{c}$. The following deformation matrix changes α conserving the volume of the structure:

$$\begin{pmatrix} \frac{1}{1-\epsilon^2} & 0 & 0 \\ 0 & 1 & \epsilon \\ 0 & \epsilon & 1 \end{pmatrix}. \tag{C.5}$$

In order to determine the equilibrium angle, the same fitting procedure as for the previous two steps.

v) *Angle β*
β is the angle between primitive vectors $\boldsymbol{a}$ and $\boldsymbol{c}$. The following deformation matrix changes β without changing the volume of the structure:

$$\begin{pmatrix} 1 & 0 & \epsilon \\ 0 & \frac{1}{1-\epsilon^2} & 0 \\ \epsilon & 0 & 1 \end{pmatrix}. \tag{C.6}$$

The equilibrium angle β is calculated by the same fitting procedure as explained for the b/a and c/a optimization steps.

vi) *Angle* γ

γ is an angle between primitive vectors $\boldsymbol{a}$ and $\boldsymbol{b}$. The following deformation matrix, which does not change the volume of the structure, is applied for this optimization step:

$$\begin{pmatrix} 1 & \epsilon & 0 \\ \epsilon & 1 & 0 \\ 0 & 0 & \dfrac{1}{1-\epsilon^2} \end{pmatrix}. \tag{C.7}$$

In order to determine the equilibrium angle, the same fitting procedure, as outlined in (ii) and (iii), is applied.

The whole cycle was repeated until the obtained equilibrium parameters were within the desired accuracy.

Acknowledgment

I am most grateful to my supervisor Claudia Draxl who gave me a great chance to consider myself as a scientist and who opened the real scientific word to me eyes.

I am extremely thankful to Pasquale Pavone who was my teacher, friend, and co-worker in this period and helped me in my scientific and nonscientific lives.

It gives me great pleasure in acknowledging the support, help, kindness, and friendliness of Jürgen Spitaler who was always willing to pay attention to my WIEN2k problems.

I would like to thank Katherine Tiede for her kindly accepting, carefully reading, and language correcting of my thesis.

I would like to thank my all friends from Chair of atomistic modelling and design materials and Materials Center Leoben who held nice working and friendly atmosphere in the group.

I am indebted to my colleagues; Lorenz, Maxim, and Lorenzo who were/are good companions for fruitful scientific discussions.

I thank B. Z. Yanchitsky for allowing me the use of the SGROUP code in my program.

This work would have not been possible without the financial support from the Competence Centre for Excellent Technologies (COMET) on Integrated Research in Materials, Processing and Product Engineering (MPPE). Financial support by the Austrian Federal Government and the Styrian Provincial Government is acknowledged.

I cannot find words to express my gratitude to my lovely wife who encouraged and accompanied me and stood by my side in all the hard moments of this period.

And last, but not least, I would like to say thank you to my parents for their steady support during all the years of my studies.

List of Figures

List of Tables

Bibliography

[1] P. Hohenberg, W. Kohn, *Phys. Rev.* **136**, B864 (1964).

[2] W. Kohn, L. J. Sham, *Phys. Rev.* **140**, A1133 (1965).

[3] J. Chen, L. L. Boyer, H. Krakauer, M. J. Mehl, *Phys. Rev. B* **37**, 3295 (1988).

[4] M. J. Mehl, L. L. Boyer, *Phys. Rev. B* **43**, 9498 (1991).

[5] J. M. Wills, O. Eriksson, P. Söderlind, A. M. Boring, *Phys. Rev. Lett.* **68**, 2802 (1992).

[6] L. L. Boyer, E. Kaxiras, J. L. Feldman, J. Q. Broughton, M. J. Mehl, *Phys. Rev. Lett.* **67**, 715 (1991).

[7] R. Nava, J. Romero, *J. Acoust. Soc. Am.* **68**, 529 (1978).

[8] J. H. Cantrell jr., *Phys. Rev. B* **21**, 4191 (1980).

[9] J. H. Cantrell jr., M. A. Breazeale, A. Nakamura, *J. Acoust. Soc. Am.* **67**, 1477 (1980).

[10] M. Nandanpawar, S. Rajagopalan, *J. Acoust. Soc. Am.* **71**, 1469 (1982).

[11] G. Perrin, M. Delannnoy-Coutris, *J. Phys. Chem. Solids.* **49**, 1397 (1988).

[12] R. N. Thurston, *J. Acoust. Soc. Am.* **41**, 1093 (1967).

[13] Y. Hiki, J. F. Thomas, A. V. Granato, *Phys. Rev.* **153**, 764 (1967).

[14] R. R. Rao, *Phys. Rev. B* **10**, 4173 (1974).

[15] J. A. Garber, A. V. Granato, *Phys. Rev. B* **11**, 3990 (1975).

[16] J. A. Garber, A. V. Granato, *Phys. Rev. B* **11**, 3998 (1975).

[17] Z. P. Chang, G. R. Barsch, *Phys. Rev. Lett.* **19**, 1381 (1967).

[18] J. K. Liakosa, G. A. Saundersa, *Phil. Mag. A* **46**, 217 (1982).

[19] M. E. Fine, L. D. Brown, H. L. Marcus, *Scr. Metall.* **18**, 951 (1984).

[20] R. L. Fleischer, *Proc. Int. Symp. on Intermetallic Compounds* p. 157 (1991).

[21] C.-M. Li, Q.-M. Hu, R. Yang, B. Johansson, L. Vitos, *Phys. Rev. B* **82**, 094201 (2010).

[22] G. V. Sinko, *Phys. Rev. B* **77**, 104118 (2008).

[23] S. Shang, Y. Wang, Z.-K. Liu, *Applied Physics Letters* **90**, 101909 (2007).

[24] K. B. Panda, K. S. R. Chandran, *Computational Materials Science* **35**, 134 (2006).

[25] C. Bercegeay, S. Bernard, *Phys. Rev. B* **72**, 214101 (2005).

[26] G. Steinle-Neumann, L. Stixrude, R. E. Cohen, *Phys. Rev. B* **60**, 791 (1999).

[27] P. Ravindran, L. Fast, P. A. Korzhavyi, B. Johansson, *J. of Appl. Phys.* **84**, 4891 (1998).

[28] H. Yao, L. Ouyang, W.-Y. Ching, *Journal of the American Ceramic Society* **90**, 3193 (2007).

[29] M. Iuga, G. Steinle-Neumann, J. Meinhardt, *Eur. Phys. J. B* **58**, 127 (2007).

[30] W. F. Perger, J. Criswell, B. Civalleri, R. Dovesi, *Computer Physics Communications* **180**, 1753 (2009).

[31] R. Yu, J. Zhu, H. Q. Ye, *Computer Physics Communications* **181**, 671 (2010).

[32] J. Nye, *Physical properties of crystals: their representation by tensors and matrices*, Oxford science publications (Clarendon Press, 1985).

[33] D. Wallace, *Thermodynamics of Crystals*, Dover books on physics (Dover Publications, 1998).

[34] L. Vitos, *Computational Quantum Mechanics for Materials Engineers: The Emto Method and Applications*, Engineering Materials and Processes Series (Springer-Verlag London Limited, 2007).

[35] J. Lubliner, *Plasticity Theory* (Dover Publications, 2008).

[36] O. H. Nielsen, R. M. Martin, *Phys. Rev. Lett.* **50**, 697 (1983).

[37] W. Voigt, *Lehrbuch der Kristallphysik* (1928).

[38] A. Reuss, *Z. Angew. Math. Mech.* **9**, 49 (1929).

[39] R. Hill, *Proc. Phys. Soc. A* **65**, 349 (1952).

[40] R. Hill, *J. Mech. Phys. Solids* **11**, 357 (1963).

[41] M. Born, R. Oppenheimer, *Annalen der Physik* **389**, 457 (1927).

[42] C. Fiolhais, F. Nogueira, M. Marques, *A Primer in Density Functional Theory*, Lecture Notes in Physics (Springer, 2003).

[43] E. Engel, R. Dreizler, *Density Functional Theory: An Advanced Course*, Texts and Monographs in Physics (Springer, 2011).

[44] J. P. Perdew, A. Zunger, *Phys. Rev. B* **23**, 5048 (1981).

[45] L. A. Cole, J. P. Perdew, *Phys. Rev. A* **25**, 1265 (1982).

[46] J. P. Perdew, Y. Wang, *Phys. Rev. B* **45**, 13244 (1992).

[47] J. P. Perdew, K. Burke, Y. Wang, *Phys. Rev. B* **54** (1996).

[48] J. P. Perdew, A. Ruzsinszky, G. I. Csonka, O. A. Vydrov, G. E. Scuseria, L. A. Constantin, X. Zhou, K. Burke, *Phys. Rev. Lett.* **100**, 136406 (2008).

[49] J. C. Slater, *Phys. Rev.* **51**, 846 (1937).

[50] D. Singh, L. Nordström, *Planewaves, Pseudopotentials, And the LAPW Method* (Springer, 2006).

[51] O. K. Andersen, *Phys. Rev. B* **12**, 3060 (1975).

[52] D. Singh, *Phys. Rev. B* **43**, 6388 (1991).

[53] E. Sjöstedt, L. Nordström, D. Singh, *Solid State Communication* **114**, 15 (2000).

[54] B. Z. Yanchitsky, A. N. Timoshevskii, *Computer Physics Communications* **139**, 235 (2001).

[55] S. Geisser, *Predictive inference: an introduction* (New York: Chapman and Hall, 1993).

[56] P. A. Devijver, J. Kittler, *Pattern recognition: a statistical approach* (Prentice/Hall International, 1982).

[57] A. van de Walle, G. Ceder, *Journal of Phase Equilibria* **23**, 348 (2002).

[58] F. Birch, *Phys. Rev.* **71**, 809 (1947).

[59] M. J. Mehl, *Phys. Rev. B* **61**, 1654 (2000).

[60] P. E. Blöchl, O. Jepsen, O. K. Andersen, *Phys. Rev. B* **49**, 16223 (1994).

[61] H. J. Monkhorst, J. D. Pack, *Phys. Rev. B* **13**, 5188 (1976).

[62] M. Methfessel, A. T. Paxton, *Phys. Rev. B* **40**, 3616 (1989).

[63] T. Hom, W. Kiszenik, B. Post, *Journal of Applied Crystallography* **8**, 457 (1975).

[64] G. Chiarotti, *1.6 Crystal structures and bulk lattice parameters of materials quoted in the volume*, vol. 24c of *Landolt-Börnstein-Group III Condensed Matter Numerical Data and Functional Relationships in Science and Technology* (Springer-Verlag, 1995).

[65] V. Ganesan, K. Girirajan, *Pramana - Journal of Physics* **27**, 472 (1986).

[66] G. L. Clendenen, H. G. Drickamer, *Phys. Rev.* **135**, A1643 (1964).

[67] J. Donohue, *The structures of the elements*, A Wiley-Interscience Publication (Wiley, 1974).

[68] L. N. Kugai, *Inorg. Chem.* **8**, 669 (1972).

[69] W. E. Lee, K. P. D. Lagerlof, *Journal of Electron Microscopy Technique* **2**, 247 (1985).

[70] R. J. Reeder, S. A. Markgraf, *American Mineralogist* **71**, 795 (1986).

[71] G. Vidal-Valat, J. P. Vidal, C. M. E. Zeyen, K. K. Suonio, *Acta Crystallographica Section* **B**, 1584 (1979).

[72] R. M. Hazen, L. W. Finger, J. W. E. Mariathasan, *J. Phys. Chem. Solids* **46**, 253 (1985).

[73] R. Rosenkranz, G. Frommeyer, *Z. Metallkd.* **83**, 685 (1992).

[74] C. J. Howard, R. J. Hill, B. E. Reichert, *Acta Crystallogr., Sect. B: Struct. Sci.* **44**, 116 (1988).

[75] A. G. Every, A. K. McCurdy, *Table 3. Cubic system. Elements*, vol. 29a of *Landolt-Börnstein-Group III Condensed Matter Numerical Data and Functional Relationships in Science and Technology* (Springer-Verlag, 1992).

[76] D. D. Slagle, H. A. McKinstry, *J. Appl. Phys.* **38**, 446 (1967).

[77] P. E. Blöchl, *Phys. Rev. B* **50**, 17953 (1994).

[78] D. Vanderbilt, *Phys. Rev. B* **41**, 7892 (1990).

[79] P. S. Spoor, J. D. Maynard, M. J. Pan, D. J. Green, J. R. Hellman, T. Tanaka, *Appl. Phys. Lett.* **70**, 1959 (1997).

[80] C. J. Smithells, E. A. Brandes, F. R. Institute., *Smithells metals reference book*, vol. 8 (Butterworth-Heinemann, 1983).

[81] Y. Le Page, P. Saxe, *Phys. Rev. B* **65**, 104104 (2002).

[82] H. Kimizuka, H. Kaburaki, Y. Kogure, *Phys. Rev. B* **67**, 024105 (2003).

[83] J. Purton, R. Jones, C. R. A. Catlow, M. Lesie, *Phys. Chem. Miner.* **19**, 392 (1993).

[84] B. Holm, R. Ahuja, *J. Chem. Phys.* **111**, 2071 (1999).

[85] R. Bechmann, *Phys. Rev.* **110**, 1060 (1958).

[86] W. P. Mason, *Van Nostrand* **84**, 508 (1950).

[87] E. Gregoryanz, R. J. Hemley, H.-K. Mao, P. Gillet, *Phys. Rev. Lett.* **84**, 3117 (2000).

[88] P.-F. Chen, L.-Y. Chiao, P.-H. Huang, *Physics of the Earth and Planetary Interiors* **155**, 73 (2006).

[89] P. Humbert, F. Plique, *CR Acad. Sci.* **275**, 391 (1972).

[90] E. R. Naimon, *Phys. Rev. B* **4**, 4291 (1971).

[91] R. E. Hankey, D. E. Schuele, *J. Acoust. Soc. Am.* **48**, 190 (1970).

[92] H. R. Cutler, J. J. Gibson, K. A. McCarthy, *Solid State Communications* **6**, 431 (1968).

[93] W. J. Alton, A. J. Barlow, *J. Appl. Phys.* **38**, 3817 (1967).

[94] M. Nakamura, *Metall. Trans.* **A**, 331 (1993).

[95] S. C. Chan, Y. Fang, M. Grimsditch, Z. Li, M. Nevitt, W. Robertson, E. S. Zoubolis, *J. Am. Ceram. Soc.* **74**, 1742 (1991).

[96] G. Kurdjumov, L. Khandros, *Dokl Nauk SSSR* **66**, 211 (1949).

[97] L. C. Chang, T. A. Read, *Trans. AIME.* **189**, 47 (1951).

[98] Z. B. Basinski, J. W. Christian, *Acta Metall.* **2**, 101 (1954).

[99] K. Otsuka, K. Otsuka, C. Wayman, *Shape memory materials* (Cambridge University Press, 1999).

[100] J. M. Zhang, G. Y. Guo, *Phys. Rev. Lett.* **78**, 4789 (1997).

[101] K. Parlinski, M. Parlinska-Wojtan, *Phys. Rev. B* **66**, 064307 (2002).

[102] D. Mutter, P. Nielaba, *Phys. Rev. B* **82**, 224201 (2010).

[103] P. Souvatzis, D. Legut, O. Eriksson, M. I. Katsnelson, *Phys. Rev. B* **81**, 092201 (2010).

[104] M.-X. Wagner, W. Windl, *Acta Materialia* **56**, 6232 (2008).

[105] N. Hatcher, O. Y. Kontsevoi, A. J. Freeman, *Phys. Rev. B* **80**, 144203 (2009).

[106] D. Lagoudas, *Shape memory alloys: modeling and engineering applications* (Springer, 2008).

[107] X. R. K. Otsuka, *Materials Science* **50**, 511 (2005).

[108] X. Huang, G. J. Ackland, K. M. Rabe, *Nature Materials* **2**, 307 (2003).

[109] G. M. Michal, R. Sinclair, *Acta Crystallographica Section B* **37**, 1803 (1981).

[110] F. E. Wang, S. J. Pickart, H. A. Alperin, *J. Appl. Phys.* **43** (1972).

[111] P. Sittner, P. Lukas, D. Neov, V. Novak, D. M. Toebbens, *J. Phys. IV France* **112**, 709 (2003).

[112] C. M. H. Wang, M. Meichle, M. B. Salamon, C. M. Wayman, *Philos Mag. A* **47**, 31 (1983).

[113] E. Goo, R. Sinclair, *Acta Metall.* **33**, 1717 (1985).

[114] T. Hara, T. Ohba, E. Okunishi, K. Otsuka, *Materials Transactions JIM* **38**, 11 (1997).

[115] D. Schryvers, P. L. Potapov, *Materials Transactions* **43**, 774 (2002).

[116] C. Gong, Y. Li, Y. Yang, D. Yang, *Modelling Simul. Mater. Sci. Eng.* **14**, 33 (2006).

[117] S. D. Prokoshkin, A. V. Korotitskiy, V. Brailovski, S. Turenne, I. Y. Khmelevskaua, I. V. Trubitsyna, *Acta Mater.* **52**, 4479 (2004).

[118] Y. Kudoh, M. Tokonami, S. Miyazaki, K. Otsuka, *Acta Metall.* **33**, 2049 (1985).

[119] M. Sanati, R. C. Albers, F. J. Pinski, *Phys. Rev. B* **58**, 13590 (1998).

[120] T. H. Nam, T. Saburi, Y. Nakata, K. Shimizu, *Materials Transactions, JIM* **31**, 959 (1990).

[121] Y. Y. Ye, C. T. Chan, K. M. Ho, *Phys. Rev. B* **56**, 3678 (1997).

[122] J. C. Gachon, M. Notin, J. Hertz, *Thermochimica Acta* **48**, 155 (1981).

[123] O. Kubaschewski, *Transactions of the Faraday Society* **54**, 814 (1958).

[124] A. Pasturel, C. Colinet, D. N. Manh, A. T. Paxton, M. van Schilfgaarde, *Phys. Rev. B* **52**, 15176 (1995).

[125] T. M. Brill, S. Mittelbach, W. Assmus, M. Müllner, B. Lüthi, *J. Phys. Condens. Matter* **3**, 9621 (1991).

[126] O. Mercier, K. N. Melton, G. Gremaud, J. Häji, *J. Appl. Phys.* **51**, 1833 (1980).

[127] M. Born, K. Huang, *Dynamical Theory of Crystal Lattices*, Oxford Classic Texts in the Physical Sciences (Oxford University Press, USA, 1998).

[128] S. F. Pugh, *Philos. Mag.* **45**, 823 (1954).

[129] M. Achenbach, *International Journal of Plasticity* **5**, 371 (1989).